August 2022

Swimming Ability of the Enigmatic Carboniferous Fish: Tullimonstrum Gregarium

Jacob James Potter
University of Wisconsin-Milwaukee

SWIMMING ABILITY OF THE ENIGMATIC CARBONIFEROUS FISH: *TULLIMONSTRUM GREGARIUM*

by

Jacob James Potter

A Thesis Submitted in

Partial Fulfillment of the

Requirements for the Degree of

Master of Science

in Geoscience

at

The University of Wisconsin-Milwaukee

August 2022

ABSTRACT

THE SWIMMING ABILITY OF THE ENGIMATIC CARBONIFEROUS FISH:
TULLIMONSTRUM GREGARIUM
by
Jacob James Potter

The University of Wisconsin-Milwaukee, 2022
Under the Supervision of Professor Dr. Victoria McCoy

Tullimonstrum gregarium, more commonly known as the Tully Monster, is one of the strangest creatures in the fossil record. While it was traditionally considered a problematic fossil, recent studies have firmly placed the Tully Monster with the vertebrates as a relative of lamprey and hagfish. This may offer insight into the Tully Monster's ecology, but the Tully Monster's Swimming ability remains uncertain due to its strange body plan. This study aims to investigate the hydrodynamics of these features to gain insight into the Tully Monster's swimming ability using computational fluid dynamics (CFD). 3D and 2D simulations of the Tully Monster revealed that the eyebar and proboscis are likely key hydrodynamic features, and that the tail fin complex could have generated pressure differentials. Pressures generated around the body also suggest the Tully Monster was a slow swimmer, and likely had a hydrodynamic tendency to descend in the water column.

TABLE OF CONTENTS

PAGE

LIST OF FIGURES

LIST OF TABLES

ACKNOWLEDGEMENTS

I would like to thank my advisor, Dr. Victoria McCoy for all of her support throughout my graduate degree at UWM, in the face of many challenges like starting graduate school in a pandemic, transitioning from biology to geoscience, and learning how to use software neither of us were familiar with beforehand. I would like to especially thank her for allowing me to pursue a project in functional morphology instead of paleobotany, even though she does not have a strong background in functional morphology. I cannot thank her enough for allowing me to pursue my passions, even though it was not the original plan. Dr. McCoy was a fantastic advisor, and I am very happy to continue working with her on this project throughout my PhD. I would also like to thank my committee, Dr. Victoria McCoy, Dr. Mark Harris, and Dr. John Janssen, for their time, support, and input throughout my master's program. The expertise of Dr. Houshou Jiang, Dr. Tom Hansen, and Dr. Rudolph Strickler was also instrumental in helping me run CFD simulations and in interpreting the results of this project. I would also like to thank Dr. Amanda Falk, Dr. Robert Schalkoff, and many other professors and mentors from my undergraduate at Centre College. I would not be here without their guidance, expertise, and support throughout my B.S. in biology and French at Centre College.

Finally, I would like to thank friends and family for helping me get to this point. I knew since high school that I wanted to pursue a PhD, but my path was not linear. I went from wanting to be an astrobiologist to a microbiologist to a paleontologist while persevering through the twists and turns of high school, college, and now a master's degree. They watched as I developed a love for teaching, even though I spent most of my childhood afraid of talking to any strangers and they kept me sane as I moved to a city I had never visited in the middle of a pandemic while starting graduate school online. I cannot thank them enough for their support.

Chapter 1: Introduction

Fossil organisms capture our imagination in ways other organisms do not. Strange long-necked reptiles, colossal predators, and flying creatures crowd our movie screens, making us wonder how these fascinating creatures looked in their time. Smaller problematic fossil organisms are even more bizarre, and they can make us wonder how strange the past diversity of life could have been. These problematic taxa, like *Opabinia regalis*, *Sharovipteryx mirabilis*, and *Hallucigenia* sometimes resemble creatures more suited for a sci-fi movie set on an alien world, reminding us just how alien our planet can be in the deep past. Taxa like these have characteristically remained mysterious over time, defying an easy placement onto the tree of life or into a niche of their fossil ecosystems. New techniques, however, have paved the way for paleontologists to finally classify some of these organisms and answer some longstanding questions about their anatomy (Cunningham et al., 2014; Racicot, 2016; Dec, 2019; Troelsen et al., 2019; Ferrón et al., 2020; Ferrón et al., 2021).

Despite this recent progress, some taxa deemed 'problematica,' remain a mystery (Troelsen et al., 2019). *Tullimonstrum gregarium*, better known as the Tully Monster, is one the most famous, now solved, mysterious problematic creatures. Recent studies have finally resolved the Tully Monster's phylogenetic affinities (Clements et al., 2016; McCoy et al., 2016), which has helped inform hypotheses surrounding the Tully Monster's life habits. Namely, how did the Tully Monster swim, given its odd anatomy? This study aims to investigate the Tully Monster's hydrodynamic properties using computational fluid dynamics, one of the many new computational techniques being incorporated into paleontological studies (Cunningham et al., 2014), by building digital models of the Tully Monster and placing them in a simulated

environment with flowing water. This will serve as a first step to understanding the swimming abilities of this strange fish.

Introduction to the Tully Monster

Recent studies have placed the Tully Monster firmly within the vertebrates after considerable past debate (Clements et al., 2016; Kuratani and Hirasawa, 2016; McCoy et al., 2016; Sallan et al., 2017; McCoy et al., 2020). Based on this interpretation, the Tully Monster is likely a relative of lamprey and hagfish, but this raises more questions than answers (McCoy et al., 2016; Kuratani and Hirasawa). While we do see lamprey and hagfish in the fossil record, they, like many soft-bodied organisms, are exceedingly rare (Gess et al., 2006). In fact, the Mazon Creek Lagerstätte in Illinois, USA, where the Tully Monster is found, is one of the few localities that preserves lamprey and hagfish fossils (Bardack and Zangerl, 1968; Gess et al., 2006). If the Tully Monster is truly related to lamprey and hagfish, their fossil diversity is far higher than previously thought (McCoy et al., 2016).

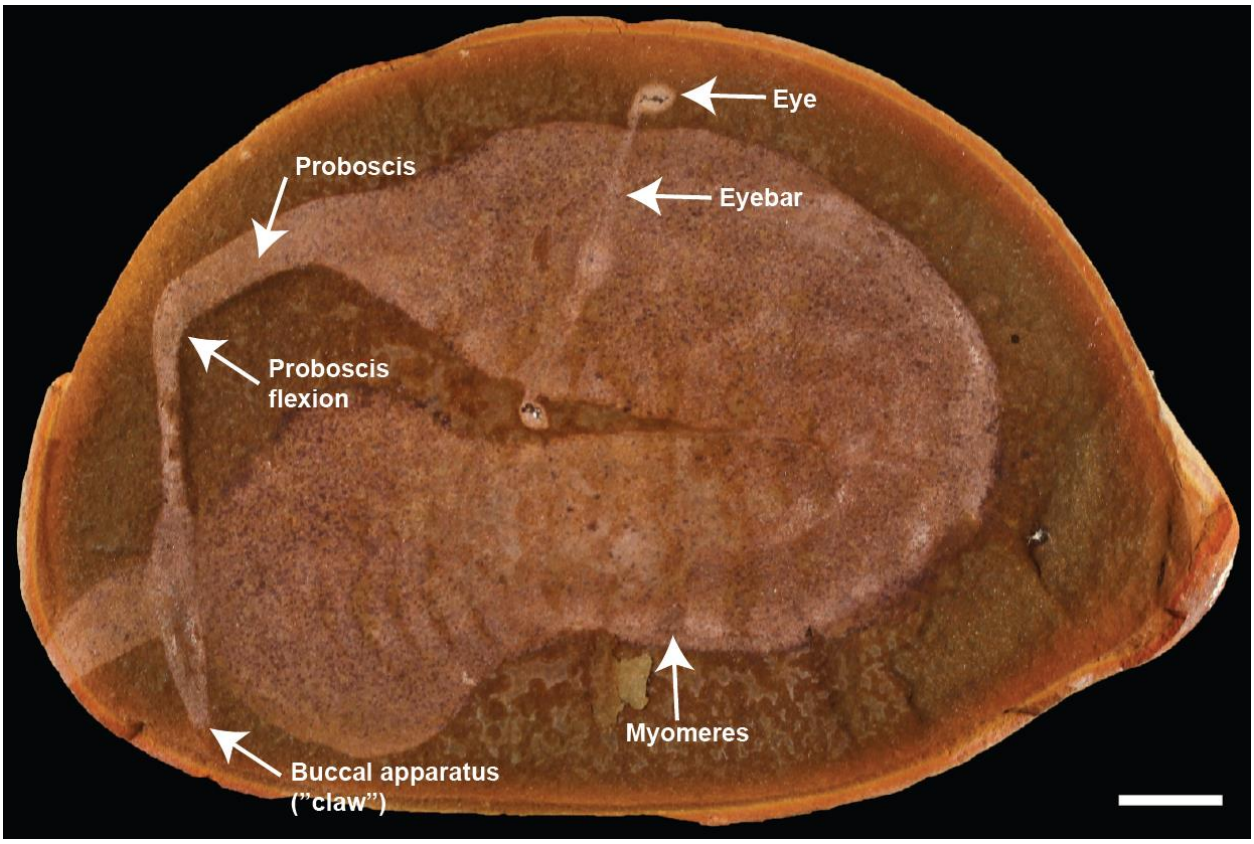

Figure 1.1: An annotated image of Tullimonstrum gregarium specimen FMNH PE 81597. The scale bar in the image equals 1 cm, and annotations highlight key morphological features in this complete specimen. Photo taken by Paul Mayer.

Exploring the Tully Monster's strange anatomy can give insight into this potential diversity (Wainwright, 1994; Thomason, 1997). The Tully Monster is truly unique; it resembles no other known fish with its strange, rigid horizontal eyebar, its elongate probiscis, and its relatively few fins (McCoy et al., 2016). On their own, none of these features are unique to the Tully Monster. Dragonfish larva, for example, have eyes on rigid horizontal stalks (Evans et al., 2005), several elephantnose fish species have elongated rostrums similar to a proboscis (Marrero and Winemiller, 1993; Feulner et al., 2008; Lamanna et al., 2016; Amen et al., 2020), and lamprey have similarly reduced fins (Shimeld and Donoghue, 2012). While none of these features are unique to the Tully Monster, the combination of these strange anatomical features

raises questions about the Tully Monster's mobility and life habits (McCoy et al., 2016, Sallan et al., 2017). The Tully Monster has been interpreted as a predator based on its teeth-like protrusions at the end of its elongate probiscis (Mikulic and Kluessendorf, 1991), but this implies the Tully Monster must have hunted or caught prey. Based on its elongate probiscis, short anterior-heavy body, and relatively simple fin arrangement including only a tail fin and very small dorsal fin, the Tully Monster probably would not have been a fast or nimble predator (Nursall, 1958; Webb, 1977; Webb, 1984; Lauder, 1989; Han et al., 2020). In fact, this combination of features calls into question whether the Tully Monster was a stable swimmer at all. No other known fish exhibits a completely analogous, and paleontologists are confident in their anatomical recreations since *Tullimonstrum gregarium* specimens are typically found as complete body fossils in concretions (Johnson and Richardson, 1969; Clements et al., 2016; McCoy et al., 2016). Since we have no perfect modern or fossil analogue for the Tully Monster, we are left to speculate on its ecological role and therefore the overall diversity of lamprey and hagfish ancestors.

Fish Swimming in General

Modern fish exhibit a wide array of swimming behaviors to solve different problems they commonly face in their respective environments (Nursall, 1958; Webb, 1977, Aleyev, 1977; Webb, 1984; Lauder, 1989; Drucker and Lauder, 2004). While these behaviors are diverse, certain morphological relationships, like the relationship between a fin's placement on the body and its function, are highly conserved despite phylogenetic distance (Webb, 1984; Lauder, 1989; Drucker and Lauder, 2004). Fins placed anteriorly tend to be used for steering and pitch control, for example, while fins place posteriorly are almost always used to propel a fish forward (Webb,

1977; Webb, 1984; Lauder, 1989). Medial fins also tend to provide roll stability as keels and rudders (Webb, 1977; Webb, 1984).

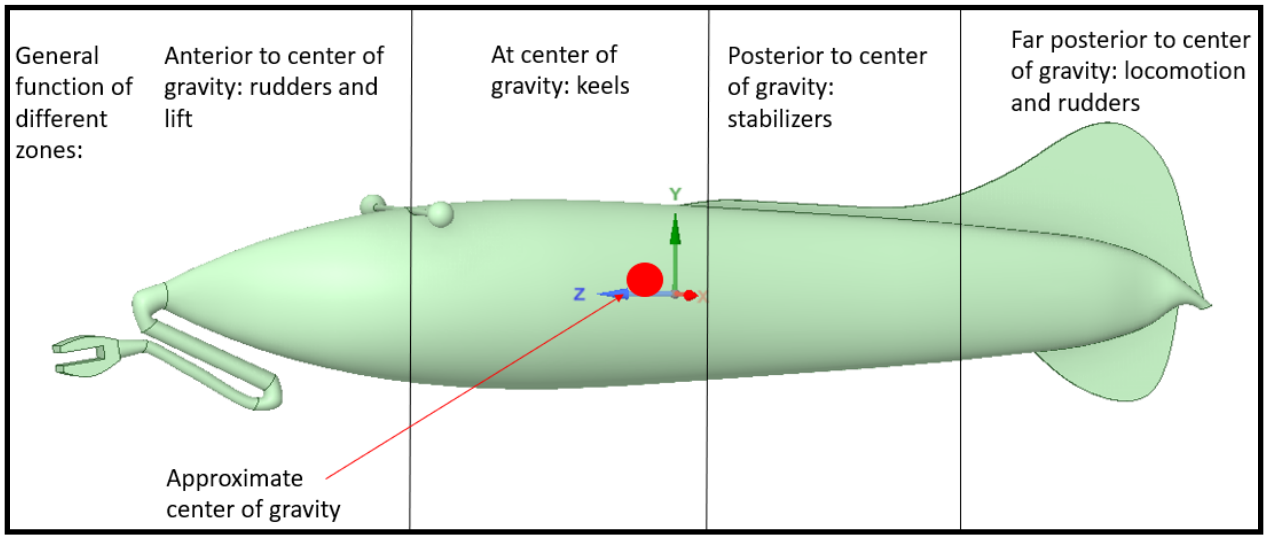

Figure 1.2: A diagram dividing the fully folded model into four functional zones based on distance from the approximate center of gravity and fin function observed in other fish.

As mentioned before, the Tully Monster lacks several common fins, like paired fins and medial fins (McCoy et al., 2016). However, the conserved placement of control and stability surfaces among other fish (Webb, 1977; Webb, 1984) suggests the Tully Monster's eyebar could have served a roll and pitch stability function like fins would, based on the eyebar's medial-anterior placement. Structures like the armored headshields of various agnathan groups and the horizontal surfaces of the hammerhead shark head could be functionally analogous to the Tully Monster eyebar, and these structures are hypothesized to produce lift to counteract negative buoyancy elsewhere in the body, stabilize the anterior of the body, and/or increase anterior mobility (Kajiura et al., 2003; Botella and Fariña, 2008; Dec, 2019). If the eyebar is analogous to these structures, the horizontal eyebar could have acted like a hydrofoil, producing hydrodynamic lift to keep the Tully Monster's body level and stable during swimming or in a flow.

While the fin placement for propulsion and stability tends to be conserved across groups of modern fish (Webb, 1977; Webb, 1984; Lauder, 1989; Drucker and Lauder, 2001; Lauder and Drucker, 2004), braking behaviors tend to vary among modern fish (Lauder and Drucker, 2004). Some fish, like many teleosts, will use their pectoral fins to push against the direction of their movement while dropping their pelvic fins down to disrupt the flow and slow their movement (Lauder and Drucker, 2004). Other fish fins employ other strategies like flaring their pectoral fins or unfurling a large fan-like tail fin to disrupt the flow and slow themselves (Lauder and Drucker, 2004; Flammang and Lauder, 2008). Since these behaviors are more variable and are less tied to a specific fin position (Lauder and Drucker, 2004; Flammang and Lauder, 2008), it is difficult to use other fish braking behaviors as analogues to hypothesize how the Tully Monster would have braked.

Swimming Hypotheses

While the Tully Monster lacks a perfect analogue, there are several fish that could provide insight into the Tully Monster's swimming and life habits. The Tully Monster was likely a slow sub-carrangiform or carrangiform swimmer, based on its overall body shape, tail aspect ratio, and caudally clustered myomeres that would favor tail-dominated swimming over anguilliform swimming (McDowall, 2003; McDowall, 2008; Tytell et al., 2010; McCoy et al., 2016). Carrangiform and sub-carrangiform swimming is not slow by nature, and many fast swimming fish are carrangiform or sub-carrangiform swimmers (Webb, 1977; Webb, 1984; Lauder, 1989; Lauder and Drucker, 2004). Instead, the strange anatomy of the Tully Monster (McCoy et al., 2016) suggests that it was a slow swimmer. Slow swimming does not exclude a predatorial lifestyle, however. Several modern fish have hunting strategies that do not require particularly fast swimming (Olla et al., 1972; Summers, 1980; Westneat and Wainwright, 1989;

Burgess et al., 2011; Gemmell et al., 2013). The slingjaw wrasse (*Epibulus insidiator*), for example, hunts prey by slinging its jaw significantly forward to catch prey (Westneat and Wainwright, 1989; Burgess et al., 2011). In this case, the prey fish does not evade the wrasse preemptively since the wrasse appears to be out of range (Burgess et al., 2011). The head of the seahorse's head functions similarly by reducing the hydrodynamic indicators prey can detect before the seahorse approaches close enough to quickly move its jaw into position to capture the prey with suction (Gemmell et al., 2013). It is possible the Tully Monster's elongate proboscis could have allowed the Tully Monster to hunt in a similar way. A small proboscis likely would have been innocuous to prey fish, allowing the Tully Monster to slowly shadow unsuspecting prey before stealthily capturing them in a hidden jaw apparatus that is either gradually moved into position or is rapidly accelerated towards the target, similar to the slingjaw wrasse's jaw (Burgess et al., 2011).

Alternatively, the Tully Monster could have used its proboscis like the elephant nose fish to scour for burrowing invertebrates and insects in and on soft sediment (Marrero and Winemiller, 1993; Feulner et al., 2008; Lamanna et al., 2016; Amen et al., 2020). This could be a particularly compelling analogy since the elephant nose fish lives in the Congo River, and specimens with highly elongated rostrums have been found in small environments near the mouth of the Congo River (Sullivan et al., 2002; Feulner et al, 2007; Feulner et al., 2008; Decru et al., 2017). Tentatively, the mouth of the Congo River may be a similar environment to the environment that formed the Mazon Creek Lagerstätte, with a high sediment load dominated by clays that are quickly deposited close to the mouth of the river instead of forming a typical delta (Bailey and Banister, 1986; Savoye et al., 2000; Savoye et al., 2009; Dennielou et al., 2017). This suggests the elephant nose fish could have occupied a similar niche to the Tully Monster

with a similar morphology. In this hypothetical case, the Tully Monster's proboscis would likely be extended below its body as the Tully Monster holds its position above the sediment. The Tully Monster's eyebar could be particularly useful in this situation since they extend beyond the maximum width of the body and could provide a wide view below the Tully Monster's body – other fish with eyes widely separated on a horizontal structure, such as hammerhead sharks and dragonfish larvae, have very wide fields of view (Weihs and Moser, 1981; McComb et al., 2009) -- allowing the Tully Monster to finely control its proboscis as it browses in the sediment.

It is also possible that the Tully Monster simply held its proboscis in front of its body as it either slowly chased prey or attempted to ambush prey. Several modern fish with elongated rostrums are able to successfully hunt prey (Scott and Tibbo, 1968; Chenhan, Yongjun, 1988; Kotrschal, 1989; Turigan, 1994; Vose and Nelson, 1994; Shimose et al., 2006; Wueringer et al., 2009; Ballard and Rakocinski, 2012). The filefish and triggerfish (Family *Monoacanthidae* and *Balistidae* respectively), for example, are reef fish that typically browse around reef structures for invertebrates or algae (Kotrschal, 1989; Turnigan, 1994; Vose and Nelson, 1994; Ballard and Rakocinski, 2012). However, both the filefish and the triggerfish are also capable of capturing and eating small fish with its elongated jaw via suction feeding (Kotrschal, 1989; Ballard and Rakocinski, 2012). Filefish and triggerfish are also relatively slow for their body size, with swimming behaviors adapted for small, fine-tuned movement within a complex reef environment (Videler, 1993; Arreola and Westneat, 1996). While the Tully Monster did not live in a reef environment, it is possible the Tully Monster swam slowly around its environment with its proboscis held in either a relaxed position in front of its body (Fig. 1.3) or in a fully extended position held straight in front of its body. Four 3D models of the Tully Monster were generated to investigate the impact of proboscis position and the eyebar on swimming ability for this study

(Fig. 1.3). These proboscis positions are based on the in-depth morphology study by McCoy et al. in 2016, which identified several joints and constraints on the Tully Monster's proboscis (McCoy et al., 2016). Specifically, the proboscis has three joints: one near the proboscis' attachment to the body, one roughly halfway along the length of the proboscis, and one near the attachment of the proboscis to the buccal apparatus (McCoy et al., 2016). Given the wide range of preserved proboscis positions among Tully Monster specimens (McCoy et al., 2016), the joint attaching the body to the proboscis and the joint roughly halfway along the proboscis are assumed to be mobile for this study in the zy-plane with a wide range of motion. The distal joint connecting the proboscis to the buccal apparatus, however, was assumed to be mostly immobile for this study. In most specimens, this distal joint is held at a consistent 130° angle between the buccal apparatus and the distal portion of the proboscis (McCoy et al., 2016), and this angle is reflected in this studies models (Fig 1.3).

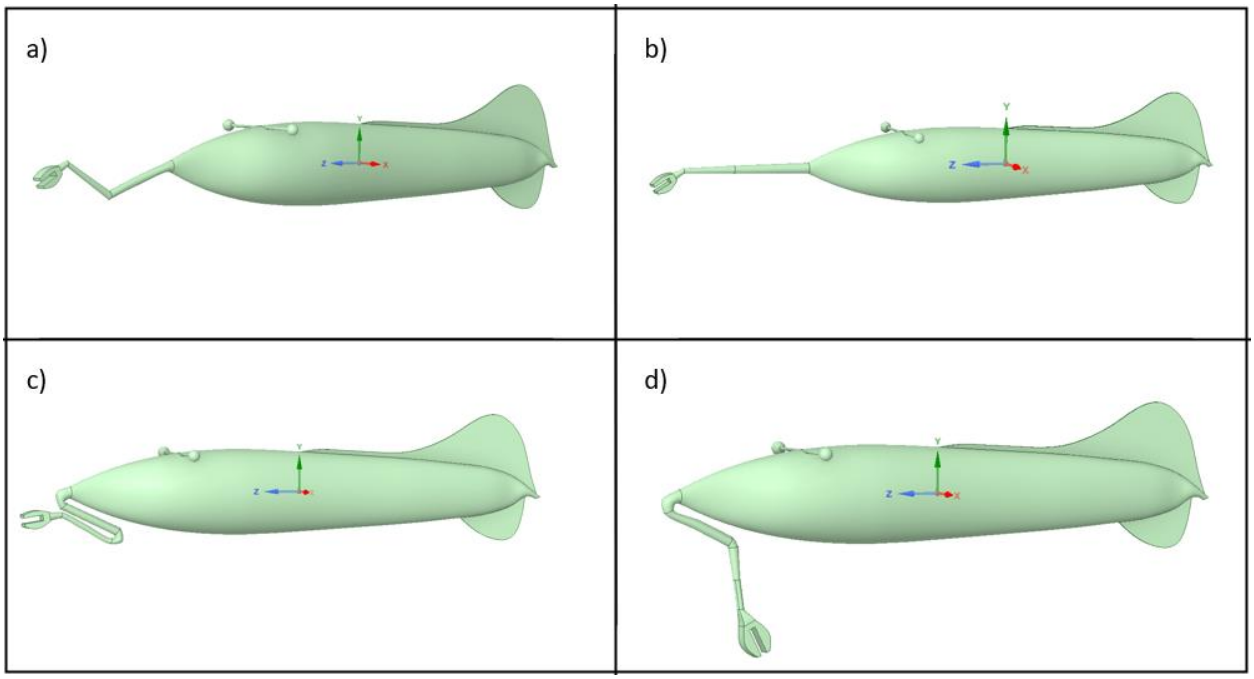

Figure 1.3: The 3D versions of each of the Tully Monster models used in this study. a) The typical reconstruction model, reflecting a relaxed proboscis position b) The fully extended model with each proboscis joint fully locked forward c) The fully folded model with the proboscis folded at each joint to pull the structure under the body d) The folded and lowered model, where the proboscis is folded under the body and lowered below the body.

Computational Fluid Dynamics in paleontology/biology

While computational fluid dynamics (CFD) is primarily used in engineering to design machine parts involved in air or water flows, CFD has seen some use in biology and paleontology (Dec, 2019; Ferrón et al., 2020; Gaylord et al., 2020; Ferrón et al., 2021; Jiang et al., 2021; Li et al., 2021). Before CFD software was widely available, however, biologists created static or robotic fish models suspended in flows to analyze fish hydrodynamics (Hultmark et al., 2007; Lauder et al., 2007; Botella and Fariña, 2008). Particles were added to the flow, and a combination of cameras, lasers, and computer software could track the movement of these particles as they deflected around the fish model or the robotic fish (Hultmark et al., 2007;

Lauder et al., 2007). By analyzing how these particles were deflected, researchers could infer pressure gradients generated by a fish's body and therefore gain a broad view of the hydrodynamics acting on the fish's body as it swims (Hultmark et al., 2007; Lauder et al., 2007; Botella and Fariña, 2008).

CFD software has streamlined this process (Gaylord et al., 2020). Highly realistic models can now be generated in modeling software associated with CFD software relatively easily and quickly compared to physical models. These models can also be manipulated to focus on the effect of individual parts of the fish's body, allowing for more focused analyses (Dec, 2019; Ferrón et al., 2020; Gaylord et al., 2020; Ferrón et al., 2021; Jiang et al., 2021). CFD software itself also provides much more accurate and replicable data compared to physical modeling (Gaylord et al., 2020; Li et al., 2021). In a CFD analysis, each particle added to the simulation is tracked automatically, reducing the chance that any particles would be ignored accidentally (Li et al., 2021). Additionally, these simulations are iterated to reduce error, and the customization inherent in CFD simulations allows researchers to fine-tune their studies to their accepted level of error (Ansys, 2021). Furthermore, most CFD software automatically runs statistical analyses on the simulation's results and generates useful figures to visualize pressure differences and particle speeds around models (Li et al., 2021).

This study used the ANSYS Student suite of programs, which includes the ANSYS Fluent CFD program and various CFD workflows (Ansys, 2021). The ANSYS Student suite is available to students free of charge with few restrictions, although there is a limit on the overall size and resolution of models placed into CFD simulations (Ansys, 2021). Therefore, this study's simulations are inherently size-limited and resolution limited (Ansys, 2021). This is not an issue for general hydrodynamic studies in 2D, which are highly informative and form the bulk of this

analysis (Jiang et al. 2021). However, this does restrict the resolution of 3D results and makes full swimming simulations with moving models impossible to run on the student version of ANSYS Fluent (Ansys, 2021). As a result, the 3D models generated for this study were used to provide a broad overview of the hydrodynamic effects of the Tully Monster while the 2D models generated from the 3D models provided a much more fine-scale and quantitative view of the Tully Monster's hydrodynamics.

Chapter 2: Geologic Background

The Mazon Creek Lagerstätte

The Mazon Creek Lagerstätte is one of the best known Carboniferous fossil assemblages worldwide, offering the highest diversity of Carboniferous flora at a single site and a staggering array of fossil fauna originating from interconnected habitats (Baird et al., 1985; Baird et al., 1986; Foster, 1998; Kuecher et al., 1999; Cotroneo et al., 2016; Clements et al., 2019). The localties that produce the fossils of the Mazon Creek Lagerstätte are located in northeastern Illinois, a region which was along a paleocoastline when the fossils were deposited from 311-306 mya (Peppers, 1996; McCoy et al., 2016; Cotroneo et al., 2016; Clements et al., 2016; Clements et al., 2019). Given the low relief of this region of Illinois, the only natural exposures bearing fossils of the Mazon Creek Lagerstätte lie along the Mazon River itself (Clements et al., 2019) (Fig. 2.1). However, several coal mines operated in this area, and removed the Francis Creek Shale, the host rock to the Lagerstätte which overlies the coal, into large spoil piles, in which most of the fossil flora and fauna are found (Baird et al., 1986; Clements et al., 2019).

The Francis Creek Shale itself has been interpreted as a product of a delta system (Baird et al., 1986; Kuecher et al., 1999). During the late Carboniferous, the Mazon Creek localities were situated near the equator in a hot, humid environment along a paleocoast (Baird et al., 1986). Transgressive events during the Late Carboniferous associated with cycles of warming and glaciation contributed to the growth of an epeiric sea that inundated the Illinois basin, which served as the depositional basin for the Francis Creek Shale (Foster, 1998) (Fig 2.1). The shale itself has been interpreted as the product of a highly erosive river system entering this epeiric sea and forming a large delta (Baird et al., 1985; Baird et al., 1986; Foster, 1998; Clements et al., 2019). The Mazon Creek Lagerstätte itself is largely found within fossiliferous siderite

concretions found in the lower 3-8 m of the Francis Creek shale, although other fossils, mostly plants, are found outside the concretions (Baird et al., 1985; Baird et al., 1986; Foster, 1998; Cotroneo et al., 2016). These characteristic siderite concretions likely formed as organic material was rapidly buried in the delta under anoxic conditions, where sulfate-reducing bacteria consumed organic matter (Cotroneo et al., 2016). The fine-grained sediments burying deceased organisms would not be porous in the Mazon Creek, restricting the amount of sulfur available to sulfate-reducing bacteria decomposing the bodies of deceased organisms (Cotroneo et al., 2016). Therefore, these bacteria quickly reduced the sulfate available in these microenvironments around carcasses before reducing iron in the absence of sulfur (Cotroneo et al, 2016, Janssen et al., 2022). Collectively, these processes created a pH microenvironment and a localized area of reduced sulfur that preferentially mineralized siderite instead of pyrite, forming the characteristic siderite concretions (Cotroneo et al. 2016, Janssen et al., 2022). Generally, the combination of rapid burial, anoxic conditions, and concretion formation led to the exceptional preservation of flora and soft-bodied organisms, often found as whole, finely-detailed specimens, in this Late Carboniferous river delta (Baird et al., 1986; Cotroneo et al., 2016).

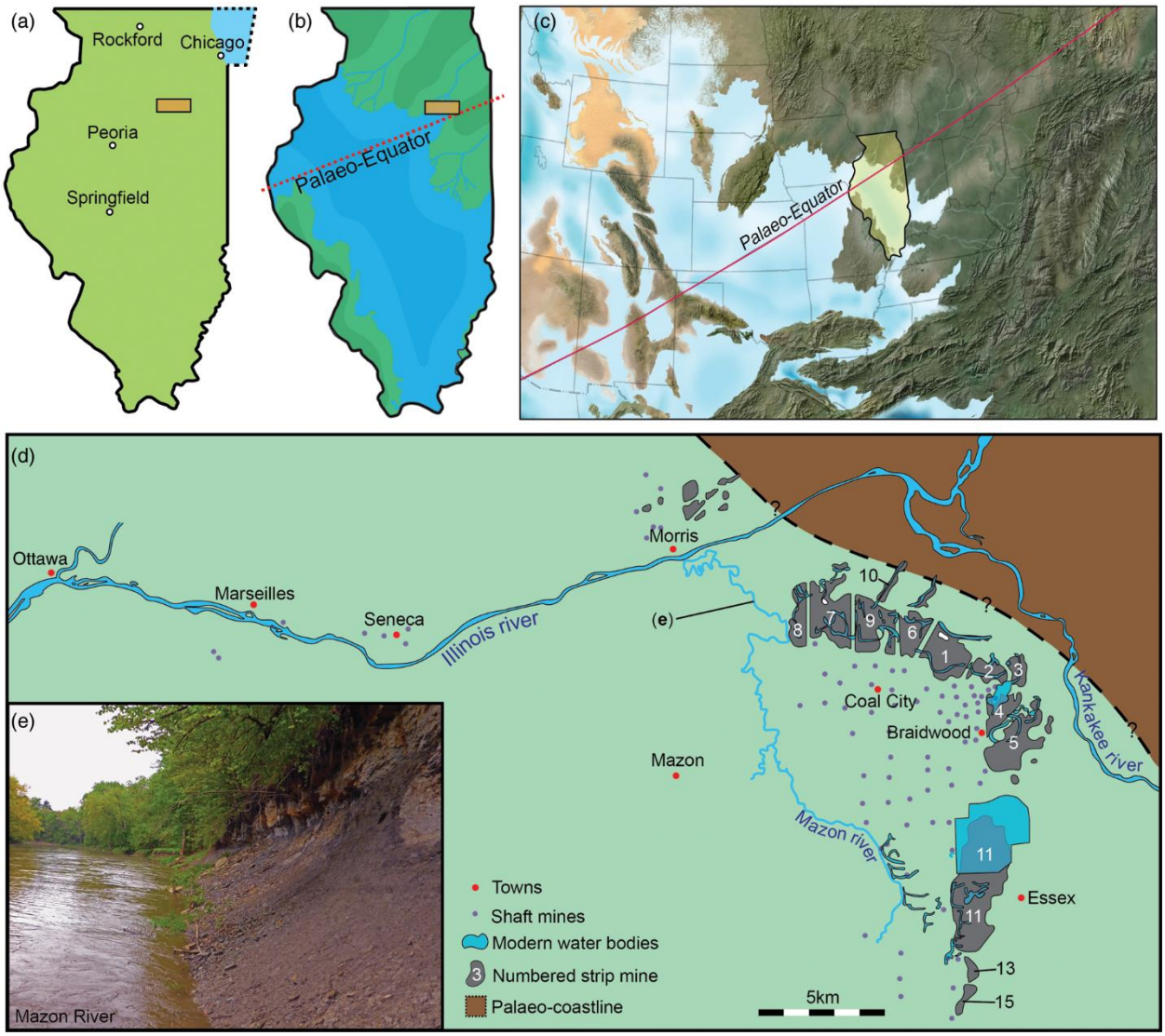

Figure 2.1: A figure placing the modern-day Mazon Creek Lagerstätte sites in the context of the Late Carboniferous Illinois from Clements et al., 2019**.** a) A map of modern Illinois with an orange box representing the area encompassed by d). b) A map of Illinois during the Late Carboniferous with an orange box representing the area encompassed by d). c) A map of the wider region during the Late Carboniferous with modern Illinois and the paleo-equator superimposed for context. d) A more detailed map of the Mazon Creek Lagerstätte sites themselves. e) An image of the Mazon River and its natural exposures of the Francis Creek Shale.

The Lagerstätte itself contains fossils from a range of interconnected habitats extending beyond the depositional environment of the delta, and ranging from a terrestrial, swampy forest to an offshore marine environment (Baird et al., 1985; Baird et al., 1986; Kuecher et al., 1999). Many of these organisms were transported into the delta by the same forces that transported the massive quantities of sediment that became the Francis Creek Shale. Previously, it has been assumed that a large terrestrial flood temporarily increased the sediment load of the river that fed the delta, rapidly burying the entire freshwater to marine ecosystem (Johnson and Richardson, 1966; Shabica, 1979; Baird et al., 1985; Baird et al., 1986; Foster, 1998). Alternatively, the river could have had a high sediment load that was stable over time, therefore burying organisms over a longer time span (Shabica, 1979; Clements, 2019). Sedimentological studies on the Francis Creek Shale suggest that the concretion formation was rapid and episodic, occurring in discrete pulses associated with different layers of concretions as the ecosystem was periodically buried by an influx of sediment (Kuecher et al., 1999). At the same time, other sections of the stratigraphy indicate that sedimentation was influenced by tidal cycles, suggesting more stable sedimentation (Feldman et al., 1993; Kuecher et al., 1999). Collectively, however, the site's depositional history remains somewhat contentious (Clements et al., 2019).

Stratigraphy of the Mazon Creek and the Francis Creek Shale

The Francis Creek Shale Member of the larger Carbondale Formation is a thick unit of shale that pinches-out to the south and to the West of the paleocoast in northeastern Illinois (Baird, 1979; Baird et al., 1986; Cotroneo et al., 2016, Clements et al., 2019). At its thickest, the Francis Creek Shale is roughly 25 m thick, and it thins to roughly 5 m thick as it pinches-out in distal regions from the paleocoast (Baird et al., 1986; Cotroneo et al., 2016; Clements et al., 2019). As the name implies, the Francis Creek Shale is dominated by laminated shales and

mudstones, although there is some variability between the shale layers (Baird, 1979; Baird et al., 1986; Cotroneo et al., 2016; Clements et al., 2019). Specifically, shales in the lower sections of the Francis Creeks Shale Member are composed of fine-grained clays without sedimentary structures (Baird, 1979; Baird et al., 1986; Cotroneo et al., 2016; Clements et al., 2019). More silty shales can be found with ripple structures as you move up through the section, and sandstone lenses with climbing ripples can be found near the top of the Francis Creek Shale (Baird, 1979; Baird et al., 1986; Cotroneo et al., 2016; Clements et al., 2019). On a smaller scale, individual layers of the Francis Creek Shale record tidal cycles with a cyclic deposition of fine-grained clay layers during slack water conditions and lenses of silt and sand deposited during more active tidal intervals (Baird et al., 1986; Kuecher et al., 1998).

The Francis Creek Shale Member itself directly contacts the underlying Colchester Coal Member, which has been interpreted as a nearshore, humid swamp environment (Baird et al., 1985; Clements et al., 2019). Given that the Colchester Coal Member represents as terrestrial nearshore swamp, the sharp transition from the Colchester Coal to the Francis Creek Shale represents a transgressive event that quickly flooded these swamp environments (Baird et al., 1985; Clements et al., 2019). As a result, the Colchester Coal does contain several prominent fossils, like large lycopod fossils preserved in-place during the transgressive event (Baird et al., 1985; Phillips et al., 1985; Clements et al., 2019). However, the fossil assemblages of the Colchester Coal are not considered part of the Mazon Creek Assemblages (Cotroneo et al., 2016).

Paleontological Assemblages

The concretions found at the Mazon Creek sites offer a fascinating window into a range of Late Carboniferous plant and animal communities (Baird et al., 1985; Baird et al., 1986;

Foster, 1998; Cotroneo et al., 2016; Clements et al., 2019). Traditionally, the Mazon Creek fossils have been separated into two assemblages, the Braidwood Assemblage and the Essex Assemblage, based on their inferred habitats and geographic distribution (Baird et al., 1985; Baird et al., 1986; Foster, 1998; Cotroneo et al., 2016; Clements et al., 2019).

The Braidwood Assemblage is comprised mostly of fossil plants, with some more rare insects, arachnids, freshwater organisms, and terrestrial vertebrates (Baird et al., 1986; Foster, 1998; Cotroneo et al., 2016; Clements et al., 2019). The localities that produce the Braidwood fossils are located closer to the paleocoast (Clements et al., 2019). Collectively, the assemblage of mostly terrestrial plant materials, terrestrial organisms, and freshwater organisms and the proximity of these sites to the paleocoast suggest that this fauna represents the products of wash-out events where parts of the terrestrial ecosystem and the freshwater delta system were rapidly buried close to the shoreline during flooding events (Cotroneo et al., 2016; Clements et al., 2019).

The Tully Monster is a member of the more marine-influenced Essex Assemblage (Richardson, 1966; Foster, 1998; Clements et al., 2019). The Essex Assemblage is mainly composed of soft-bodied fish and invertebrates interpreted to be marine/brackish organisms, and the localities that produce the Essex fossils are located farther away from the paleocoast than the Braidwood localities (Baird et al., 1985; Baird et al., 1986; Foster, 1998; Cotroneo et al., 2016; Clements et al., 2019). Due to its position farther away from the delta and its composition of marine/brackish organisms, the Essex fauna is interpreted as a nearshore marine fauna that was still influenced by the delta system and the delta's sediment load (Foster, 1998; Clements et al., 2019). Like those of the Braidwood Assemblage, the concretions that carry the Essex fossils

likely formed as flooding events temporarily increased sediment loads in the delta, rapidly burying parts of the ecosystem (Baird et al., 1986; Cotroneo et al., 2016).

While these two assemblages have been treated as separate freshwater and marine communities, a recent review of the literature argues that they comprise a unique deltaic community, the Essex Assemblage, and a separate terrestrial and nearshore community that washed-out into the delta and fossilized alongside organisms from the deltaic community, the Braidwood Assemblage (Clements et al., 2019) (Fig. 2.2). This study pointed to several discrepancies in the Essex Fauna, like the lack of corals, brachiopods, and trilobites typically found in contemporary Late Carboniferous marine assemblages, to suggest that the Mazon Creek Lagerstätte in its entirety represents a terrestrial community and a specific brackish water community in the nearshore environment near the shoreline (Clements et al., 2019). This certainly warrants more investigation and could affect interpretations on the Tully Monster's swimming abilities by altering our understanding of the Tully Monster's hydrodynamic environment. Modern delta systems have been shown to create separate riverine and brackish environments with distinct hydrodynamic conditions (Maicu et al., 2018), which may mirror the conditions in the Carboniferous at the Mazon Creek. Specifically, these somewhat isolated environments shift over time as flooding events and tidal cycles influence their boundaries (Maicu et al., 2018). These shifting boundaries and complex interactions create sub-environments, like brackish lagoons, which are also variable over time (Maicu et al., 2018). Further investigation into the sedimentology of the Francis Creek Shale and modern delta systems may provide insight into the sub-environments present in the Francis Creek Shale, and how they shifted over time as depositional conditions changed. This, in turn, could provide key insight into habitat range fluctuations that may have affected the Essex Assemblage organisms

while also providing insight into why siderite concretions are only found in the lower sections of the Francis Creek Shale.

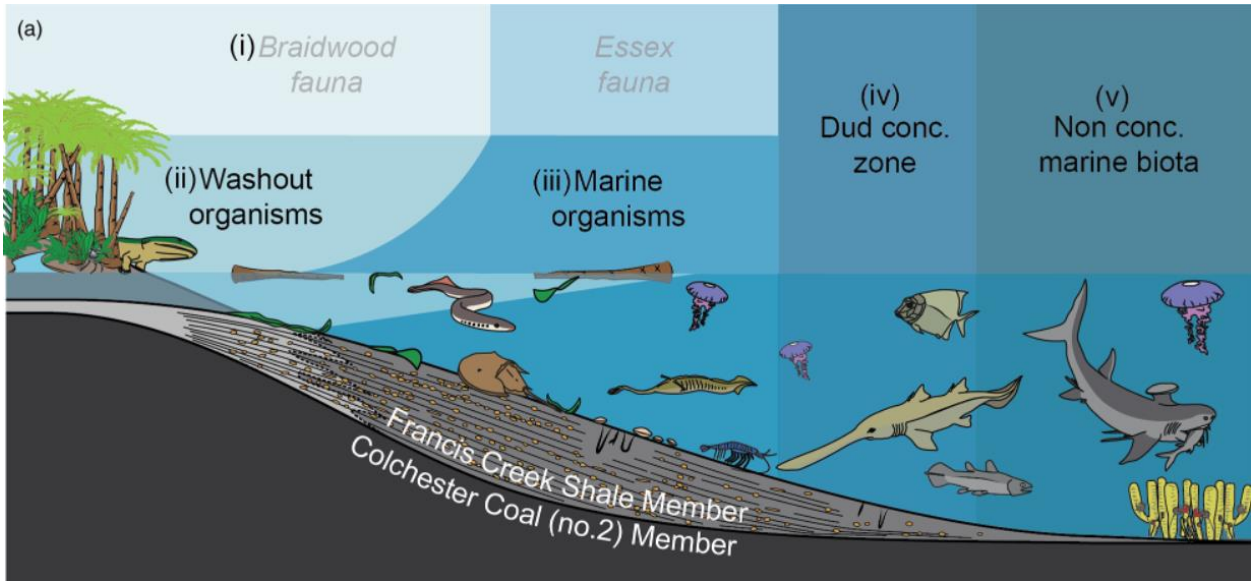

Figure 2.2: A panel from a figure in Clements et al., 2019 detailing the distribution of the Braidwood Fauna and the Essex Fauna in relation to the Francis Creek Shale deposits and other organisms found from related sites in deeper marine environments.

Chapter 3: Methods

Computational Modeling in Ansys Fluent

Computational fluid dynamics modeling in Ansys Fluent is a multi-step process that follows a prescribed workflow (Ansys, 2021). While this workflow can be modified, it is simpler to follow this process unless there is a specific step that needs to be added or subtracted to fit a project (Jiang et al., 2021). In this case, the standard workflow was appropriate for the aims of the 3D models used in this project, but was adjusted to meet the needs of the 2D modeling component. Generally speaking, the Fluent workflow is broken into 5 steps divided by the software used for each step (Ansys, 2021). (1) The process starts with model building in the Spaceclaim software, and then moves to (2) surface and volumetric meshing in a separate Ansys meshing program (Ansys, 2021). Once the model is meshed, the model is imported into Ansys Fluent automatically, where you set the parameters of the flow conditions and any solution constraints before Fluent calculates the solution as steps 3 and 4 (Ansys, 2021). Finally, the Fluent automatically imports the solution into the CFD-Post software, where results, images and plots are generated in step 5 (Ansys, 2021). This step can also be completed within the Fluent software, but CFD-Post offers more options and is easier to use. Here I expand upon each of these steps and detail the specific parameters used for each 3D model in this project. Then, I explain how the 3D models informed the 2D models, which were more accurate with more robust and less computationally intensive simulations, and how the solutions for the 2D models were calculated by modifying the same general 5-step workflow.

Step 1: 3D Model Construction in Ansys SpaceClaim

Spaceclaim is the modeling and design software nested within the Ansys umbrella, and it is therefore compatible with other Ansys programs (Ansys, 2021). Exploratory studies early in

the research process showed that models imported from other software face issues when they are prepared for programs in the Ansys suite; they are more difficult to manipulate and mesh in Spaceclaim and Fluent. I had originally imported a model generated by McCoy et al. (2016) into Ansys but converting this model into a file Ansys would recognize produced a model comprised of individual facets, or polygons, instead of curved faces and edges. Faceted models are often used by digital artists, and they are often highly realistic. However, SpaceClaim will not allow models without faces, edges, and vertices to be altered or manipulated, preventing this original model from being used in the analysis.

For this reason, new models had to be generated in SpaceClaim itself. Since Ansys is predominately used for engineering applications, the tools in SpaceClaim are designed to build larger, blocky geometries that can be more easily manufactured. These tools can be used to create curves and lines that flow more organically, but the software was not designed to create complex 3D animals. Therefore, each 3D model went through several iterations using different design tools and building strategies to best approximate the actual biological Tully Monster shape.

Approach 1: Rounding Method

The first approach involved attempting to sculpt a Tully Monster body shape from a rectangle by creating symmetrical rounded edges across the model. Ideally, each set of symmetrical rounds would create more edges that could also be rounded until you are left with a smooth circular body. In reality, each set of new edges created an increasingly complex model that tended to confuse the program, leading to automatic failures. In theory, only rounding one side of the model at a time could outmaneuver these errors. However, this would pinch the

opposite side of the model, creating uneven surfaces that could not be perfectly smoothed to be symmetrical. Ultimately, this approach was abandoned.

Approach 2: Sweep Method

The second model approach was more successful. Instead of carving the Tully Monster out of a central body, the main body of the 3D model (minus fins and other appendages) was built in smaller pieces by connecting circles and ovals together in a sequence. These circles and ovals were essentially 2D yx-plane cross sections of the Tully Monster body, which were placed along a line in 3D space normal to the yz-plane. These 2D yx-plane cross sections were then connected in the yx-plane by simple curves that followed the yx-plane profile of the Tully Monster. Once these curves were created in the sketch mode, they became faces and edges in 3D. SpaceClaim could then automatically connect the faces along these guiding curves creating a 3D volume with a suite of control points for each part of the curved 3D body. If the guiding curves narrowed too sharply between faces or curved too drastically (a particular problem in the posterior of the Tully Monster model) the process would fail. In these instances, additional 2D cross section with new guiding curves could be added to solve the issue.

Once the main body of the Tully Monster was generated, the dorsal and ventral fins were generated in 2D. These fins were constructed as single faces attached to the previously generated body by drawing the outline of the connected to the body in the yz-plane. These outlines were then thickened into full 3D fins by pulling each side of the face symmetrically along the x-axis to the desired thickness.

The horizontal eyebar was also added onto the generated 3D body as a separate component. A cylinder with the desired eyebar radius was generated and placed onto the body at

the appropriate spot and extended to the desired dimensions. Spheres were then placed as closely to the center of each side of the cylinder to generate eyes.

The elongate anterior proboscis was also added to the main body as a separate component, but its construction was more complicated than any of the other features. Initially, I tried the same method as for the main body – using 2D cross sections connected into a 3D structure along guiding curves. However, the proboscis guiding curves narrowed too sharply/curved drastically, due to the various bends of the proboscis. Additional cross sections could not solve the problem here because the proboscis bends were too sharp. Instead, the proboscis shape itself was created from intersecting simple cylinders generated from circular cross sections and straight guiding lines, which prevented the program from becoming confused. However, it did create sharper bends in the proboscis than the Tully likely had in life. Ultimately, this issue could not be addressed using this modeling approach, but these sharp bends were addressed in later modeling approaches. This method was also incapable of merging the relatively larger faces of the grasping apparatus with the smaller cross section faces of the proboscis. Instead, the grasping apparatus was drawn separately in 2D using simplified, blockier shapes that were thickened to the desired dimensions in 3D.

Merging the completed proboscis with the body was also problematic, however, since the program viewed the body and its attachments as a separate 3D object than the proboscis. So, I simply extended the cylindrical face on the proboscis closest to the body into the flat anterior face on the Tully Monster's body. This created 2 overlapping bodies that were recognized as separate objects by the software. Since they were separate objects, these two bodies could not be merged into a singular body in the software. This model-building approach was also incapable of merging faces along the proboscis into faces on the grasping claw. Instead, the claw itself had to

be built separately from the proboscis using 2D blocky shapes that were thickened until they formed the desired 3D structure. The proboscis was then slightly extended to overlap the claw structure and the bodies were merged so the software recognized them as a single object. Unlike the failed merge between the body and the proboscis, the claw itself was not automatically viewed as a separate object in the SpaceClaim software.

While the model generated by this approach was complete and mostly accurate, it generated several undesirable downstream errors later in the CFD workflow due to hidden errors and complex regions in the original 3D model. For example, the overlap between the proboscis and the body objects could be ignored in the meshing software, but the strange connection point between objects forced the software to mesh one body while ignoring the other unless these sites were designated as "bonded." Even if they were bonded, the highly accurate automatic meshing method would not work, and a less accurate meshing algorithm had to be used. Additionally, building and thickening the tail fins as an attachment onto the curved 3D body generated several fatal errors. Thickening these fins forced the tail fins to serve as cutter faces in the software, essentially pulling apart the already generated body as they were thickened. This was an issue specifically with the main body as generated by the above approach: it was generated as one large face with many different facets. This singular complex face had a wide array of individual control points to control the variable shape of the curves on the face, which already tended to confuse the program as they were adjusted. Cutting these points with the tail fins generated several tiny faces within the rip in the body that were within the 3D volume of the tail fin, yet were still identified as part of the body face by the program. These faces were completely undetectable unless the tail fins were deleted, and they would result in tiny volumes that would

confuse the Fluent software in later steps. Therefore, in order to continue beyond model building into hydrodynamic modeling, I moved on to a third approach.

Approach 3: Blend Method

A third and final model building approach was implemented to solve these issues. Instead of building the models by connecting the 2D cross sections along user-generated guidelines, I connected them using a tool that infers its own guide lines. This reduces the amount of control points organizing the new 3D geometry in the software, resulting in an accurate and less complex curved surface. By default, this approach creates a curved, organic transition between oval or circular faces, either widening or pinching the 3D shape to ensure a smooth transition between faces. This greatly simplified the construction of the Tully Monster's tubular body. More complex areas in the model, like the slight downturn at the posterior end of the Tully Monster's body, could also be added to the main body separately to prevent excessive pinching or widening of these regions.

Once the body was generated, the tail fins were built separately following the same approach as before, but initially built above the model in 3D space. Since the tail fins generated for approach 2 were accurate, the 2D xy-plane faces of fin models from approach 2 were copied and pasted in the space above the blended model's body. Once these faces were pasted into approach 3, any split curves along the edge of the fin face curves were repaired to make cohesive faces. These faces were then thickened into actual 3D fins by using the pull tool. Once they were fully constructed, each tail fin was moved down onto the model. During this process, the "no merge" option was selected to prevent the tail fins from automatically splitting the body. Once the tail fins were in place, they were merged using a tool that eliminates any part of the tail fins that would have been inside the body, avoiding the issues the previous model generated.

Since the eyebar was generated using simple shapes in previous models, it did not generate any strange issues in the body like the tail fins did. Therefore, it was once again built from the same cylinder and spheres. In this case, the eyebar was automatically recognized as part of the body object.

This approach also simplified the construction of the proboscis. In this case, circular cross sections were placed and tilted in 3D space to outline where the proboscis should be. These cross sections were then connected using inferred straight guidelines, which prevents the software from generating pinched or widened sections along part of the blend. The proboscis was built using the same set of tools as the body, and so could be easily connected to it. However, the proboscis was not connected to the body until the entire proboscis was finished to avoid any issues that would prevent the proboscis and the body from being recognized as a single object in the software.

Once the proboscis itself was built, the proboscis grasping apparatus was generated separately with blocky, simple shapes using the same methods used when it was generated in previous models. However, the blend tool allows blends to be generated from the rectangular faces on the posterior of the grasping apparatus to the proboscis itself, which helped simplify the proboscis. Once the grasping apparatus was generated and attached to the proboscis, any unnecessarily sharp angles at joints were smoothed by adding small spheres to these regions using the sphere tool. Finally, the combine tool was used to ensure the entire proboscis was a single object, and the entire proboscis was moved into position and blended onto the Tully Monster body.

Once the core model was built, variations on it with different proboscis positions were generated using the same approach. These models were based on the original model, and the

proboscis was the only part of the model that was modified to generate each variation. In each case, the model was split to isolate the proboscis and the grasping apparatus. The tube-like sections of the proboscis were then deleted, and the grasping apparatus was moved to its intended position for the specific model being built. The grasping apparatus was connected to the main body after proboscis cross sections were placed in an outline of the intended proboscis position. Finally, the model was once again combined into one object.

Final model and variations

Four 3D models were generated using the blend method with different proboscis positions (Fig 3.1). The typical reconstruction represents the proboscis position previous authors have used in their reconstructions and seen frequently in popular media (Johnson and Richardson, 1969; McCoy et al., 2016) while the other three models represent biologically feasible variations based on fossil evidence and inferred joint flexibility (McCoy et al., 2016). For example, the grasping apparatus seems to be held at a consistent 130° angle relative to the proboscis in all Tully Monster specimens with a preserved proboscis (McCoy et al. 2016), so all of the reconstructions have the proboscis with the oral apparatus held at this angle. Three more models were generated based on hypothetical proboscis positions. Specifically, a model where the proboscis was fully folded underneath the anterior portion of the body to reduce drag and a model with the proboscis fully extended with locked joints straight in front of the body to reduce drag were constructed for this study. A final fourth model with the proboscis folded under the body and lowered below the body was also constructed to assess whether proboscis positions that didn't fall roughly along the xy-plane centerline of the body were feasible.

Tully Monster specimens range drastically in size (Johnson and Richardson, 1969; Foster, 1998; McCoy et al., 2016), so the resulting models were built to fall within this size range

and follow general proportions across Tully Monster specimens. The resulting models were approximately 115 mm long from the posterior point on their tail to the anterior oval face where the proboscis was merged to the body, and the proboscis was 30 mm long from its attachment point to the body to the anterior edge of the grasping apparatus. The models' bodies were and were 16 mm wide from left to right at their thickest point on the body, 110 mm long from the attachment of the proboscis to the farthest posterior point on the body, and 18 mm deep from the anterior to ventral points at the widest point of their bodies. This would place the models towards the middle of the known Tully Monster specimen size range (Johnson & Richardson, 1969, McCoy et al., 2016).

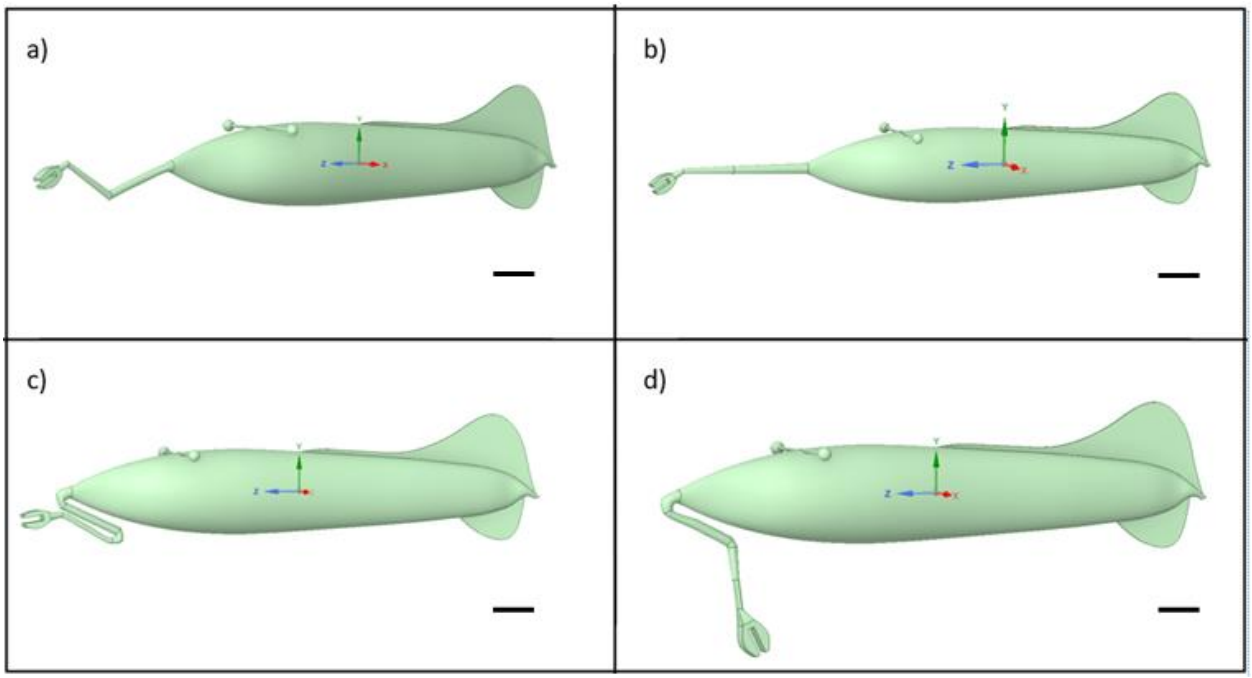

Figure 3.1: The 3D Tully Monster models with various proboscis positions, built using the blend method, used in this study. a) The typical reconstruction model, with the proboscis held in a bent, relaxed position in front of the body. b) The fully extended model, where the proboscis is fully extended in front of the body. c) The fully folded model, where the proboscis is folded at each joint and tucked closely under the anterior portion of the body. d) The folded and lowered model, where the distal part of the proboscis is extended downward from the fully folded position. Scale bar = 10 mm

Once the models were generated and checked for errors, a large tube was drawn around each of them to prepare for the next steps in the Fluent workflow. The tube was intentionally much larger than the Tully Monster, with a 200 mm diameter and a 300 mm length, to model the flow around the Tully Monster in the following steps 2-5 (Fig. 3.2). Modeling a tube space larger than the model itself ensures that the effects of the simulated flow on the 3D body are not affected by any interactions between the flow and the tube wall, or any interactions that can happen within the flow itself by chance (Jiang et al., 2021).

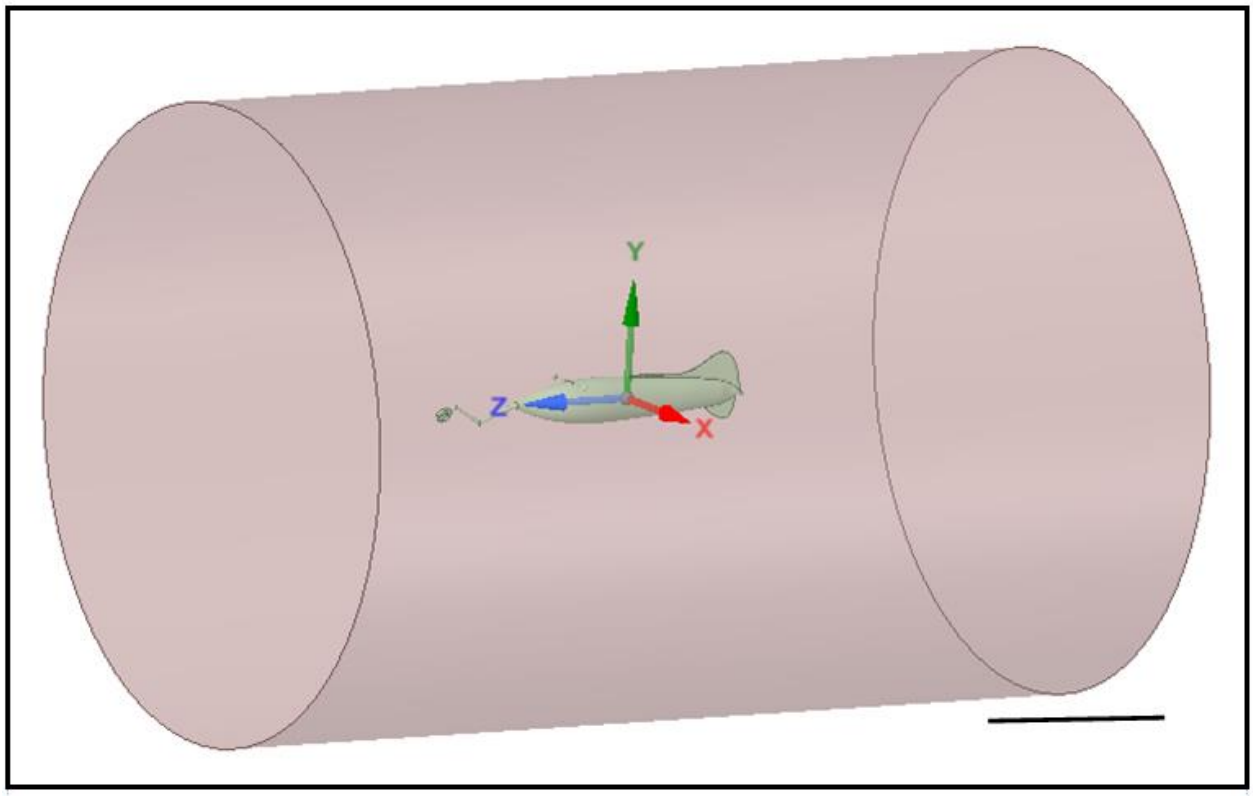

Figure 3.2: An image of a finished 3D model (the typical reconstruction model) with the full 3D tube shown. Scale bar = 100 mm.

Step 2: 3D Volumetric Meshing

Once the models were built, checked for errors, and placed in a tube, they were imported into the Ansys meshing software to generate volumetric meshes. Volumetric meshes create a grid of small polygons across an object to calculate fluid action and forces across that region of the object. These polygons extend inside the 3D space of the object to mesh the entire object's volume and surface in a mosaic of polygons. The size and density of these polygons can be altered to get a finer-scale solution in targeted regions of an object, and different meshing algorithms can be used to adjust the mesh for specific purposes. In most cases, however, the automatic methods are adequate, so the automatic method was used to mesh the models in this study.

Before generating the mesh, names are assigned to any faces that need to be easily found in Fluent later in the process. In this case, the face of the tube towards the anterior of the Tully Monster was named the inlet, the opposite face of the tube was named “outlet” and the walls of the tube were named “shearwall.” The Tully Monster model itself was named “Tully”. At this point, the model was checked in the meshing program to ensure it was recognized as one solid object in the program without any detected connections.

Once all of the faces of interest were named and the connections were checked, the mesh was generated. In this study, the automatic method was sufficient to mesh the 3D bodies with enough resolution. However, the Tully Monster model was meshed more densely than the tube, and certain smaller parts of the Tully Monster model, like the eyebar and the proboscis, were meshed more densely still, which was desirable since these features likely had a disproportionate effect on the flow (Patil and Jeyakarthikeyan, 2018; Ansys, 2021) (Fig. 3.3). Once the settings were set, the mesh was generated and automatically imported into Fluent for the next steps in the workflow.

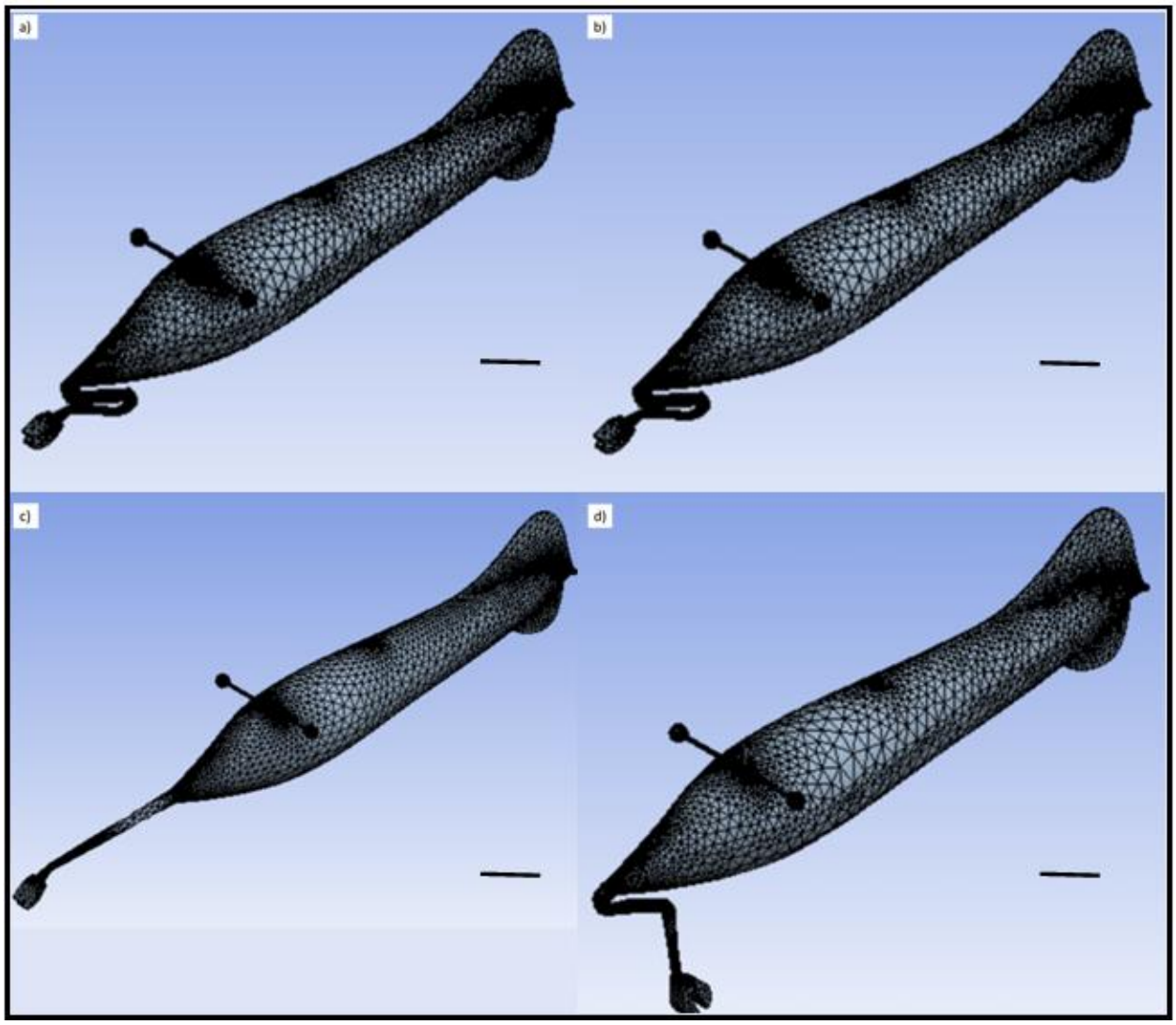

Figure 3.3: The finished 3D meshes of each model. a) The mesh for the typical reconstruction model. b) The mesh for the fully folded model. c) The mesh for the fully extended model. d) The mesh for the fully folded and lowered model.

Steps 3-4: Fluent Setup and Solution Calculation

The Fluent software allows users to import meshes, setup calculation activities, and calculate solutions. While Fluent can be used to model everything from liquid batteries to internal combustion engines, it is organized to analyze a simple flow by default. Therefore, there

are minimal inputs required for this analysis, and there are no specific models that need to be applied for these calculations.

Upon opening Fluent, the program asks users to designate whether the user would like to use double precision, and how many GPUs the user would like to designate for the calculation. For this project, all calculations used double precision to reduce errors and 3 GPUs to speed-up calculations. Once these parameters are set, the user is able to modify several other parameters. For this study's 3D solutions, the solutions were calculated as steady-state calculations, where the model does not move and individual pulses of flow do not interact with each other significantly. Steady-state solutions are generally considered adequate for simple, static applications, and they are less computationally intensive then transient solutions (Patil and Jeyakarthikeyan, 2018; Ansys, 2021). The flow was also set to be composed of liquid water at 298 K, since the Tully Monster was aquatic.

Once these basic parameters were set, specific conditions at the model walls were set. Flow velocity at the inlet, was set to 0.1 m/s, or roughly a body length per second. The shear condition at the shearwall (the walls of the tube) were set to specified shear to eliminate the tube's effect on the flow. While the outlet was defined as an outlet, no outlet parameters were changed for the 3D calculations. Before initializing the solution and running the calculation, the reference values were also checked to make sure they reflect the properties of water and not the properties of air, and the reference temperature was set to 298 K, or 25° C.

Once these parameters were set, the solution was initialized. All of the parameters were set to 0 under the initialization tab except for the z-velocity value. This value was set to 0.1 m/s to match the inlet velocity. The solution was also set to compute from the tube, which ensures the flow begins from the tube's inlet. At this point, the solution can be initialized, and specific

calculation activities can be designated. In this case, the calculation was set to autosave at every iteration and the simulation was set to execute 80 iterations. As the calculation ran, several simulations might terminate early if the solutions converge. In this case, 80 iterations tended to be sufficient to calculate an accurate, converged solution.

Fluent Tab	**Specific Input**
Opening Fluent	Double Precision with 3 GPUs
General	Steady-State Solution
Materials	Change the fluid material to water
Boundary Conditions: Inlet	Set the velocity at inlet to 0.1 m/s
Boundary Conditions: Wall	Set "shearwall" to specified shear
Boundary Conditions: Outlet	Ensure the "outlet" is designated as an outlet
Reference Values	Ensure the values relate to the properties of water and set temperature to 298 K, set reference frame to the "tube" object
Initialization	Set to standard initialization and make sure all values are 0 except for z-velocity, set z-velocity to .1 m/s, initialize
Calculation Activities	Set iterations to 80
Calculation Activities	Run calculation

Table 3.1: A list of specific inputs used in Ansys Fluent for the 3D solutions, organized by tabs in the Fluent software.

Step 5: Results Post-Processing in CFD-Post

Once the solution was calculated, the CFD-Post program could be opened to view the results and generate figures. By default, CFD-Post does not show any of the calculated results and only displays a simplified image of your model. However, selecting different visualization options allows the user to generate different figures that can be layered onto the wireframe or the volumetric model. In this case, the velocity vectors acting on the 3D model and the fluid pressure across the model's body were the most relevant visualizations. In both cases, results images were only generated for the Tully Monster model instead of generating images for the tube walls, the inlet, and the outlet along with the model body. Since the flow area itself was not meshed for the

3D models, the program considered any vectors or gradients in these non-body regions to be homogenous, and they did not inform the results. Instead, velocity vectors were generated using the default colors and sizing across the model's body, and pressure gradients were generated across the model's body using the default color scheme. Due to their small size, velocity vector magnitudes were extended by a factor of 10 in the results images to increase their visibility.

Once each of these visualizations were generated, they were layered onto the volumetric model and a final image was captured. The final images were taken of the entire model from a point slightly offset from the yx-plane view. Each model was slightly turned towards the screen to avoid obscuring the vectors generated by the eyebar. While there was no default view used to standardize these images, each model was placed in approximately the same position and the models were not tilted up or down (Fig. 3.4).

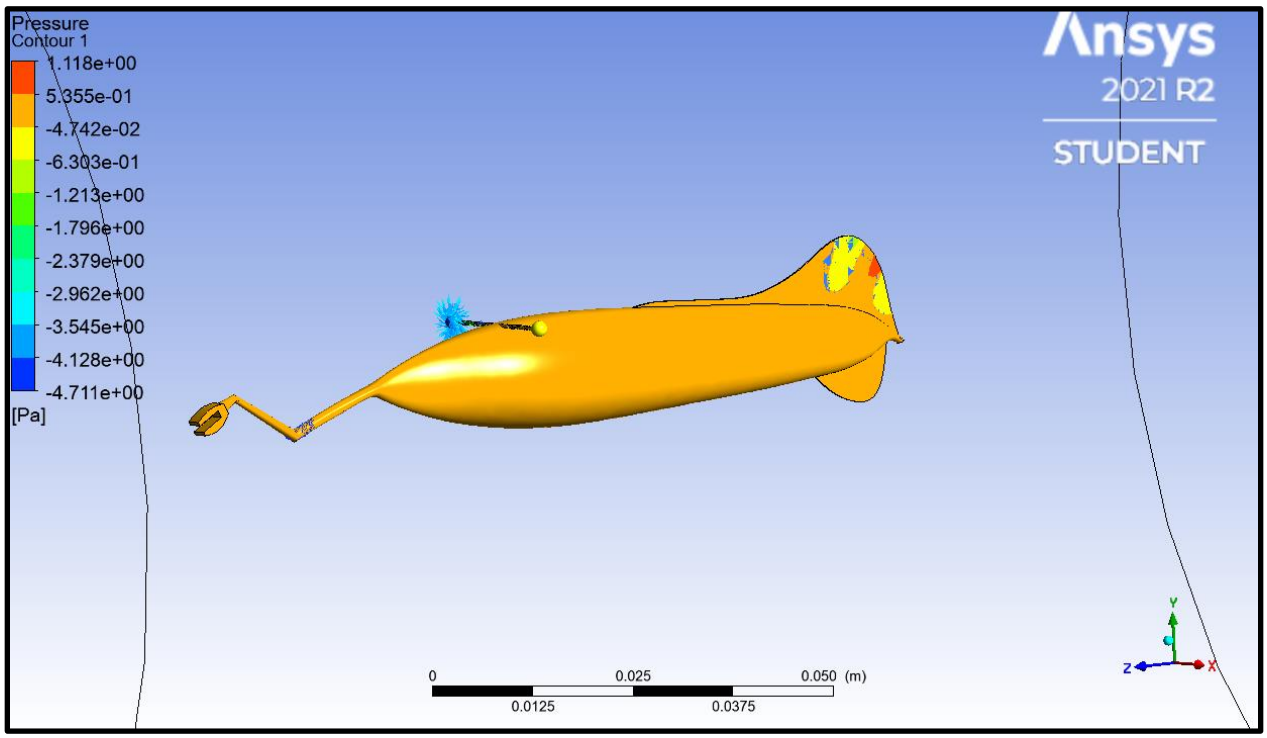

Figure 3.4: An example of the data visualization generated in Ansys CFD Post for the typical reconstruction model, with pressure gradients and z-velocity vectors layered onto the model.

Variations for the 2D Workflow: 2D Profile Generation

Given the restrictions on meshed element numbers within the Ansys Student software (Ansys, 2021), simulations of a 2D flow around profiles of different Tully Monster models were far more accurate than 3D models (Patil and Jeyakarthikeyan, 2018). However, these 2D profiles could not capture certain hydrodynamic characteristics of morphological structures like the eyebar, and the 3D models acted as a base to generate the 2D profiles. Therefore, the 3D models were still essential to this study, even though their solutions were not as accurate as the 2D solutions.

Two 2D profiles were generated for each 3D model, one yz-plane profile, named side profiles for simplicity, with a lateral view of each model and one yx-plane profile, named top-down profiles for simplicity, with a dorsal view of the model. A dorsal view was chosen instead of a ventral view for the top-down profiles since a dorsal view captured the eyebar while a ventral view would ignore the eyebar. These profiles were generated in SpaceClaim and the overall workflow for each simulation was similar to the five-step Fluent workflow used for the 3D models.

To generate these 2D profiles, the 3D model was loaded into SpaceClaim, the tube was deleted, and sketch mode was opened with the sketch plane centered on the yz-plane or the yx-plane from the origin. Then, I outlined the profile of the 3D model, using the visible 3D model as a stencil. In most cases, this could be done automatically to create a nearly identical profile to the outline of the 3D model. The only differences originated from small, sharp bends near the grasping apparatus of the proboscis where sketching tools automatically smoothed some sharp corners. These differences were very minor, however, and should not be significant in the simulations.

The side profiles could be directly outlined, but the top-down profiles required some minor extra steps since there was not a single yx-plane in each 3D model that intersected the grasping apparatus, the proboscis, and the eyebar at the same time. Instead, the sketch view was locked to the yx-plane and these structures were outlined as closely as possible based on the yx-plane view. Once the profile was generated, unneeded curves or lines were removed to prevent SpaceClaim from recognizing multiple faces in the profile.

Once a profile was generated, the 3D model was deleted and a rectangle was built around the 2D model, creating a 2D image that would be analogous to a 2D view of a 3D tube. Since each model varied in size, each bounding rectangle varied in size to encompass a space ten times larger than the profiles' maximum dimensions, ensuring that any interactions in the flow around the body were captured accurately and did not interact with the arbitrary walls of the bounding box (Jiang et al., 2021). For the side profiles, the bounding rectangle was 1200 mm wide and 400 mm deep. Similarly, the top-down profile bounding rectangles were pulled 1200 long and 400 mm wide to ensure there was adequate space around the models (Fig. 3.5).

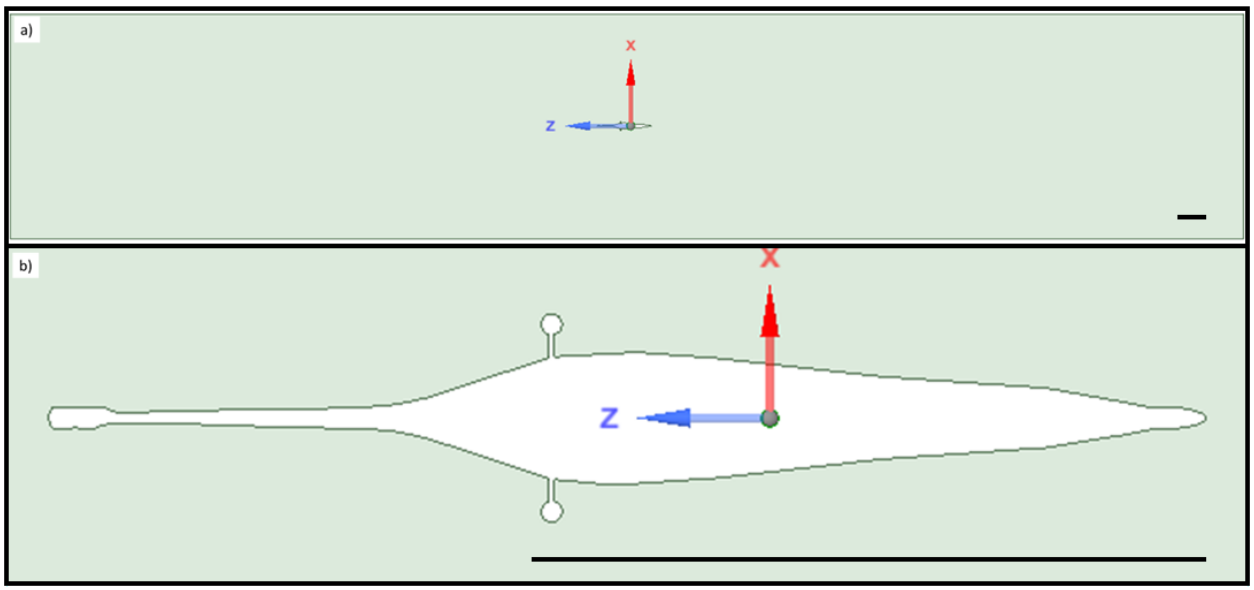

Figure 3.5: An example of a finished yx-plane 2D model with its bounding box to demonstrate the relative size of the model and the bounding box. a) An image of the entire 2D model. b) A close-up image of the Tully Monster top-down profile within the larger model. Scale bars = 100 mm.

Once the profiles and bounding rectangles were bounding box was split using the profile as a cutter face. This generates a surface with the entire bounding rectangle's area with a profile-shaped hole cut into it. This surface is the desired final surface for the 2D workflow, so any extra or duplicate faces were deleted at this point, including the original 2D profile (Fig. 3.6 and 3.7).

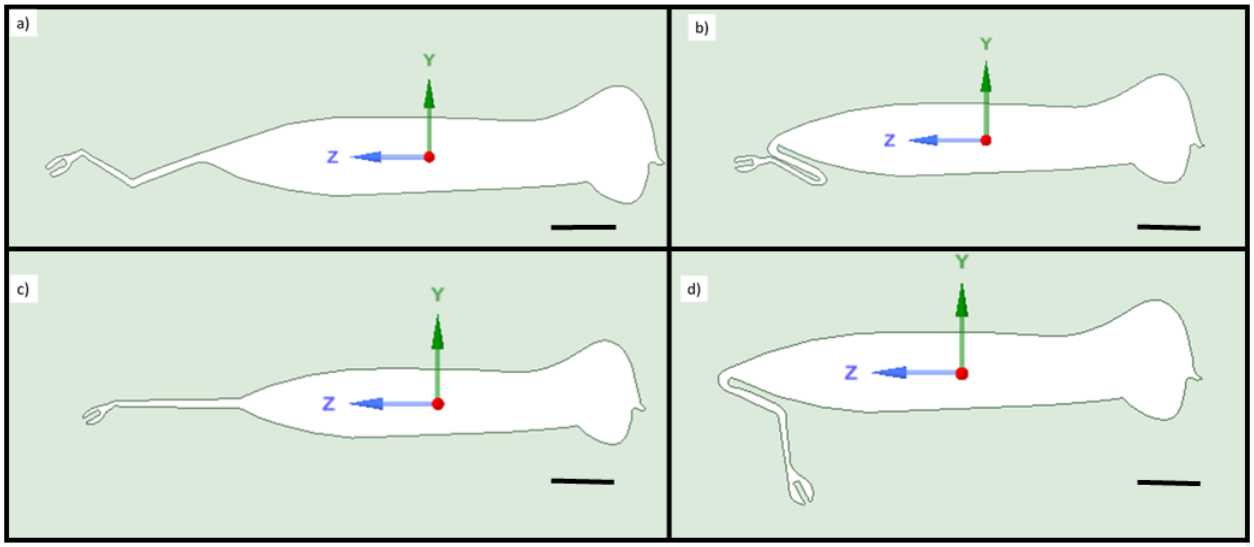

Figure 3.6: The 2D side profiles used in this study. a) The typical reconstruction model. b) The fully folded model. c) The fully extended model. d) The fully folded and lowered model. Scale bars = 10 mm.

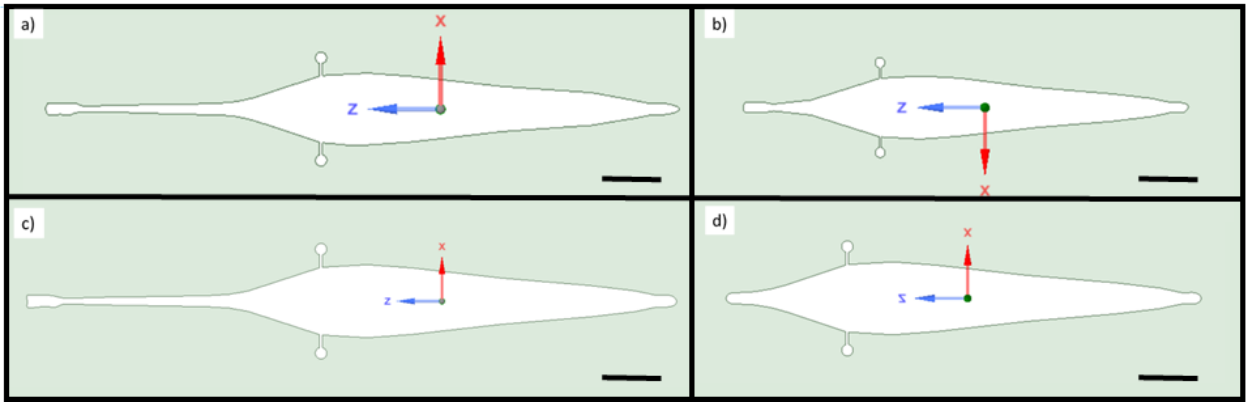

Figure 3.7: The 2D top-down plane profiles used in this study. a) The typical reconstruction model. b) The fully folded model. c) The fully extended model. d) The fully folded and lowered model. Scale bars = 10 mm long.

Variations for the 2D Workflow: 2D Meshing

Meshing the 2D profiles required several variations compared to the 3D workflow to ensure that the mesh had an adequate resolution in the boundary region (Patil and Jeyakarthikeyan, 2018) near the profile itself. Determining what constitutes an adequate

resolution in a mesh is often qualitative, but, generally, a denser mesh around small structures that blends smoothly into a less dense mesh elsewhere in the model provides adequate resolution for most calculations (Patil and Jeyakarthikeyan, 2018). Similar to the 3D workflow, named edges were defined as named selections before beginning the meshing process. In this case, the inlet and outlet were named the same way they were in the 3D model, and the two other edges of rectangular flow field were selected together and named "shearwall." The edges composing the Tully Monster profile were also selected and named "Tully."

Once the named selections were established, the meshing algorithm was altered for the flow field. The triangle mesh method was selected to provide a denser mesh near the profile (Jiang et al., 2021), since individual triangles could be stacked together to form sets of perfect outlines radiating from the body region. An edge sizing function was also applied to the Tully Monster profile. The element size near this edge was set to 0.0001 in all of the 2D profiles. An inflation was then added to this edge sizing to expand the denser edge mesh farther from the profile. In this case, the profile edge was set as the "boundary" in the inflation, and the inflation itself was set to "first layer thickness" with a growth rate of 2.5 and 10 maximum layers. This extended the fine scale mesh with a 0.0001 element size at the edge 10 layers away from the body, creating a densely meshed boundary layer. Finally, the universal element size was set to 0.1 to make the overall mesh denser in regions farther away from the profile (Jiang et al., 2021) while still ensuring the mesh smoothly transitioned from the densely meshed area near the profile into the less densely meshed flow field. This ensured that regions closer to the body profile where the flow was likely to interact with itself as particles are deflected around various structures was meshed more densely than regions farther away from the body profile, where the

flow was likely to be uniform. At this point, the mesh was generated and exported to the Fluent software (Fig. 3.8 and 3.9).

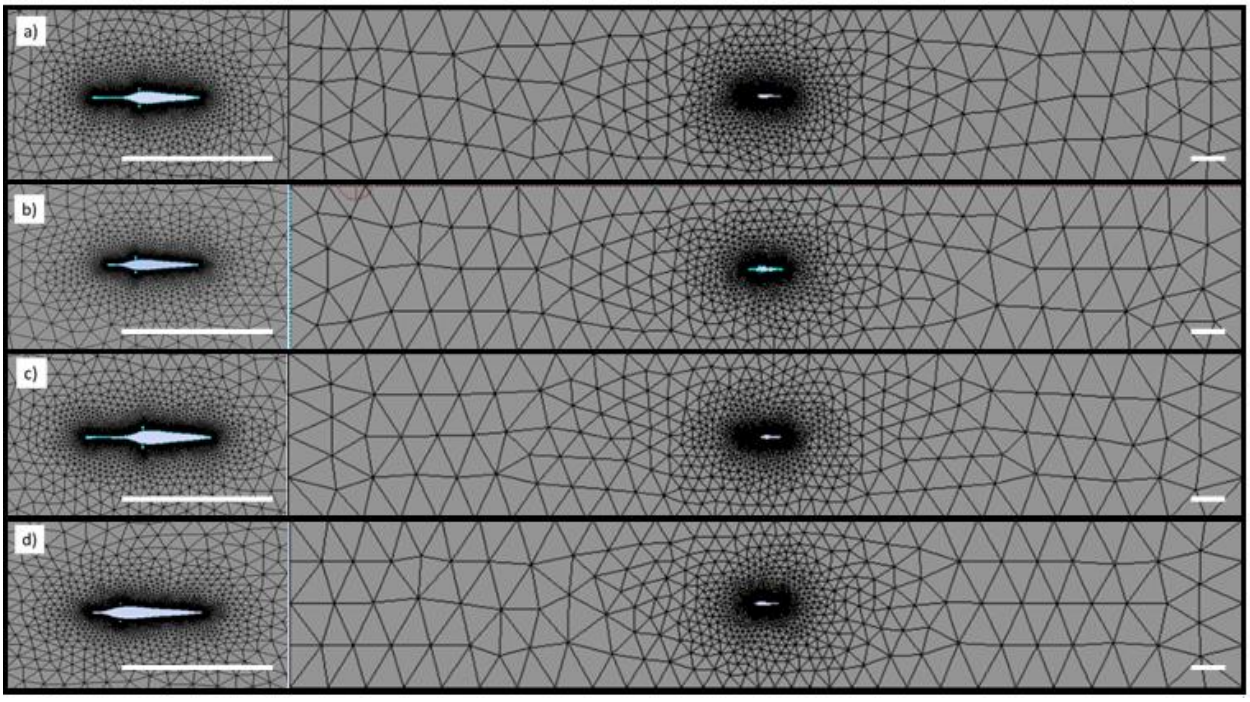

Figure 3.8: The completed 2D top-down meshes for all of the models, with a zoomed-in view and a view of the full mesh. a) The mesh for the typical reconstruction. b) The mesh for the fully folded model. c) The mesh for the fully extended model. d) The mesh for the fully folded and lowered model. Scale bars = 100 mm

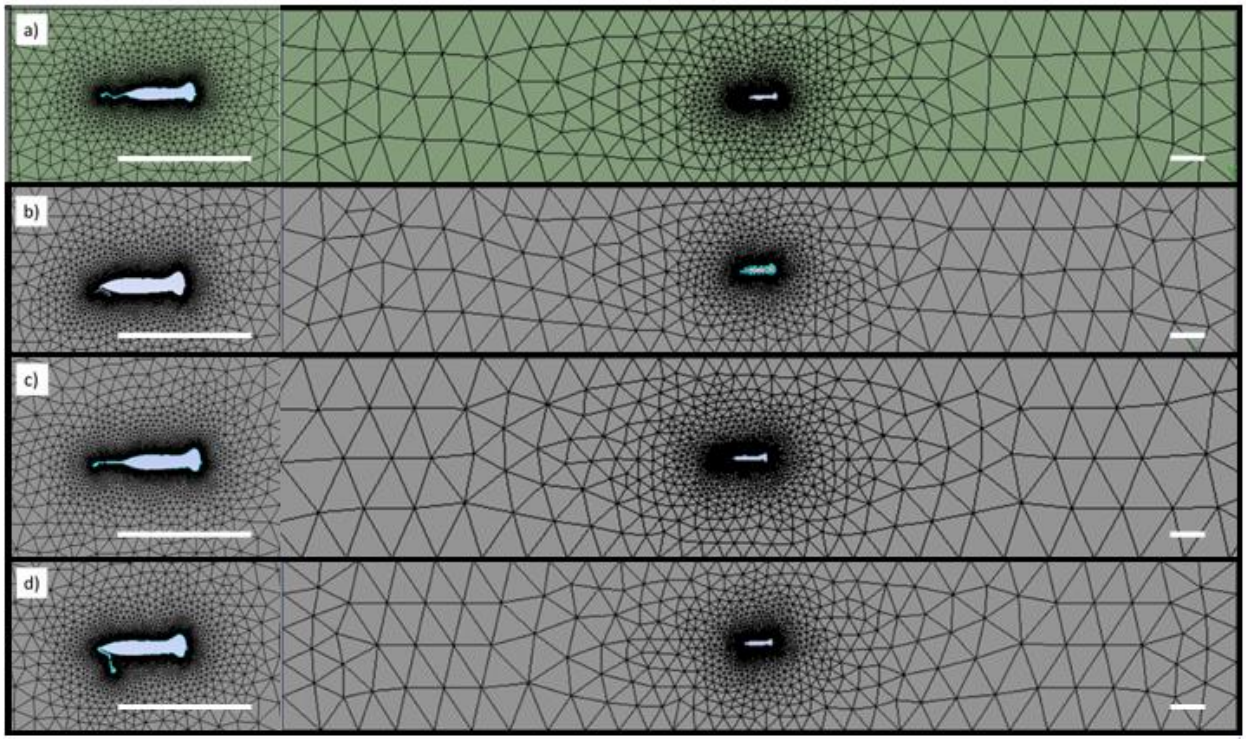

Figure 3.9: The completed 2D side profile meshes for all of the models, with a zoomed-in view and a view of the full mesh. a) The mesh for the typical reconstruction. b) The mesh for the fully folded model. c) The mesh for the fully extended model. d) The mesh for the fully folded and dropped model. Scale bars = 100 mm

Variations for the 2D Workflow: Transient Solution Workflow in Fluent

Several Fluent parameters differed between the 2D workflow and the 3D workflow. Primarily, the 2D workflow used the transient solution instead of the steady state solution. Transient solutions can be used to assess how the flow around an object changes over a set period of time instead of simply analyzing the instantaneous effects of the flow as it first interacts with an object. In this case, the interactions in the flow downstream from the Tully Monster were more interesting than the instantaneous effects on the flow from the Tully Monster's body, so a transient solution was chosen instead of a steady-state solution. These flow

interactions shift slightly over time as initial turbulence generated by the model interacts with the surrounding fluid flow. These interactions would not be clear without using the transient solver.

Like in the 3D workflow, double precision was selected upon opening the Fluent program and 3 GPUs were assigned to the program. The 2D option did not have to be selected since the program automatically recognizes that the model is a 2D model. The transient time option was selected instead of the default steady state option. Like in the 3D workflow, the fluid material was water and the cell zone conditions were set to use water as a fluid instead of the default air option. The inlet velocity was set to 0.1 m/s, like in the 3D workflow, and the outlet was defined as an outlet zone by default.

The transient solution was set as "second order implicit." Once the method was switched to second order implicit, the solution was initialized using the hybrid initializer. Unlike the standard initializer, the hybrid initializer does not require the user to input any values before initializing the solution. Finally, the calculation activities were defined before calculating the solution. The transient solver runs a defined number of simulations, called timesteps, of the same scenario and the average solution is then displayed. The length of each time step can be changed, along with the number of overall time steps and the number of iterations per time step. Unlike the steady state solutions, transient solutions will never converge, so running a larger number of time steps with several iterations helps reduce overall error for the final solution. In this case, the calculation used 100 time steps, and the time steps were set to 1 second. Each time step was also iterated 20 times. These parameters were chosen after several test simulations to determine which combination of parameters produced low error values without being overly computationally intensive. Once the solution was calculated, the results were visualized in CFD Post using the same methods used in the 3D workflow.

Fluent Tab	Specific Input
Opening Fluent	Double Precision with 3 GPUs
General	Transient Solution
Materials	Change the fluid material to water
Boundary Conditions: Inlet	Set the velocity at inlet to .1 m/s
Boundary Conditions: Wall	Set "spshearwall" to specified shear
Boundary Conditions: Outlet	Ensure the "outlet" is designated as an outlet
Solution Methods	Set the solution to 2nd order
Initialization	Set to hybrid initialization and initialize
Calculation Activities	Set time steps to 1 sec, iterations to 20, and number of time steps to 100
Calculation Activities	Run calculation

Table 3.2: A list of the inputs used in Ansys Fluent for the 2D solutions, organized by individual tabs within the Fluent software.

Comparisons to extant fish

The Tully Monster's anatomy was also compared to extant fish to inform the discussion of the CFD results. Specifically, the Tully Monster was compared to sling-jaw wrasse (*Epibulus insidator*) wrasse and elephant nose fish (genus *Campylomomyrus*) documented in videos and images to inform hypotheses regarding the function of the proboscis. The Tully Monster's anatomy, detailed by McCoy et al. (2016) was also analyzed to speculate on swimming mechanisms. Specifically, myomere locations along the Tully Monster were compared to myomere placements on other extant fish.

Chapter 4: Results

Overview of 3D Modeling Results

3D CFD modeling in this study was lacked the resolution to calculate the effect of the Tully Monster's body on the flow around it due to the calculation limits of the ANSYS Student software (Ansys, 2021). Instead, 3D modeling provided a broad picture of the hydrodynamic effects of anatomical features like the proboscis, the eyebar, and the tail fins (Dec, 2019). Specifically, the eyebars in each of the 3D models generate velocity vectors in multiple directions, with the largest magnitude velocity vectors pointed in the positive y direction (up relative to the body). Similarly, the proboscis in each model generates velocity vectors, with the largest magnitude vectors pointed in the positive z direction (away from the front of the body). (Fig. 4.1).

Occasionally, the simulations would also produce velocity vectors at the tail fins. However, these vectors were generated less consistently, so pressure gradients were more indicative of hydrodynamic forces in this region of the body (Ferrón et al., 2020). As shown in Figure 4.1**,** each 3D solution visualization included a layer of colored pressure gradients across the model's body. While the specific values associated with each color varied for each simulation, warmer colors indicated higher pressure zones and colder colors indicated lower pressure zones. Pressure values were fairly consistent across the body of each model until the tail fins, and the dorsal tail fins specifically showed a pressure variation in each simulation. Generally, the dorsal tail fins produced higher pressure areas concentrated near the most distal part of the dorsal tail fin relative to the body. The specific size and placement of this region varied between models, but it was present in every model. Furthermore, the magnitude of the pressure differential between the ambient pressure around the body and the tail-generated high-

pressure zone varied between each model. The typical reconstruction model produced a minor pressure differential, along with two regions of slightly lower pressure relative to the ambient body pressure (Fig. 4.1 panel a). The extended model also produced a more minor pressure differential, but the differential was larger than the typical reconstruction model's differential. Both the fully folded and the folded and lowered model's pressure differentials were the largest relative to the other models, and both generated a small area of lower pressure relative to the body's ambient pressure towards the posterior region of the tail fin.

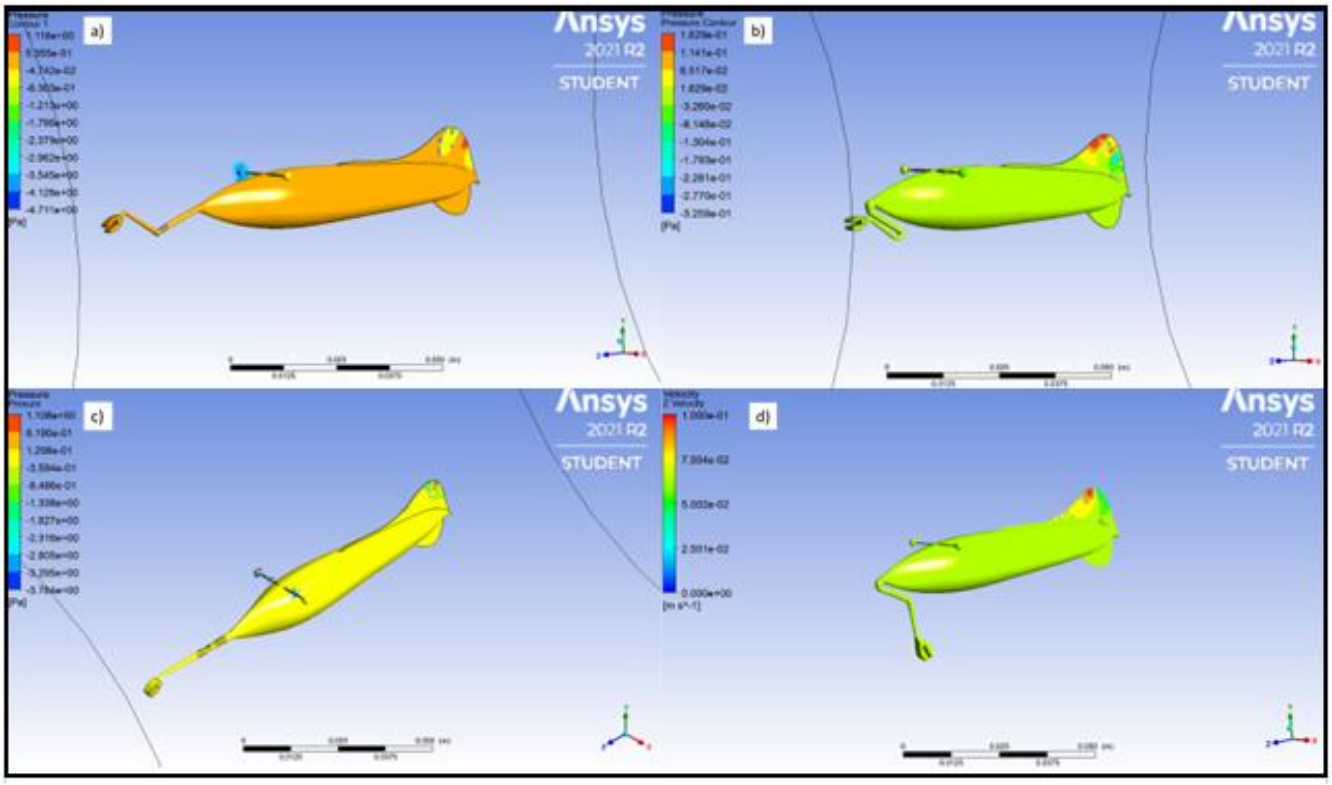

Figure 4.1: An overview of the visualizations of the 3D simulation results for each model, with velocity vectors and pressure gradients layered onto the models. a) The results for the typical reconstruction model. b) The results for the fully folded model. c) The results for the fully extended model. d) The results for the folded and lowered model. Based on size differences and viewing angle differences for each model, scale bar length in each panel is not consistent. However, each scale bar represents .050 m.

Typical Reconstruction Model in 3D

The typical reconstruction 3D model's simulation produced prominent velocity vectors clustered around the right eyeball on the model's eyebar, with significant magnitudes pointing in all directions in 3D space, suggesting that this region significantly disrupted the flow, generating forces in a variety of different directions (Dec, 2019). These vectors are clustered around one eye and not both eyes likely due to random errors. As mentioned previously, the resolution in the 3D

simulations are restricted in the ANSYS Student software, and the regions surrounding the body were not modeled in these 3D simulations (Ansys, 2021). Therefore, the program is inferring how a fluid around the body would interact with the body without actually modeling the fluid, which increases the error associated with these 3D models. Most likely, disruption around one eye instead of the other or both eyes randomly produced less error across several iterations, making this the preferred solution.

While these larger magnitude vectors are far more prominent than other vectors placed on the model, there are smaller vectors present along the eyebar itself and near the first joint of the proboscis. Vectors along the eyebar point mostly in the positive y direction and the positive z direction, indicating that the eyebar is producing some amount of drag and lift. The vectors clustered around the first joint along the proboscis lack a clear net direction, unlike the vectors along the eyebar. Instead, these vectors point in all directions, which suggests that this region of the proboscis is producing drag.

Differences in pressure zones along the dorsal tail fin were also fairly prominent in the typical reconstruction model (Ferrón et al, 2020). Two lower pressure regions relative to the body's ambient pressure and one higher pressure region relative to the body's ambient pressure were generated along this fin. The largest low-pressure region occurred along the centerline of the fin, where the fin is longest, and was outlined with smaller regions of even lower pressure shown in blue (Fig. 4.2). The second low pressure region occurred towards the posterior end of the tail in conjunction with the single high-pressure zone, which occurred slightly farther towards the anterior of the body and higher along the fin itself. Unlike the first low-pressure zone, the second low-pressure zone is not outline by smaller, even lower pressure zones, and the entire

zone itself was smaller. The high-pressure zone was very small as well, but still prominent. It occurred between the two low-pressure zones, clustered near the outer edge of the fin.

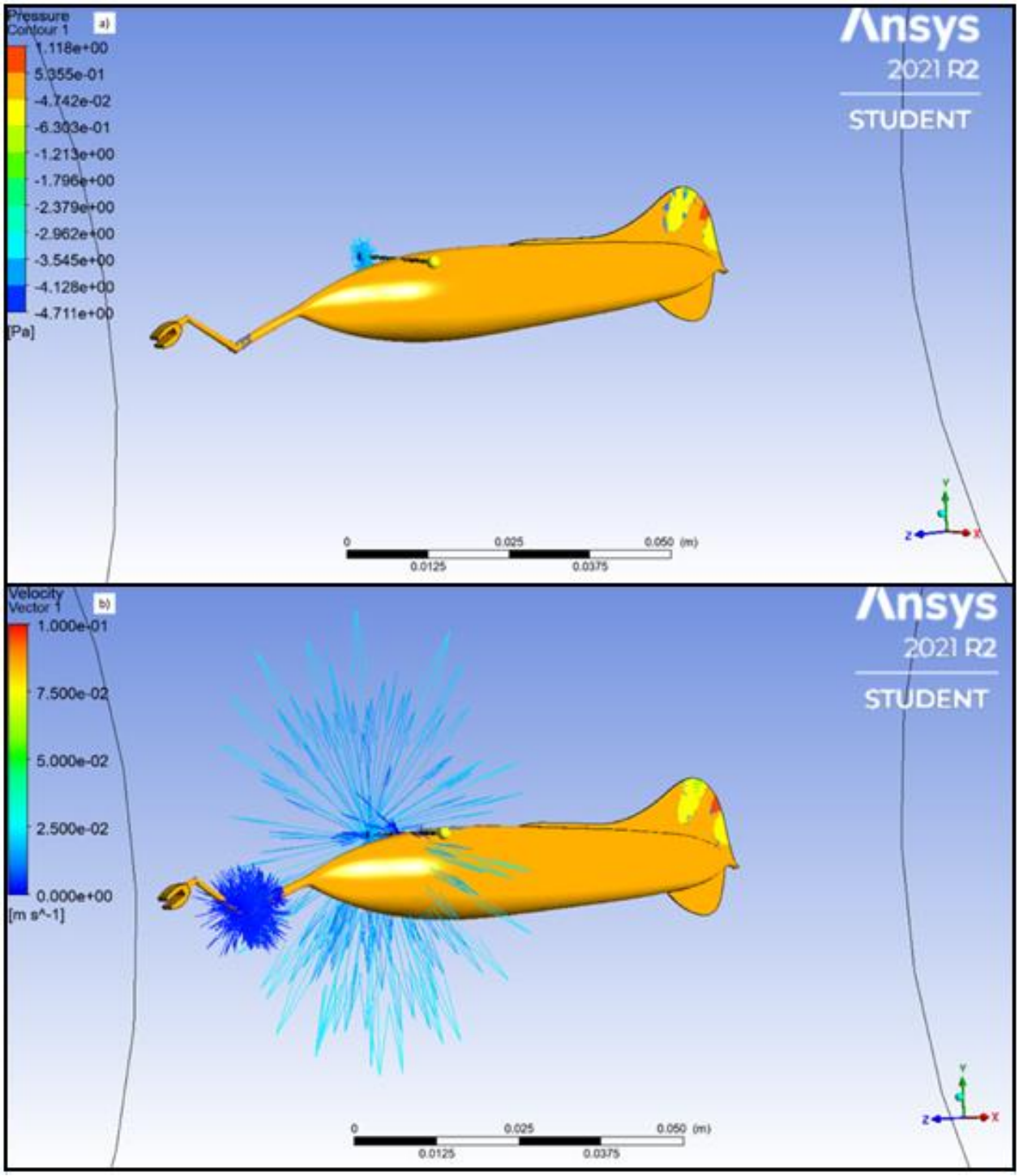

Figure 4.2: A more detailed view of the typical reconstruction model's 3D results. a) A broad view of the results with a focus on pressure gradients. b) A model with exaggerated vectors. Vectors in panel b are multiplied by a factor of 10.

Fully Folded Model in 3D

The fully folded model's simulations produced velocity vectors in different regions than the typical reconstruction model. Unlike the typical reconstruction model, the fully folded model's simulations did not produce any significant velocity vectors clustered around either of the model's eyes. Instead, the largest vectors were clustered near the posterior of the body near the region where the body meets the dorsal tail fin. These vectors originated at the point where the body begins to narrow, and uniformly pointed in the positive y direction, suggesting this region of the body is providing lift. There vectors appear to be slightly deflected to the posterior of the body, but not drastically so.

Like the typical reconstruction model, the fully folded model simulations also produced vectors along the eyebar, and they generally pointed in the positive y direction and the negative z direction, suggesting the eyebar was producing lift. The negative z component of these vectors could suggest that the eyebar was actually accelerating the flow, likely by manipulating pressure differentials near the eyebar. However, these vectors are relatively small, and the flow itself was not modeled in these 3D simulations, so these negative z components could simply be due to chance. The proboscis of the fully folded model also generated small vectors. These velocity vectors were mainly clustered near the feeding apparatus, but there were a handful of very small vectors present along the rest of the proboscis. All of these velocity vectors were very small relative to the other generated vectors, and they did not point in a coherent direction. Therefore, these vectors most likely indicate minor drag generation along the folded proboscis.

Pressure differentials generated by the fully folded model also differed from the typical reconstruction model. Specifically, the fully folded model generated more regions of high or low pressure relative to the ambient pressure around the body, even though these regions were still

constrained to the dorsal tail fin. High-pressure regions were concentrated near the leading edge of the dorsal tail fin around the distal edge of the fin and continued slightly into the center of the fin. A single high-pressure area was also located near the tip of the fin on the trailing edge of the fin, in the region where the fin edge quickly drops to the centerline of the body. Lower pressure regions were concentrated under this trailing edge high-pressure zone and extended nearly to the fin's attachment to the body. Generally, the high-pressure zones in the fully forward model were shifted anteriorly and expanded compared to the typical reconstruction model, while the low-pressure zones were shifted posteriorly.

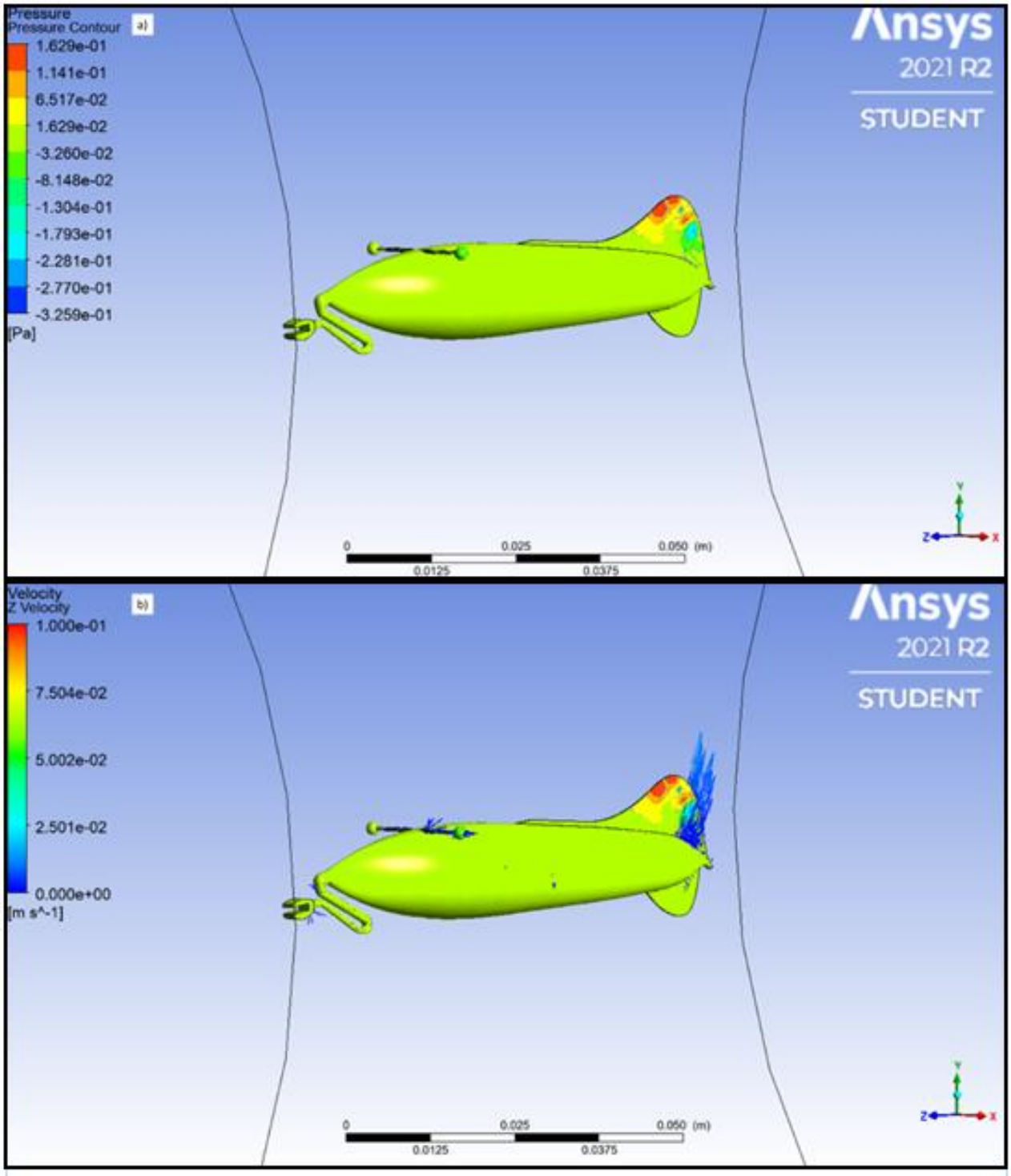

Figure 4.3: A more detailed view of the fully folded model's 3D results. a) A broad view of the results with a focus on pressure gradients. b) A model with exaggerated vectors. Vectors in panel b) are multiplied by a factor of 10.

Extended Proboscis Model in 3D

The extended proboscis model was somewhat of an outlier compared to the other models' 3D simulations. Like the other models, the extended proboscis model generated significant velocity vectors along the eyebar. However, these vectors point in multiple directions with no clear upward trend, suggesting that they were producing drag. The extended model also generated prominent velocity vectors around the buccal apparatus on the proboscis. These vectors pointed in various directions, but all of them had a negative z component pointing towards the posterior of the body. This suggests that the buccal apparatus could be increasing flow in this region by manipulating pressure zones around the proboscis itself. Furthermore, the extended model did not produce velocity vectors near the tail fin, unlike the fully folded model.

The pressure zones along the dorsal tail fin of the extended model were also smaller and differed less drastically relative to the ambient body pressure when compared to the other models. The low and high-pressure zones occurred in roughly the same locations along the dorsal tail fin as the pressure zones for the typical reconstruction model, but they were all smaller and more compact. Specifically, the low-pressure zones occurred near the tallest point of the dorsal tail fin and along the trailing edge of the dorsal tail fin as the fin begins to narrow. The high-pressure zone occurred in between the two low-pressure zones and bled into the posteriorly placed low-pressure zone. Each low-pressure zone had small areas of even lower pressure around its edges, but they did not form a complete or near-complete outline.

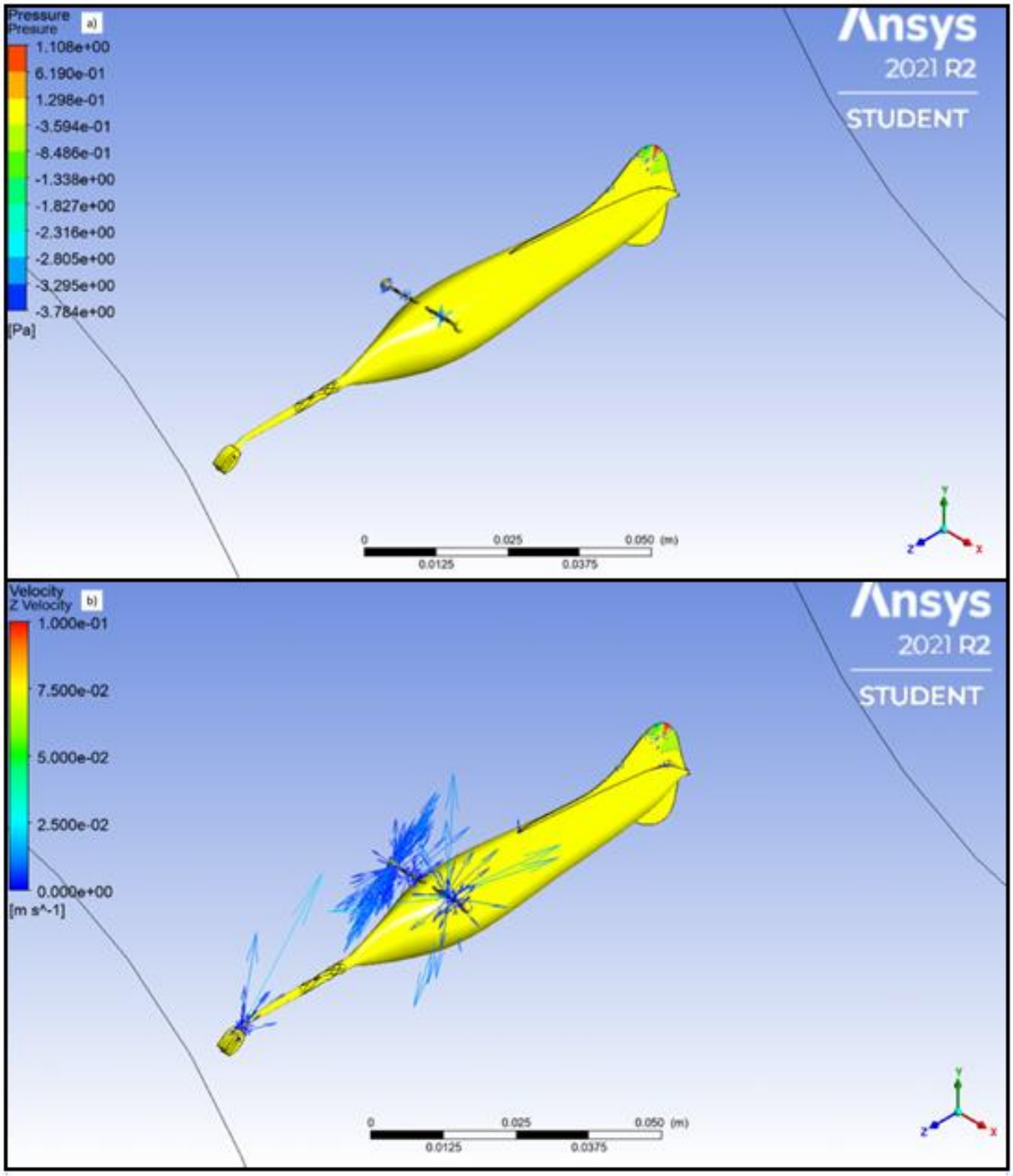

Figure 4.4: A more detailed view of the extended model's 3D results. a) A broad view of the results with a focus on pressure gradients. b) A model with exaggerated vectors. Vectors in panel b) are multiplied by a factor of 10.

Folded and Lowered Model in 3D

The folded and lowered model's simulation results were similar to the fully folded model's results, with a few key differences. Mainly, the vectors generated by the folded and lowered model are much smaller and less significant than in any of the other simulations, even when they are extended by a factor of 10 (Fig. 4.5). Like in the fully folded model, these vectors are clustered around the eyebar, the proboscis, and along the area where the dorsal tail fin meets the body. Vectors around the eyebar point in a variety of directions, with the majority of the vectors including a positive y component, suggesting lift is generated in this region. Vectors along the proboscis are very small and lack a directionality until the buccal apparatus. The handful of vectors generated by the buccal apparatus are larger relative to the other vectors along the body, and they incorporate a negative z component. However, it is difficult to interpret the vectors generated by the buccal apparatus because there are so few of them. Finally, the vectors generated by the attachment of the dorsal tail fin to the body are relatively uniform and follow the same upward trend in the positive y direction seen in the same region of the fully folded model's results. This suggests that this region of the body is producing lift.

The distribution of low and high-pressure zones along the dorsal tail fin of the folded and lowered model also mirrored the results of the fully folded model, with a few differences. Specifically, high-pressure regions were clustered near the leading edge of the dorsal tail fin and extended up until the farthest edge of the tail fin, where the highest-pressure zone was located. The low-pressure zone was located just downstream of the highest-pressure zone along the trailing edge of the dorsal tail fin. Unlike the fully folded model, the pressure zones in the folded and lowered model's results appear more gradational with smoother transitions from high pressure areas to low pressure areas without independent clusters of higher or lower pressure.

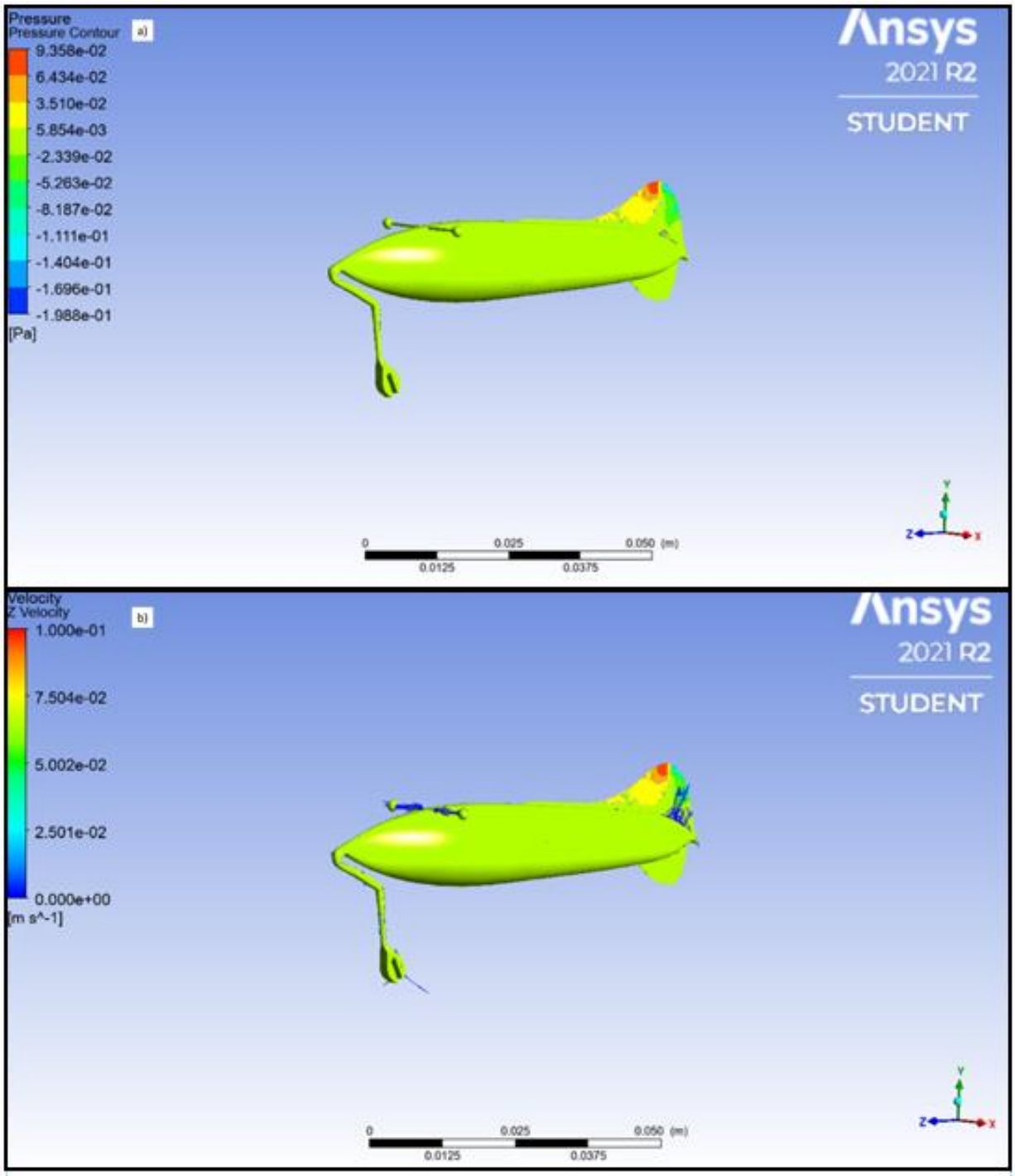

Figure 4.5: A more detailed view of the folded and lowered model's 3D results. a) A broad view of the results with a focus on pressure gradients. b) A model with exaggerated vectors. Vectors in panel b) are multiplied by a factor of 10.

An Overview of the 2D Results

Given the limitations of the ANSYS Student software, the 2D simulations for each model provided far more accurate results and more detailed data (Ansys, 2021 & Jiang et al., 2021). Each model produced two sets of 2D results, one from a zy-plane view looking at a side profile of the body and one from a xy-plane view looking at a top-down view of the body. Both sets of results model the flow around the body instead of the forces acting on the body itself (Jiang et al., 2021). The results of these simulations are visualized as a layer of pressure contours, which reveal regions of low and high pressure around the body, and velocity streamlines, which detail how individual particles in the flow interact with the body to produce these pressure gradients (Jiang et al., 2021). Collectively, they give insight into the hydrodynamic forces, like lift and drag, that are acting on the body, even though the forces on the body itself are not simulated or recorded in 2D, and their resolution allows for more robust comparisons between models (Jiang et al., 2021).

Typical Reconstruction Model in 2D

The typical model generated several distinct pressure zones in the flow around the body in a side profile view. Specifically, the typical model generated a high-pressure zone near the leading edge of the buccal apparatus and on the dorsal section of the body where the proboscis meets the body, just upstream of the eyebar. The high-pressure zone generated by the buccal apparatus was paired with a significant low-pressure zone downstream and underneath the proboscis while the high-pressure zone near the eyebar was not paired with a low-pressure zone. The body itself also generated a low-pressure zone underneath the model, near the ventral midpoint of the body. Finally, the tail fins generated a large elliptical low-pressure zone relative to the ambient flow in this region of the body.

The typical model from a side profile view's velocity streamlines matched the pressure contours quite closely. Higher velocity regions occurred on the ventral side of the proboscis downstream of the buccal apparatus, along the ventral side of the model, and downstream of the ventral and dorsal tail fins. These higher velocity regions coincided with the low-pressure regions seen in the pressure contours. Low-velocity regions were clustered around the buccal apparatus, the dorsal side of the model, and in the boundary layer of the model. Except for the low-velocity generated in the boundary layer, other low-velocity zones coincided with the high-pressure regions of the model. The model also generated a wake with no velocity downstream of the buccal apparatus and the tail fins.

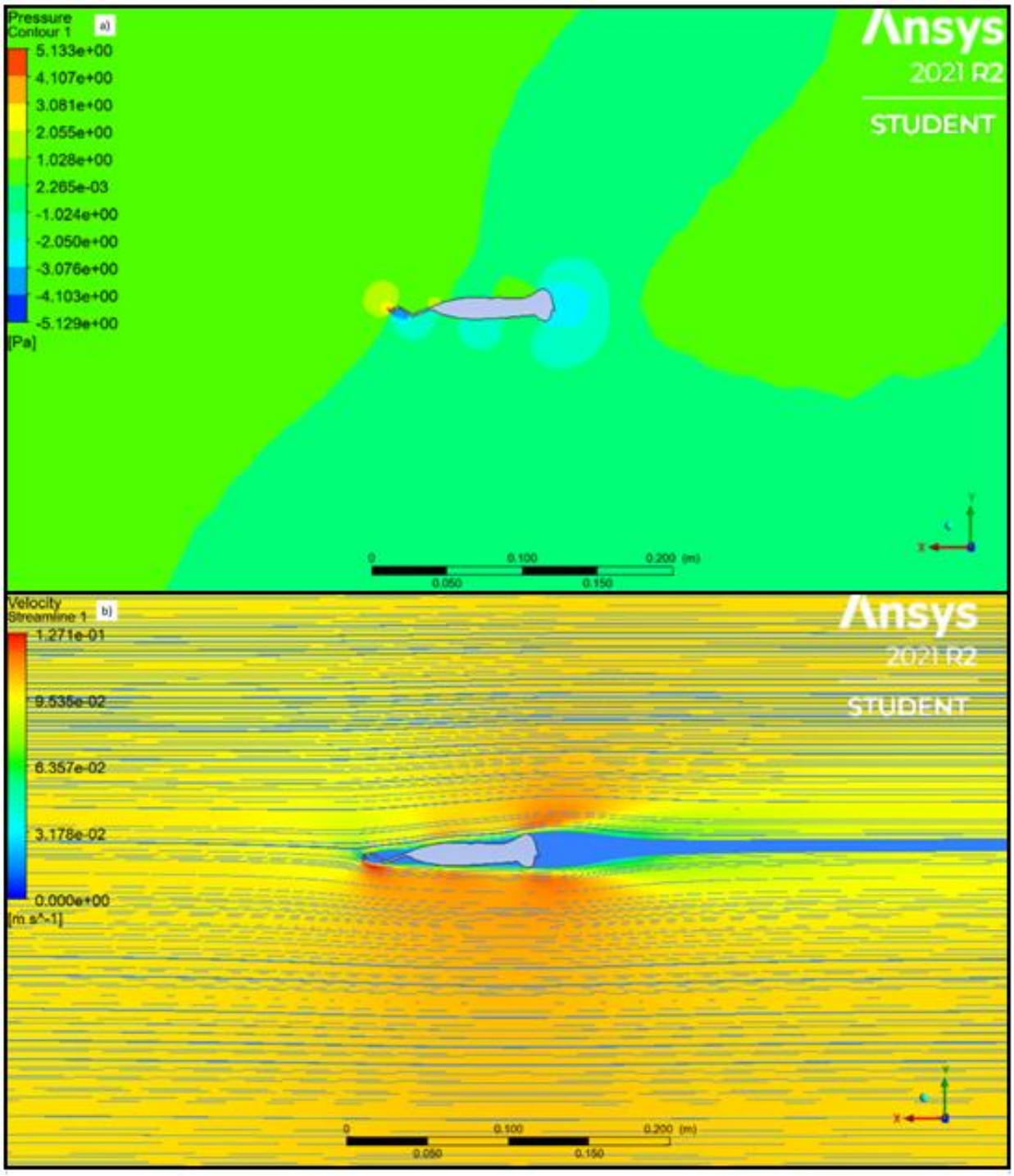

Figure 4.6: A more detailed view of the typical reconstruction model's 2D side profile results. a) Pressure contours in the flow field. b) Particle velocities around the model's body.

The top-down view of the typical reconstruction model provided more information about the effect of the eyebar on the flow. Specifically, the eyebar generated a large low-pressure zone

that was more significant near the body in an ellipse continuing to the tail fins, and less significant as you move farther from the body. Upstream of the eyebar, the buccal apparatus of the proboscis generated a high-pressure cone pointing forward from the model compared to the ambient flow. This cone of high-pressure was most intense where the buccal apparatus met the flow and in a region from the midway point of the proboscis to the outer edge of the eyebar downstream.

Similar to the side profile results, the velocity streamlines mirror the pressure gradients in the top-down profile results for the typical reconstruction model. Specifically, the eyebar generates a clear high-velocity region to the left and the right of the body along with a significant wake with no velocity, which coincides with the low-pressure regions observed in this region. The flow also appears to slow slightly around the buccal apparatus and the proboscis, which coincides with the observed high-pressure region in this area.

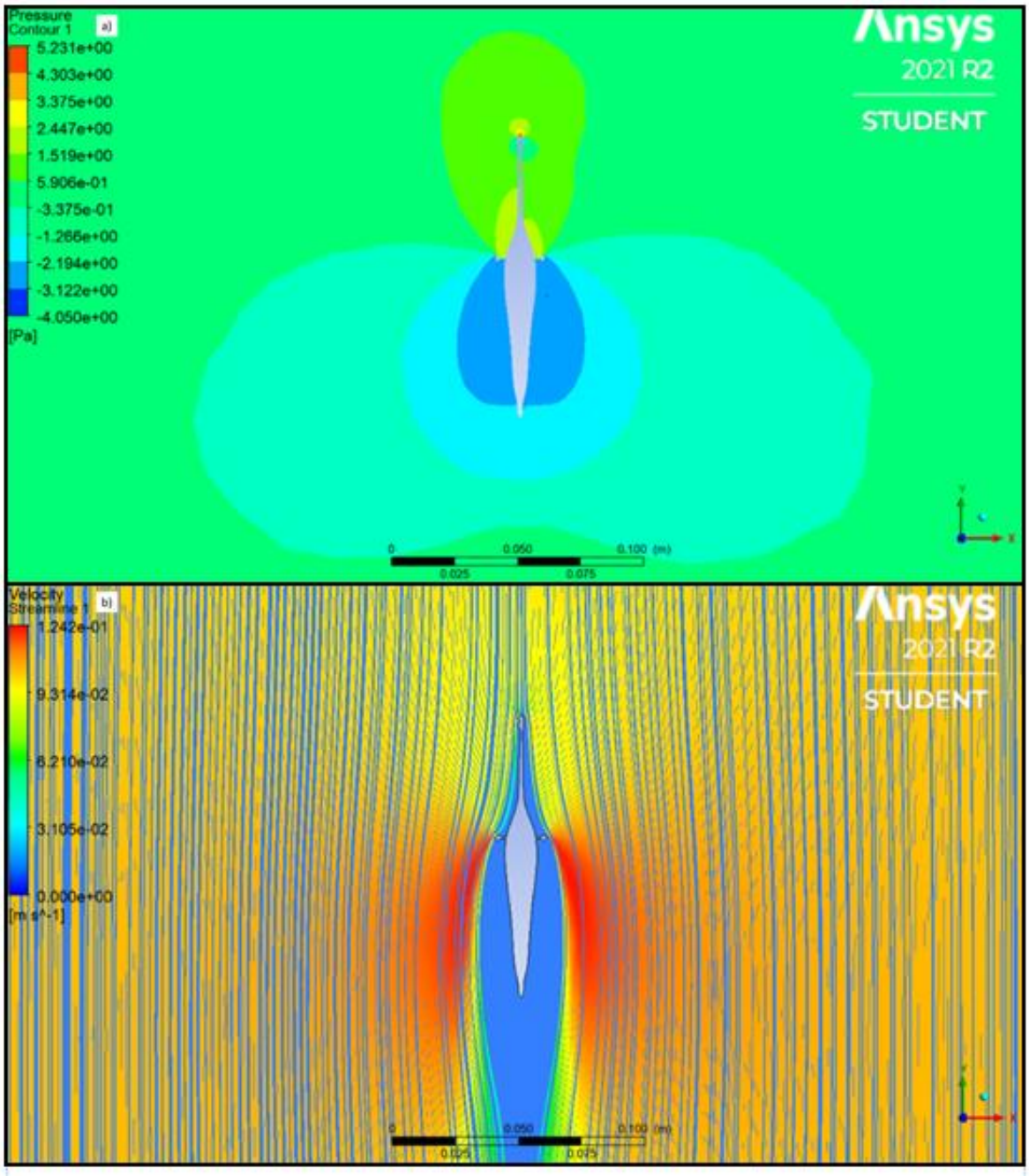

Figure 4.7: A more detailed view of the typical reconstruction model's 2D top-down profile results. a) Pressure contours in the flow field. b) Particle velocities around the model's body.

Fully Folded Model in 2D

The fully folded model's 2D results were more complicated than the 2D results generated by the typical reconstruction model. In a side profile view of the side of the body, the fully

folded model generated a large high-pressure zone along the dorsal edge of the buccal apparatus and the folded proboscis, generating a bloom of high-pressure to the anterior of the model, mostly above the model's centerline. There were also high-pressure zones present along the body just before the dorsal tail fin, and downstream of the body to the posterior of the model. Low-pressure zones were concentrated on the ventral side of the model. The most significant low-pressure zone occurred underneath the folded proboscis and was paired with the dorsal high-pressure zone. A second low-pressure zone occurred formed an ellipse around both the ventral and dorsal tail fins, extending outwards from the posterior of the body.

As in the typical reconstruction model's results, the velocity streamlines mirrored the pressure contours for the fully folded model's simulations. Specifically, the significant high-pressure zone formed by the buccal apparatus and the folded proboscis was reflected in a low-velocity zone in this region. The low velocity in this region to the anterior of the body appears to deflect particles towards the body, slowing their velocity and contributing to the high-pressure bloom to the anterior of the body and the high-pressure region along the dorsal side of the body. This low-velocity region above the proboscis coincides with a high-velocity region underneath the proboscis. This high-velocity region coincides with the low-pressure region observed in this area. Like in the typical reconstruction model's results, the tail fins also generate mirrored regions of higher velocity, which coincide with the low-pressure regions observed in the same area. Finally, the proboscis and body itself generated a wake with no velocity, similar to the typical reconstruction model.

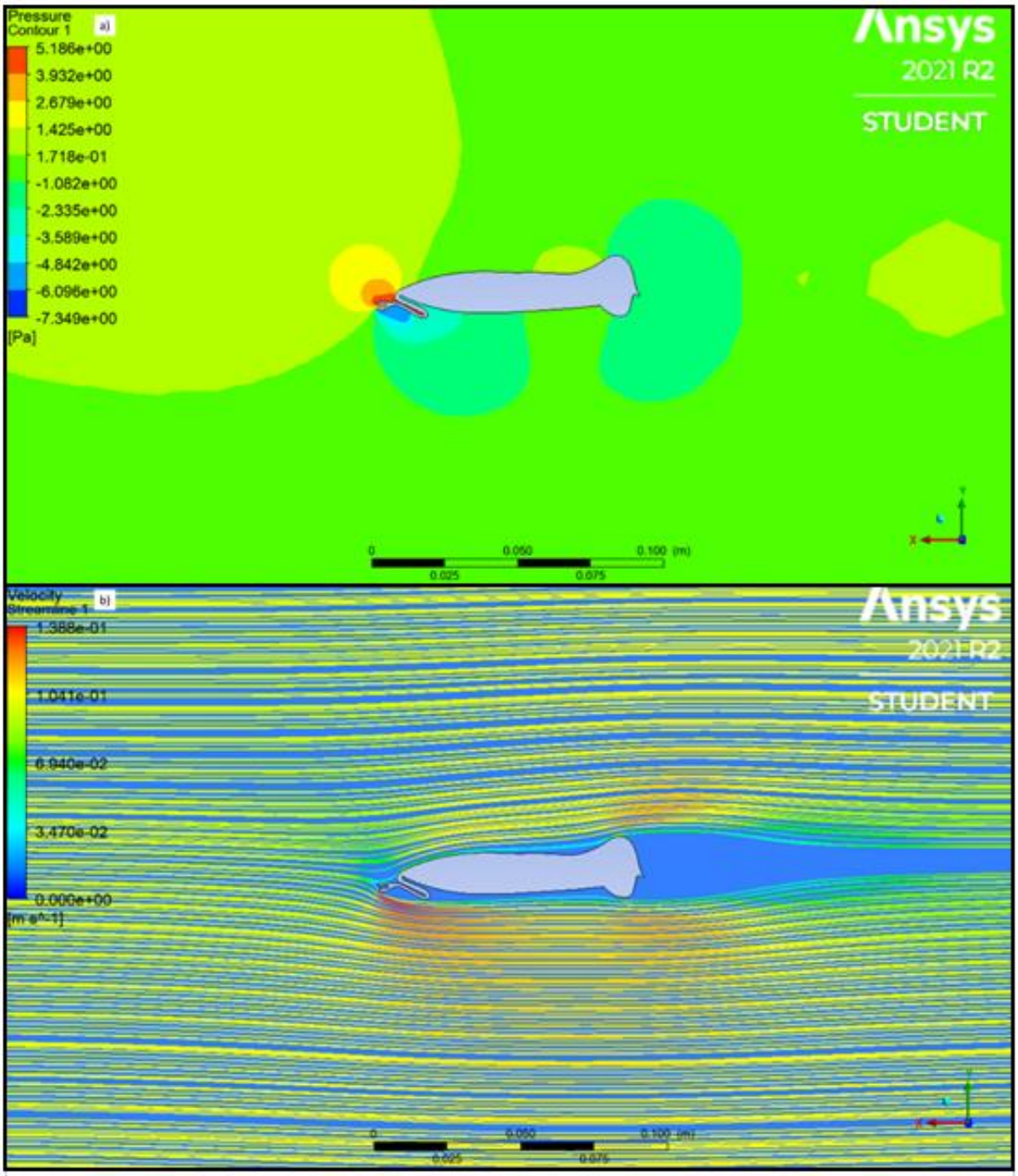

Figure 4.8: A more detailed view of the fully folded model's 2D side profile results. a) Pressure contours in the flow field. b) Particle velocities around the model's body.

The fully folded model's top-down profile results were almost identical to the typical reconstruction model's top-down profile results, with a few minor differences. Mainly, the shorter proboscis from a top-down view generated more intense high-pressure regions near the

buccal apparatus and the leading edge of the eyebar relative to the typical reconstruction model's results. Otherwise, the eyebar in the fully folded model generated the same low-pressure zone downstream of the eyebar that dissipated into the ambient pressure as you move away from the body. The velocity streamlines reflect this, with the eyebars generating significant high-velocity regions on either side of the body. The velocity streamlines also reflect the high-pressure zones near the proboscis with low-velocity regions in the same area, which are likely generated as the proboscis and the buccal apparatus disrupt the flow.

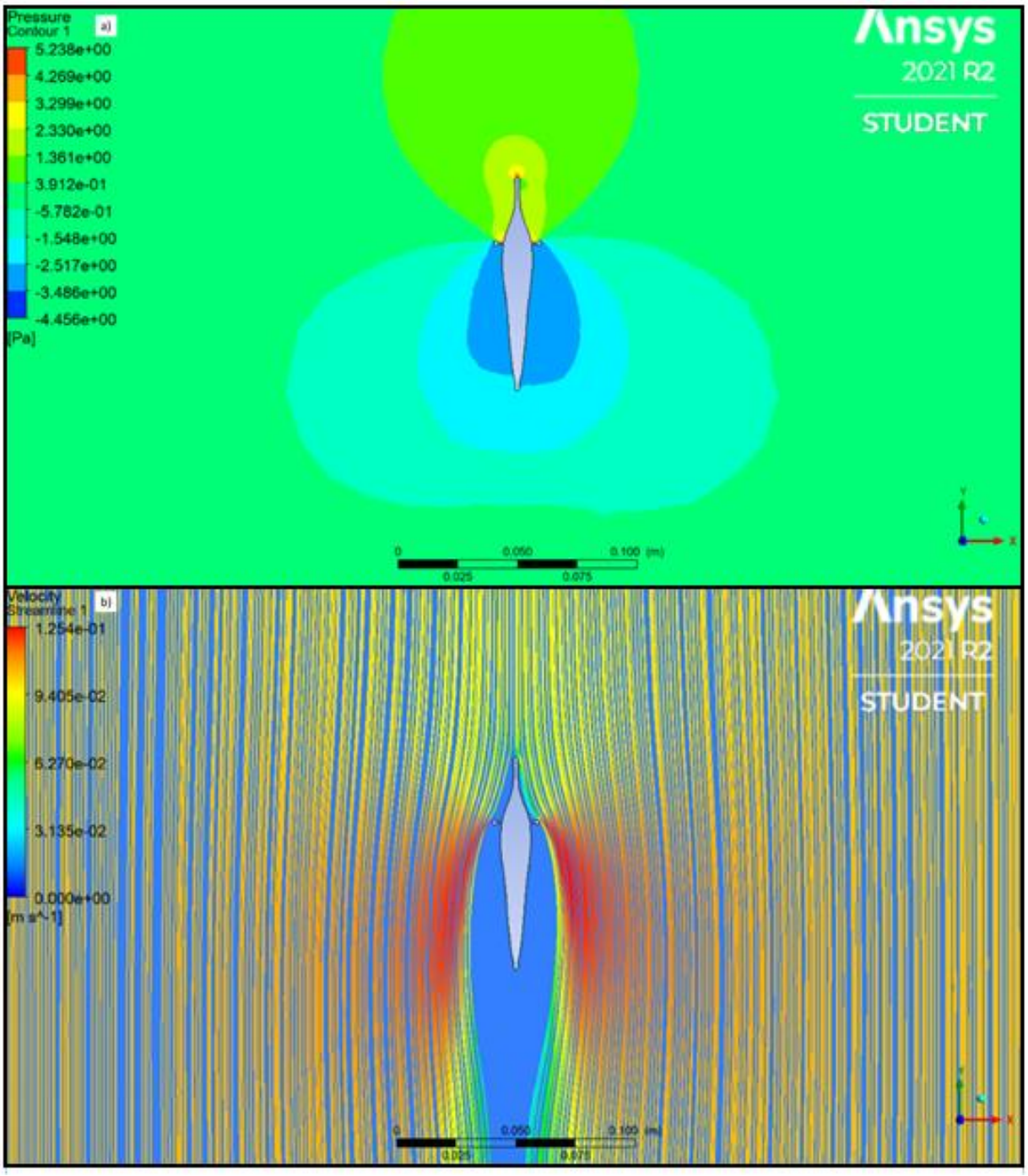

Figure 4.9: A more detailed view of the fully folded model's 2D top-down profile results. a) Pressure contours in the flow field. b) Particle velocities around the model's body.

Extended Model in 2D

The extended model also followed trends seen in the previous models, with a handful of notable differences. Specifically, the high-pressure region generated by the buccal apparatus had a higher intensity at the point where the flow meets the apparatus, but this more intense region was very restricted compared to the overall high-pressure bloom. There was also a second region of higher pressure within the high-pressure bloom, located where the proboscis meets the body. Like in the other models, the high-pressure region was paired with a low-pressure region extending underneath the buccal apparatus along the length of the proboscis. Given that the proboscis is held in a position that extends it further into the flow, this low-pressure region underneath the proboscis was larger than in the other models. Furthermore, this low-pressure region connected with a semi-circular low-pressure region extending below the ventral side of the model. This larger low-pressure bloom also connected with the low-pressure zone generated by the tail fins to the posterior of the body.

As in the other models, the velocity streamlines supported the pressure contours. The buccal apparatus and the proboscis generated low-velocity regions to the anterior of the body, which coincide with the high-pressure regions seen in the flow field. Similarly, this low-velocity region was paired with a high-velocity region underneath the buccal apparatus and the proboscis, which extended along the entire ventral side of the model and coincided with the large low-pressure zone observed in the results. As in the other models, the spade-shaped tail generated two mirrored high-velocity zones that mirrored the low-pressure bloom observed in this region downstream of the body. The model itself also generated a wake with no velocity, but the shape of this wake differed from the other models. Specifically, the buccal apparatus itself generated a large wake that correlated with the intense low-pressure underneath the proboscis. The wake generated downstream of the model, however, was consistent with the other models.

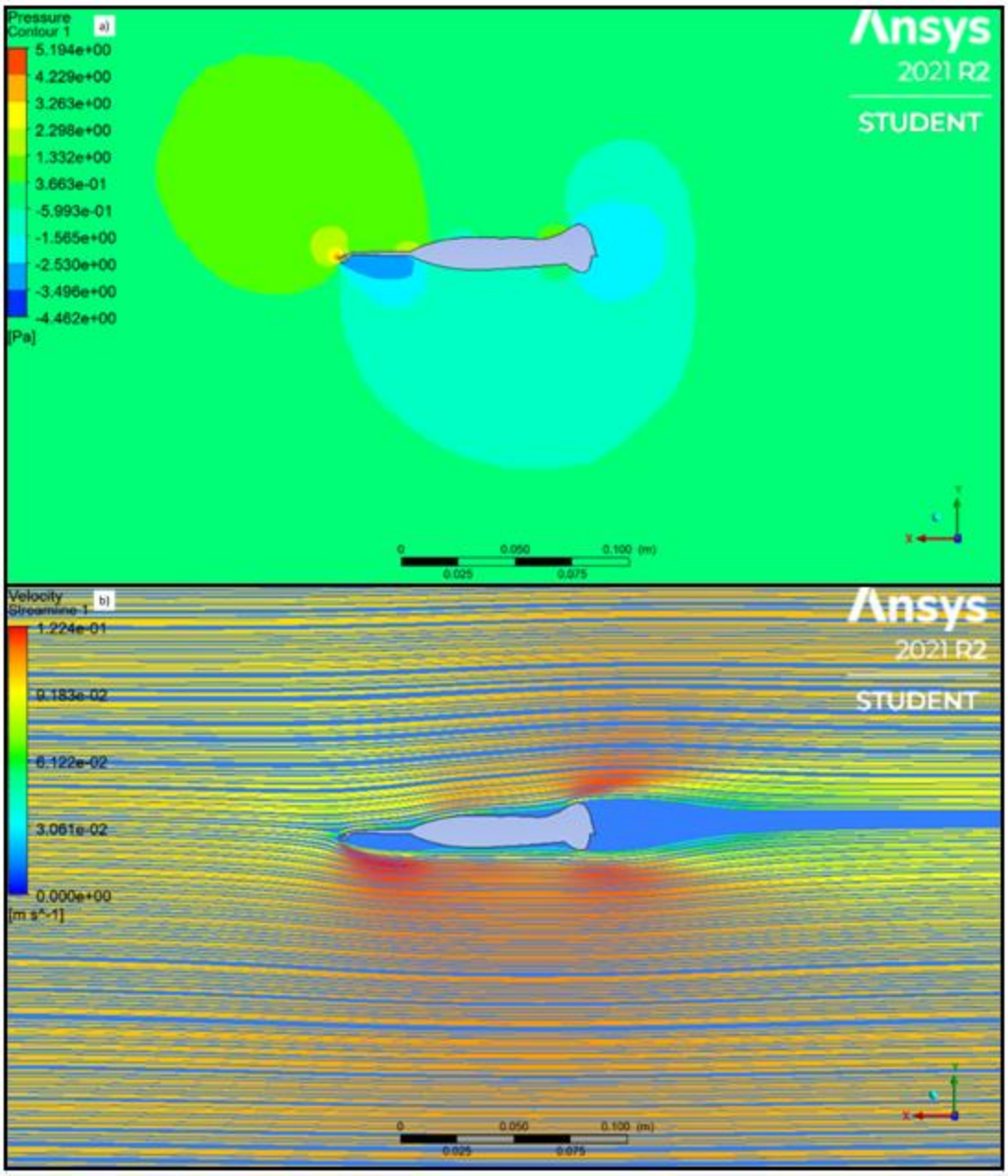

Figure 4.10: A more detailed view of the extended model's 2D side profile results. a) Pressure contours in the flow field. b) Particle velocities around the model's body.

In a top-down view, the extended model was mostly consistent with the other models. Like in the other models' simulations, the buccal apparatus and the proboscis generated a high-pressure region, with a more intense high-pressure region occurring near the leading edge of the buccal apparatus. The eyebar also generated the same low-pressure zone around the body, with a

more intense low-pressure clustered around the body itself, and less intense regions radiating out from the body. These low-pressure regions on both sides of the body extended farther away from the body in all directions than they did in other simulations.

These low-pressure regions were paired with high-velocity regions generated as the eyebar deflected flow around the body. Similarly, the high-pressure regions were paired with low-velocity regions generated as the proboscis and the buccal apparatus met the flow and disrupted the flow. Both the proboscis and the eyebar generated a wake with no velocity downstream of these features.

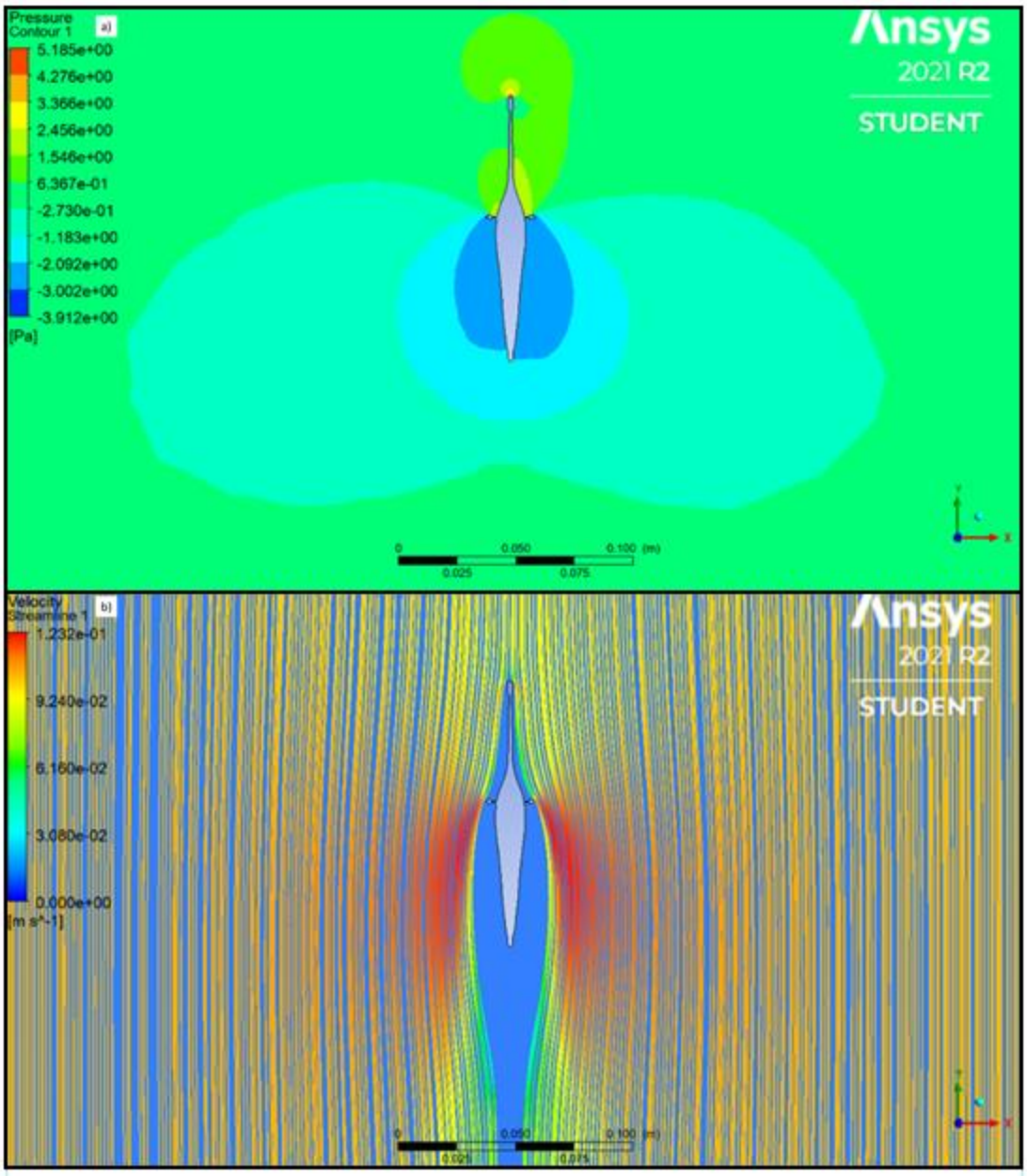

Figure 4.11: A more detailed view of the extended model's 2D top-down profile results. a) Pressure contours in the flow field. b) Particle velocities around the model's body.

Folded and Lowered Model in 2D

Given that the folded and lowered model's proboscis extends significantly farther to the posterior of the body compared to the other models, the folded and lowered model's 2D results were outliers compared to the other models. However, several trends were still present in the

folded and lowered model's results. Specifically, the leading edge of the proboscis generated a large high-pressure zone to the anterior of the model in a side profile. This high-pressure zone was paired with a large low-pressure zone that extended all the way around the body from the edge of the buccal apparatus to the area where the proboscis meets the body on the dorsal side of the model. This low-pressure zone was most intense along the ventral side of the model downstream of the lowered proboscis and around the tail fins. Most likely, this is the result of the low-pressure zones observed underneath the bodies of the other models and the low-pressure zones seen around the tails of the other models merging. Furthermore, the overall low-pressure zone was less pronounced on the dorsal side of the body and generally became less intense as you move farther from the body. Interestingly, the low-pressure region does not dissipate entirely in this simulation, instead forming a shape that almost represents a shockwave in the flow field extending from where the model first interacts with the flow on the anterior side of the model.

The velocity streamlines complement these pressure contours. Specifically, the lowered proboscis significantly disrupts the flow, generating a low-velocity, high-pressure region upstream of the lowered proboscis. Past the buccal apparatus and above the dorsal attachment point of the proboscis to the body, the flow velocity increases significantly, coinciding with the low-pressure region seen surrounding the body downstream from the proboscis. The boundary layer velocity in this region appears to be much faster relative to the ambient flow than the observed boundary layers in the other models' simulations. The no velocity wake is also larger in this simulation, which makes sense considering the lowered proboscis significantly disrupts the flow in this region.

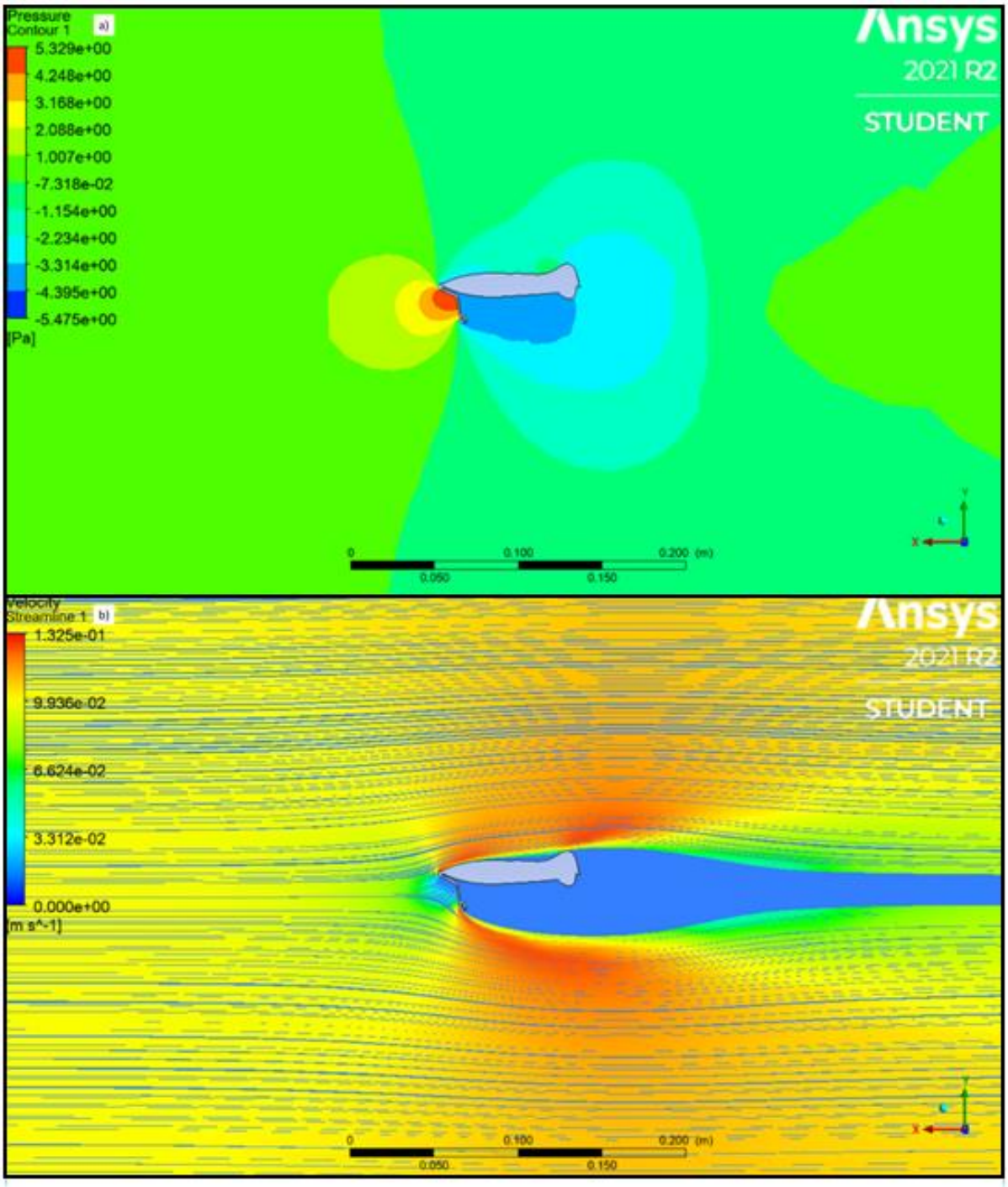

Figure 4.12: A more detailed view of the folded and lowered model's 2D side profile results. a) Pressure contours in the flow field. b) Particle velocities around the model's body.

While the side profile view of the folded and lowered model differs significantly from the other models, the top-down view is fairly consistent with the other models. As in the other

models, the eyebar generates a significant low-pressure zone around the body that is most intense in the region extending from the eyebar to the posterior of the body. This low-pressure zone also dissipates into the ambient flow pressure as you move away from the body. The folded proboscis also generates a high-pressure region at the anterior of the body, extending to the anterior edge of the eyebar, like in the other models. This high-pressure region extends farther forward from the anterior compared to the other models, but it forms the same basic shape with the same distribution of higher-pressure areas within the entire high-pressure region.

Similarly, the eyebar deflects and accelerates the flow around the body, creating high-velocity regions and wake regions that correlate with the low-pressure zones observed in the pressure contours. The folded proboscis also generates lower flow regions around the anterior of the body as the body meets the flow, which correlate with the high-pressure region observed in the pressure contours. While the apparent length of the proboscis is shorter in this view for the folded and lowered model relative to the other three models, these velocity regions and pressure regions do not appear to be significantly different compared to the other models in a top-down view.

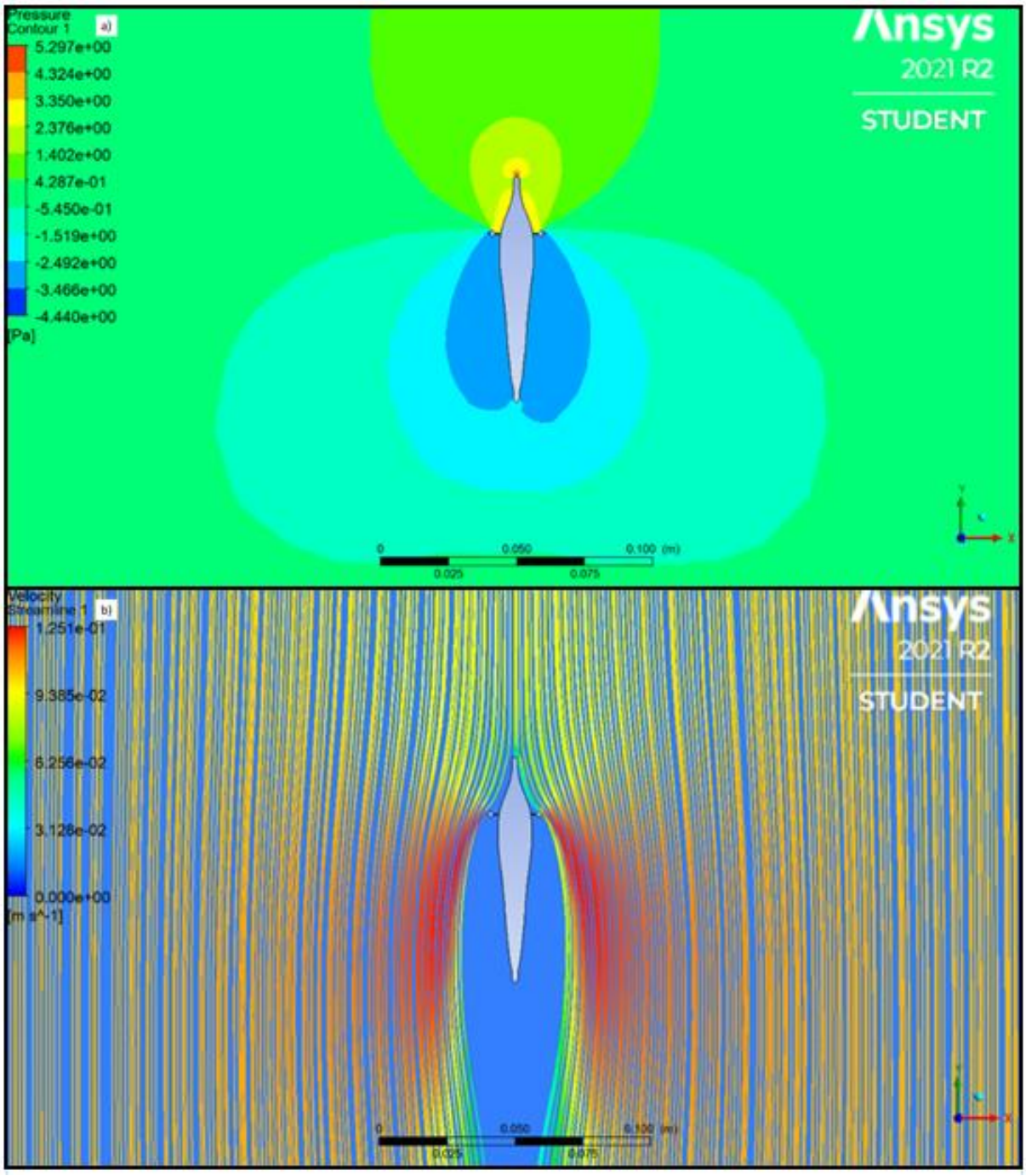

Figure 4.13: A more detailed view of the folded and lowered model's 2D top-down profile results. a) Pressure contours in the flow field. b) Particle velocities around the model's body.

Chapter 5: Discussion

3D Trends Amongst the Models

Fin Pressures

While each model produced different results during simulations, there were notable trends that were mostly consistent among the 3D models. Perhaps most obviously, each 3D model only produced pressure differentials along the dorsal tail fin. While fish employ a variety of techniques to propel themselves, many fish are capable of sculling, or propelling themselves forward by manipulating zones of low and high pressure generated as they move their tail fins back and forth (Webb, 1977; Webb, 1984; Lauder, 1989). These motions change the velocity of the water moving across the surface of the fin, which creates regions of lower or higher pressure relative to the body or the ambient flow following Bernoulli's Principle (Lee et al., 2011). Generally, propulsion via sculling is more efficient and less energy intensive than other forms of swimming (Webb, 1984). Since the Tully Monster's dorsal tail fin generated high- and low-pressure zones relative to the rest of the body in all of the 3D simulations, it is likely that this tail fin would have been capable of generating the pressure differentials required for sustained sculling.

Alternatively, the Tully Monster could have relied on inertial swimming using its dorsal tail fins. The Tully Monster could have, for example, used its tail fin to physically push the water at an angle to propel the whole body forward as the tail undulates (Webb, 1984). This angle would be more drastic relative to the body's centerline compared to the angle the tail fins would have been held at to generate pressure differentials for sculling (Webb, 1977; Webb, 1984). This larger angle would produce more drag as the Tully Monster moves forward, making this swimming motion more energy-intensive than sculling (Webb, 1984). Regardless, all fish that

scull must start moving by inertial swimming before the flow around the body is fast enough to generate pressure differentials, so all fish that rely on sculling are also capable of inertial swimming (Webb, 1984). Therefore, it is very likely that the Tully Monster was also capable of inertial swimming.

The Tully Monster's fins could have also trapped a bubble of water between folds in its fin, and then undulating these fins in a ripple motion to evenly push against the water above and below the body. Several modern fish groups are capable of this, and some fish groups in tropical settings, like the filefish, rely on this undulatory motion as their primary form of forward and vertical propulsion (Ballard and Rakocinski, 2012; George, 2020). However, fish like the filefish that rely on undulatory fin motions tend to have straight, mostly symmetrical dorsal and ventral tail fins, and this swimming motion requires musculature that can precisely manipulate individual fin-rays (George, 2020). Preserved Tully Monster specimens lack the detail required to determine whether this undulatory motion is feasible (McCoy et al., 2016), but it certainly cannot be ruled-out entirely. Furthermore, the Tully Monster's fins are spade-shaped instead of straight, and the dorsal tail fin is positioned slightly posteriorly relative to the ventral tail fin. Collectively, these characteristics would likely produce uneven forces if the fins were undulated, making this propulsion method less likely.

Eyebar vectors

While the magnitude of the velocity vectors generated by the eyes and the eyebar varied between each 3D model, each model produced velocity vectors around the eyebar. Furthermore, these vectors appeared to have a positive y-axis component in all of the solutions, suggesting that this region was providing an upward force. This could indicate that the eyebar produces small amounts of hydrodynamic lift in a flow, which could help stabilize that Tully Monster. Fish

typically have several key stabilizing fins for roll, pitch, and yaw control (Webb, 1984; Lauder, 1989; Drucker and Lauder, 2004). The pectoral fins, for example, often stabilize the roll and the pitch of a fish's body upstream of a fish's center of gravity (Webb, 1977; Webb, 1984). The Tully Monster, however, lacks traditional stabilizing fins and lacks fins anterior of the body's center of gravity entirely. Therefore, it is likely that the vectors generated by the eyebar indicate that this was a stability feature that likely stabilized the body passively. Preserved eyebars in Tully Monster specimens are routinely preserved in the same, horizontal orientation relative to the body, suggesting that they were likely rigid structures in life and likely could not be manipulated to control flow (Johnson and Richardson, 1969).

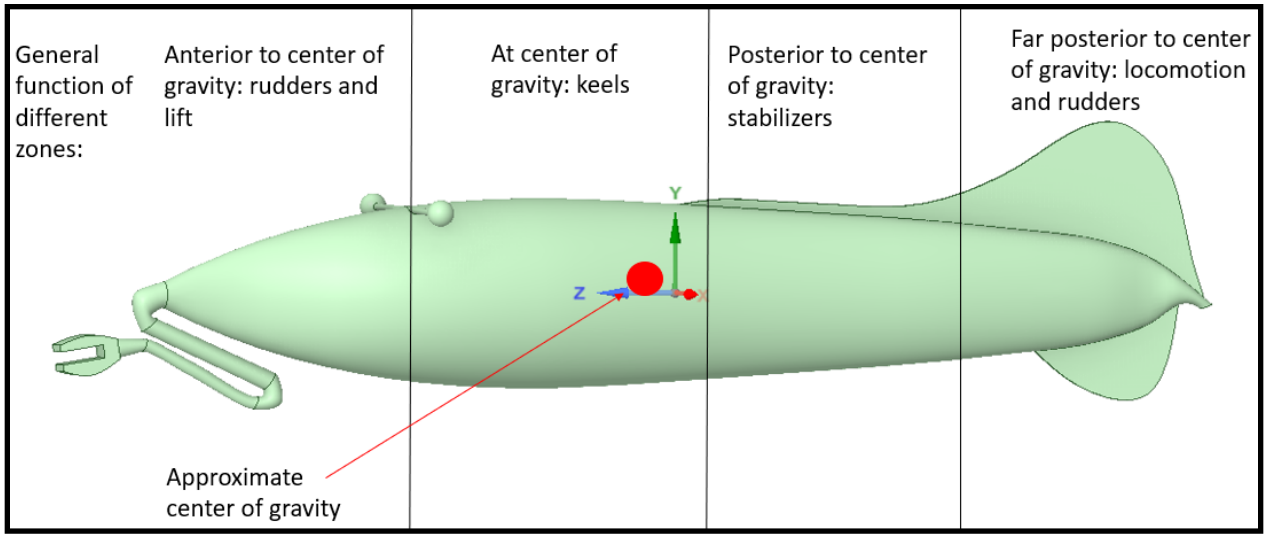

Figure 5.1: A diagram detailing the general function of different features in different regions of a fish body plan relative to the body's center of gravity superimposed over the fully folded model.

It is also possible that the velocity vectors generated by the eyebar and the eyes themselves could be indicative of vortices generated by these features. Features that extend from a mostly streamlined body would be able to generate vortices, and other CFD simulations studying several agnathan groups with bony shields have documented vortices generated by the

most distal edges of the headshields of these armored fish (Dec, 2019; Ferrón et al., 2021). If the Tully Monster's eyebars are generating vortices, these vortices may re-attach to the body farther downstream and generate the pressure differentials observed along the dorsal tail fins of the models. This, however, remains unclear given that the flow could not be modeled in 3D within the limitations of the ANSYS Student software suite (Ansys, 2021).

2D Trends Amongst the Models

As mentioned previously, the 2D results of this study are more robust than the 3D results (Ansys, 2021 & Jiang, 2021), and they provide a clearer picture of the hydrodynamic effects of various features and the overall hydrodynamic characteristics of the Tully Monster. The 2D models exposed several key differences amongst the models, but there were also several interesting trends. Namely, the side profiles of each model generate a distinct pressure differential between the dorsal and ventral sides of the model. Specifically, each model generated lower pressure underneath the ventral side of the model and relatively higher pressure above the dorsal side of the model. The high-pressure zone above the dorsal side of the models was occasionally a lower pressure than the ambient flow, but still higher-pressure relative to the underside of the body. This pressure differential could be significant since these differentials are indicative of negative lift. The high-pressure, less interrupted flow above the body could push the body downward in the water column while the low-pressure zone below the body pulls the body downward, like an upside-down airfoil. Since these differentials appeared in each simulation, it is possible that the Tully Monster's body plan generates forces that favor descent in the water column while the Tully Monster is moving or when the Tully Monster is stationary in a flow.

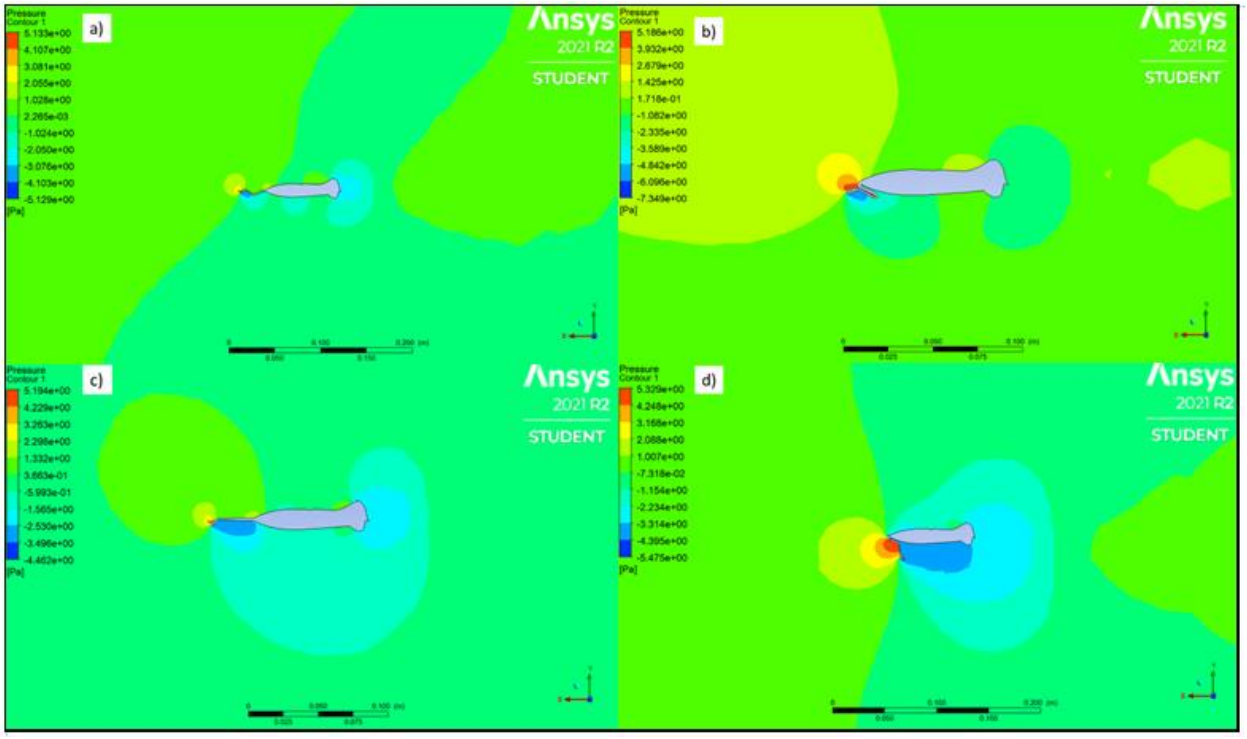

Figure 5.2: The 2D side profile results for each model, compiled for comparison. a) The typical reconstruction model b) The fully folded model c) The extended model d) The folded and lowered model.

Along with the consistent dorsal-ventral pressure zones, each model produced remarkably similar results in the top-down simulations. While each model had a slightly different apparent proboscis length in this view, each proboscis produced the same hydrodynamic effects. In each case, the proboscis slowed the flow, generating high pressure zones in a cone extending slightly beyond the proboscis to the anterior of the body that ended at the start of the eyebar to the posterior of the proboscis. The pressure intensities and the overall size of the cone varied slightly with proboscis length, but the overall trend was consistent. Furthermore, the eyebar generated a distinct low-pressure bubble downstream from the eyebar around most of the Tully Monster's body, and created a clear, large area of no-velocity wake.

This large wake and low-pressure zone suggest that the eyebar's hydrodynamic effects likely interact with the tail fins during swimming to maintain consistent pressure differentials in this region of the body. However, it is unclear how large of a role these eyebar-generated forces play without more robust 3D modeling. It is quite likely that the eyebar is generating symmetrical vortices trailing behind each eye in the flow, and these 3D vortices would provide a physical barrier to maintain a zero-velocity wake and a low-pressure zone around the body (Dec, 2019). Without more robust 3D models, however, it is unclear whether this is truly the case and how large these vortices are, if they truly exist. A range of vortex sizes could determine whether the eyebar only impacts the dorsal tail fin or whether these potential vortices are large enough to impact flow around both tail fins, which could have implications for the Tully Monster's swimming abilities.

Regardless, the symmetrical low-pressure bubble generated by the eyebar to the left and the right of the body likely helps stabilize the Tully Monster while swimming on in a flow, whether it is generated by vortices or not. Since this large, low-pressure zone is even on both sides of the body, higher pressure water outside of the bubble in the ambient flow would push against the body evenly from the left and the right. Any uneven forces would likely induce roll instability. However, it remains unclear how important or how strong this stabilizing force is without more detailed 3D simulations. It could be that the low-pressure zones only affect the dorsal tail fin, leaving the ventral tail fin exposed to potential pressure differences in other planes. Since the tail fins form a large, flat oval shape extending above and below the Tully Monster's body, these regions are more prone to being affected by the flow and inducing roll instability by uneven forces pushing against the left and right of these fins. At the very least, it is

clear that the eyebar partially protects the dorsal tail fin from destabilizing forces, and it is possible the eyebar fully protects the dorsal tail fin along with part or all of the ventral tail fin.

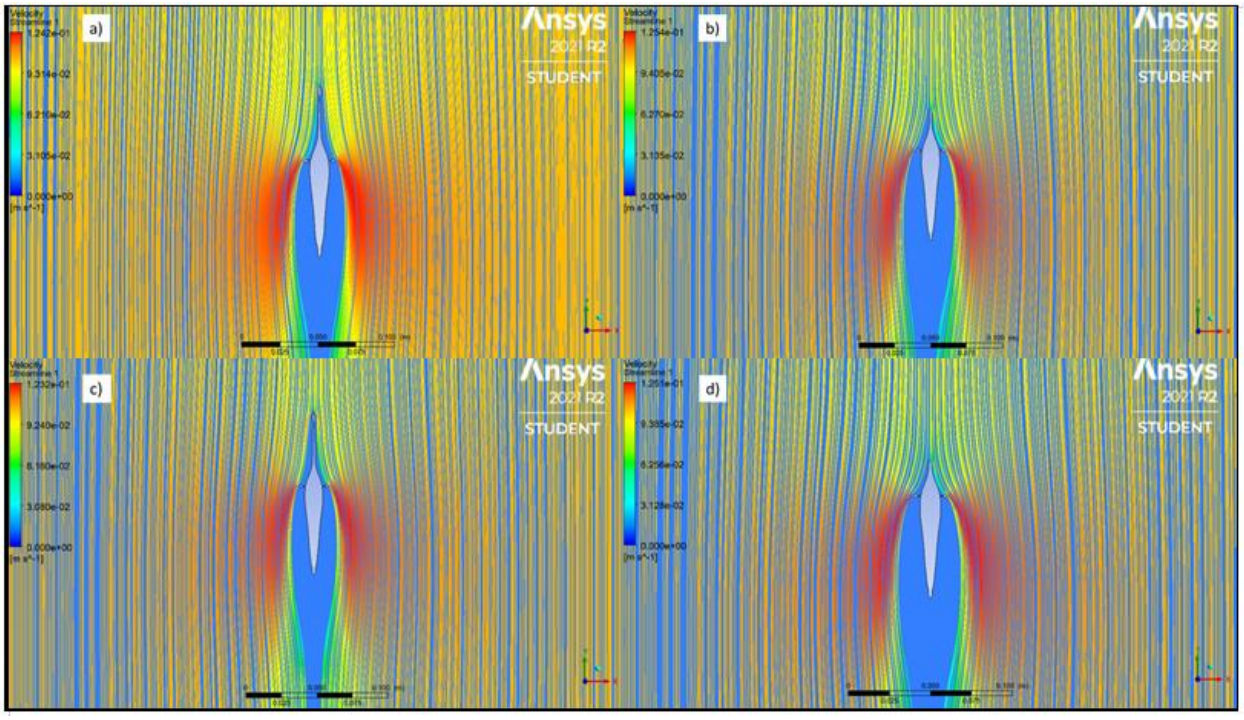

Figure 5.3: The 2D top-down profile results for each model, compiled for comparison. a) The typical reconstruction model b) The fully folded model c) The extended model d) The folded and lowered model.

Proboscis Position During Swimming

The typical reconstruction model, the fully folded model, and the extended model were all designed to test various biologically feasible proboscis positions that we hypothesized could maximize hydrodynamic efficiency. Of these models, the fully folded model appears to offer the most efficient swimming position. While all of the models produced low pressure zone below the body and high-pressure zones above the body, the fully folded model produced these regions with less disruption to the flow compared to the other models. For example, the streamline in the extended model and the typical reconstruction models' 2D side profile simulations suggest that

these models were disrupting more flow by generating larger, red-colored areas indicative of higher velocity below the proboscis (Fig. 5.4). Both of these models also generated more no-velocity wake around the proboscis, suggesting that these proboscis positions physically blocked more water. The extended model specifically blocked a significant amount of water, generating very large pressure differentials around the proboscis and generating a large wake with no velocity (Fig. 5.4).

It is likely more beneficial for the Tully Monster to generate smaller pressure differentials towards the anterior of the body while swimming, given that the Tully Monster is likely a carrangiform or sub-carrangiform swimmer based on its anatomy (McCoy et al., 2016). The anterior of the body is therefore likely not used for propulsion in any way, and any pressure differentials in this region would likely destabilize the anterior of the body in a flow. Therefore, the extended model likely does not offer a feasible swimming position. The extended model generated large pressure differentials along the entire length of the proboscis, which contributed to a downstream low-pressure region that impacted the flow around the dorsal and ventral tail fins (Fig. 5.4). Comparatively, the typical reconstruction model and the fully folded model lacked this low-pressure bubble that extended from the proboscis to the tail fins, suggesting the proboscis did not significantly interact with the tail fins hydrodynamically. This large pressure differential observed around the proboscis in the extended model would also likely overly destabilize the anterior of the Tully Monster and induces stress along the entire proboscis.

While the typical reconstruction model and the fully folded model both generated pressure differentials around the proboscis that likely destabilize the anterior of the body in a flow, other characteristics of the fully folded model's results suggest that it is the most efficient swimming position in this study. Specifically, the fully folded model produced less no-velocity

wake than the typical reconstruction model, which suggests that the fully folded model produces less drag (Fig. 5.4). Furthermore, the fully folded model's 3D results produced vectors around the connection of the dorsal tail fin to the body that pointed in the positive y direction (Fig. 5.4). This suggests that this region provides some amount of lift when the proboscis is fully folded, and therefore likely provides pitch stability by offsetting the destabilizing effects of the pressure differentials around the proboscis.

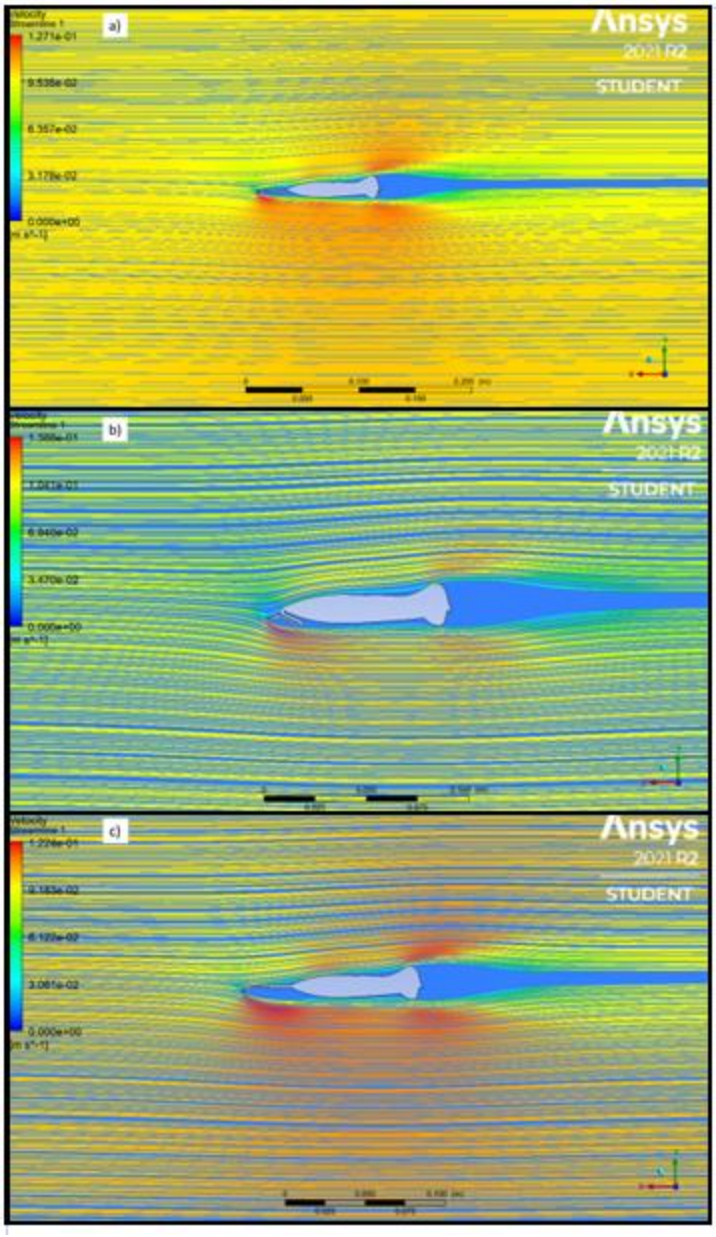

Figure 5.4: The 2D side profile results for three of the models, displayed as velocity streamlines and compiled for comparison. a) The typical reconstruction model b) The fully folded model c) The extended model.

Unlike the other three models, the folded and lowered model was included to assess an ecological hypothesis. Specifically, the Tully Monster could have used its elongated eyebar to see below the body while it picks around the mud with its buccal apparatus for food items,

holding its proboscis in a position like the folded and lowered model. Therefore, this model was simulated to assess whether this configuration would have been hydrodynamically feasible in a flow. As expected, the lowered proboscis significantly disrupts the flow, generating a large wake with no velocity downstream from the proboscis. This disruption generates a large pressure differential across the proboscis, with a high-pressure region on the anterior side of the proboscis and a low-pressure region to the posterior of the proboscis. While this would likely destabilize the anterior of the Tully Monster and induce pitch instability, the folded and lowered model's 3D results showed the similar positive y-axis vectors seen in the fully folded model's results. These vectors clustered near the dorsal tail fin's attachment to the body could offset the pitch instability induced by the lowered proboscis, keeping the body stable as the Tully Monster searches for food around the delta floor. However, this is far from definitive without more robust 3D data to assess how various structures interact with a 3D flow. Regardless, this feeding position may be possible.

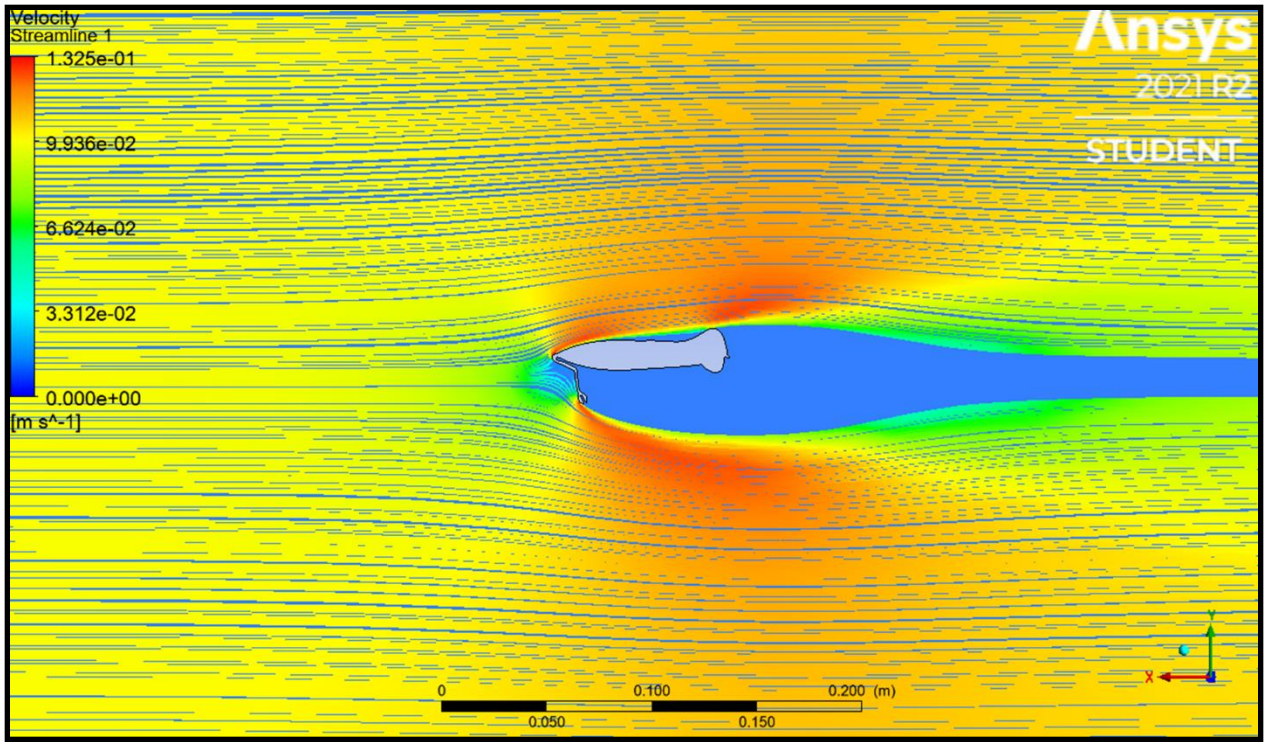

Figure 5.5: The 2D side profile results of the folded and lowered model, displayed as velocity streamlines.

Implications for Swimming and Ecology

Swimming

Ultimately, this study aimed to investigate the Tully Monster's swimming abilities and mechanics by analyzing the general hydrodynamics of the Tully Monster, since these remain unclear due to the Tully Monster's strange body plan and its apparent lack of control features commonly seen in other fish. The Tully Monster only has a dorsal and ventral tail fin, which are placed on the posterior of the body, while it also lacks any paired fins or median fins typically used as to stabilize or turn the body (Webb, 1977; Webb, 1984). There are other fish, like eels and lamprey, that lack paired fins (Webb, 1984; Kern and Koumoutsakos, 2006). However, these fish had tail fins that blend into a longer dorsal and/or ventral fin that extends farther along the body, and these fish have musculature to undulate their entire body for anguilliform swimming

(Kern & Koumoutsakos, 2006). This specialized swimming motion gives these fish stability and directional control across their entire body, even with a lack of paired fins (Kern & Koumoutsakos, 2006). Comparatively, the Tully Monster's broad, oval shaped tail and posteriorly concentrated musculature suggests it would not have been an anguilliform swimmer (McCoy et al., 2016), leaving open several questions about its swimming ability. Primarily, how was the Tully Monster stable in a flow without paired or accessory fins placed anteriorly on the body and how would the Tully Monster change direction or its pitch?

The results of this study suggest that the eyebar served a similar purpose to paired fins and provide some amount of roll and pitch stability. The eyebar accomplishes this by either providing hydrodynamic lift or generating flow disruptions that interact with the tail fins to provide roll control. There is precedent for rigid horizontal structures providing lift and stability in fish. Specifically, the cephalofoils of various hammerhead shark species has been interpreted to provide lift during swimming (Kajiura et al., 2003). Recent studies have challenged this interpretation (Gaylord et al., 2020), but it is generally accepted that the cephalofoil serves a stability function (Kajiura et al., 2003, Gaylord et al., 2003). The bony head shields of armored agnathans also likely provided lift and stability while swimming (Ferrón et al., 2021).

While the eyebar could have provided lift and stability, the eyebar is a rigid structure, and likely could not have been used by the Tully Monster to change direction. Therefore, it is likely that the proboscis was used to change the Tully Monster's swimming direction and control pitch. As seen in the 2D side profiles, the proboscis is capable of significantly disrupting flow around the body by being moved into different positions. Changing the position of the proboscis while swimming or while in a flow could likely turn the body through inertial forces by disrupting the flow. Holding the proboscis slightly to one side of the body's centerline, for example, would

likely create a pivot point for the body to rotate around as the hydrodynamic forces acting on the body become unbalanced. This effect of the proboscis, however, requires further 3D modeling before this hypothesis can be accepted or rejected.

Ecology

Based on the depositional environment of the Mazon Creek sites where Tully Monster specimens have been found and the fauna found in association with Tully Monster specimens, it is likely that the Tully Monster lived in a brackish water, muddy deltaic environment associated with a more marine environment (Baird et al., 1985; Baird et al., 1986; Foster, 1998; Kuecher et al., 1999; Cotroneo et al., 2016; Clements et al., 2019). The Tully Monster has traditionally been considered a predator in this environment, eating small worms, fish, or other prey **(**Mikulic and Kluessendorf, 1991). However, the Tully Monster's body plan would probably restrict its swimming speed, indicating that it likely did not chase prey. Instead, the Tully Monster could have rapidly extended its proboscis to catch unsuspecting prey, bury itself in soft sediments to ambush prey, or browse the seafloor for prey with its proboscis held below the body.

Several modern fish extend their jaws beyond their bodies rapidly to catch unsuspecting prey **(**Westneat and Wainwright, 1989; Burgess et al., 2011), so it is possible that the Tully Monster would have been able to do this with its proboscis. The slingjaw wrasse (*Epibulus insidiator*), for example rapidly extends its jaw to catch prey (Westneat and Wainwright, 1989; Burgess et al., 2011), and the Tully Monster could have rapidly extended its proboscis from a folded position in a similar way to catch unaware prey. This would, however, require some amount of musculature along the proboscis, which is already quite narrow and contains the esophagus (McCoy et al., 2016), but this feeding strategy cannot be ruled-out.

Alternatively, the Tully Monster could have burrowed in the muds and soft sediments along the seafloor or hidden among debris to use its elongated proboscis and extended eyebar to ambush prey. The pressure differentials observed in the 2D side profiles for each model suggest that the pressure gradients generated by the body plan itself would likely pull the Tully Monster downwards in the water column, which could help the Tully Monster remain near or on the seafloor while buried or hiding from prey. However, other body features, like the large, oval-shaped tail region, would not be very beneficial for burial or ambush predation. Furthermore, this study used a laminar flow in each simulation, and the flow near the seafloor of the deltaic environment would be turbulent (Ferrón et al., 2020). These pressure effects may not be present in the complicated turbulent flow, and complicated features like the proboscis and the eyebars may produce different, more destabilizing effects under a turbulent flow.

The folded and lowered model suggests that the Tully Monster may have been able to browse the seafloor for prey with its proboscis held underneath the body while the body is stable in the flow. However, as mentioned earlier, this remains unclear without more robust 3D simulations to determine how drastic the destabilizing effects of holding the proboscis under the body in a flow would be. Furthermore, the Tully Monster would likely be exposed to turbulent flow if it browsed the seafloor, which could affect the body's stability as it fed. Regardless, all of these possibilities require further research with more robust simulations and turbulent models similar to the conditions used by Ferrón et al. in their 2020 paper.

Potential Environmental and Biological Analogues

The Tully Monster remains enigmatic because it lacks a clear modern analogue to serve as a comparison, and the Mazon Creek deltaic environment was likely fairly unique, given the exceptional preservation seen at the site (Baird et al., 1985; Baird et al., 1986; Foster, 1998;

Kuecher et al., 1999; Cotroneo et al., 2016; Clements et al., 2019). The mouth of the Congo River, however, may serve as a compelling analogue for the Mazon Creek environment, and several species of elephantnose fish endemic to the mouth of the Congo River could be used as partial analogues or ecomorphs of the Tully Monster. The Mazon Creek was unquestionably muddy in the Carboniferous, and it likely had a high deposition rate (Baird et al., 1985; Baird et al., 1986; Kuecher et al., 1999; Clements et al., 2019), which is usually indicative of a higher flow regime in the river system feeding the delta. However, the Lagerstätte is dominated by thick shale deposits indicative of low or no flow deposition (Baird et al., 1985; Baird et al., 1986; Foster, 1998; Kuecher et al., 1999; Cotroneo et al., 2016; Clements et al., 2019), even though the fossil bearing sites are relatively close to the reconstructed paleo-coast (Baird et al., 1985; baird et al., 1986; Clements et al., 2019). Similarly, the Congo transports significant amounts of mud, and the mouth of the Congo is notably murky (Bailey and Banister, 1986; Savoye et al., 2000; Savoye et al., 2009; Dennielou et al., 2017). However, the Congo does not form a delta or estuary ((Bailey and Banister, 1986; Savoye et al., 2000; Savoye et al., 2009; Dennielou et al., 2017). Instead, the mouth of the Congo River is deep, and empties into a submarine canyon in the continental shelf (Savoye et al., 2000; Savoye et al., 2009; Dennielou et al., 2017). As a result, the sediments and debris carried by the river cascade almost directly off of the continental shelf once they exit the river system, preventing the formation of a proper delta (Bailey and Banister, 1986; Savoye et al., 2000; Savoye et al., 2009; Dennielou et al., 2017)

It is possible the Mazon Creek represents a similar environment, given that the depositional environment and sedimentology of the Lagerstätte remain mostly unclear. It has been hypothesized that the morphology and flow conditions at the mouth of the Congo River has generated several unique ecosystems separated by flow conditions or sediment type (Feulner et

al., 2007; Lamanna et al., 2016; Amen et al., 2020). These smaller, ecologically distinct ecosystems are relatively isolated from each other, promoting speciation and resulting in cohorts of unique endemic groups of fish (Stewart and Roberts, 1976; Market et al., 2010). One of these groups, the elephant fish of family Mormyridae (Feulner et al, 2008; Decru et al, 2017), may be a useful ecological analogue for the Tully Monster. Some genera within the Mormyridae, such as *Campylomormyrus* have extended rostrums with mouths at the end (Sullivan et al., 2002; Feulner et al, 2007; Feulner et al., 2008), similar to the Tully Monster elongate anterior proboscis (Fig. 5.6), and they typically browse for small bits of food among the sediments in the river bottom using suction feeding (Marrero and Winemiller, 1993, Amen et al., 2020). Most *Campylomormyrus* species do not have a proboscis as drastically long relative to their body length as the Tully Monster (Feulner et al, 2008; Lamanna 2016), but some, such as *C. numenius* have much longer rostrums that are more analogous to the Tully Monster's proportions. Speciation patterns among the genus *Campylomormyrus* suggest that variations in the rostrum length and morphology are adaptations to different ecological niches and specifically different feeding strategies or different food sources (Feulner et al, 2008). A recent experimental study determined that rostrum length in the genus *Campylomormyrus* is linked to substrate preference, and that the longest rostrums, analogous to the Tully proboscis, correlate with a preference for picking food out of stone substrates (Amen et al., 2020). By analogy, the Tully Monster proboscis may also be functionally adapted to picking food out of sediments on the river or estuary bottom, and based on the length of the proboscis, possibly the most likely ecological niche is picking food out of stone substrates bottoms. It has been suggested that the elongated Tully Monster eyebar provides a wide field of vision necessary for the Tully Monster to visualize the full range of motion of the probiscis (McCoy et al., 2016) by comparison to the large field of

view afforded by the wide head of a hammerhead shark (McComb et al., 2009) and the elongate eyestalks in dragonfish larvae (Weihs and Moser, 1981), these long-rostrumed elephantnose fish do not have eyes on stalks. However, fish in the family Mormyridae generate weak electric fields which they use as their primary sense for capturing prey (Feulner et al, 2008; Crampton, 2018), and this genus in particular has a strong electro-sense and weak vision (Stevens et al., 2013) and therefore it may use other senses than vision to 'aim' the rostrum.

However, these elephantnose fish with elongated rostrums are not a perfect analogue for the Tully Monster since they have pectoral fins, a different tail fin shape (Fig. 5.6). However, they are living in an environment that is likely similar to the Carboniferous delta the Tully Monster inhabited. Therefore, new findings on this elephantnose fish's life habits could be used to inform future hypotheses on the Tully Monster's swimming and ecological niche.

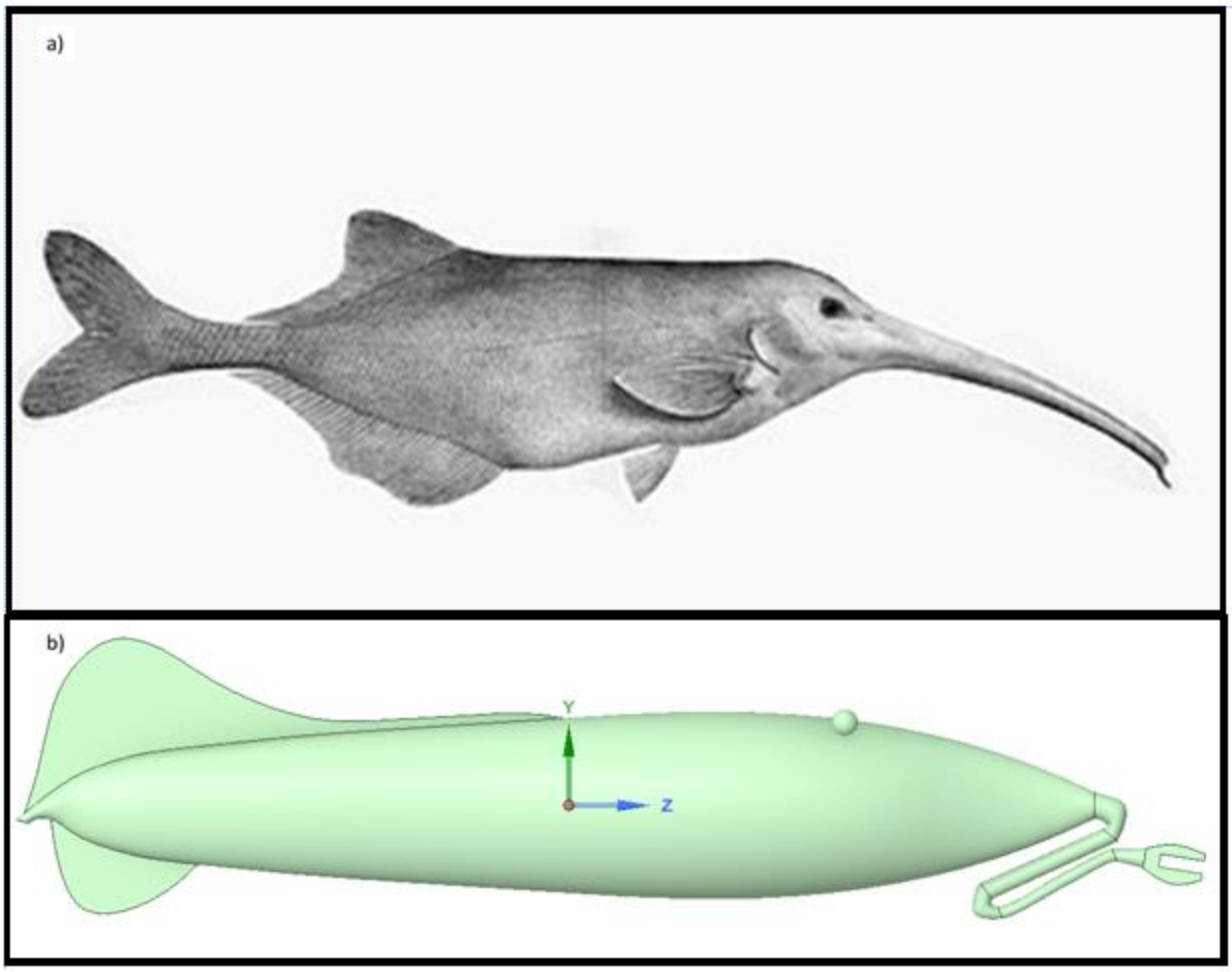

Figure 5.6: A side-by-side comparison of Campylomormyrus numenius and a the fully folded Tully Monster model to highlight similarities and differences between the two fish. a) An image of *Campylomormyrus numenius*. b) An image of the fully folded Tully Monster model. The fully folded model was chosen specifically to demonstrate the potential disparity between the two fish. The rostrum of *Campylomormyrus numenius* is roughly 1/3 of its entire length while the proboscis and buccal apparatus of the Tully Monster is roughly 1/4 of its entire length.

Chapter 6: Conclusion

This study investigated the Tully Monster's swimming abilities by modeling four hypothesized proboscis positions based on the anatomical interpretations made by McCoy et al. (2016). 3D and 2D simulations revealed that the Tully Monster's tail fin likely could have produced the pressure gradients required for sculling. Given that this study did not investigate fin-ray undulations, this method of propulsion cannot be ruled-out, but the Tully Monster would have likely been able to scull even if it relied primarily on fin-ray undulations for propulsion. Furthermore, the Tully Monster body plan generated a pressure differential above and below the body that would favor descending in the water column, regardless of proboscis position. Along with this, this study suggests that the eyebar is a critical hydrodynamic feature that either provides lift, stability, or both lift and stability during swimming. Based on these findings, the Tully Monster was most likely analogous to slow, bottom dwelling fish, and its eyebar was likely a stability structure to stabilize the head region. The eyebar was not, however, likely used to lift the Tully Monster in the water column.

This study also aimed to investigate which proboscis position would have been the most feasible position for the Tully Monster to hold while swimming. While this study cannot entirely discard any of the four hypotheses, the fully folded proboscis position seems to be the most hydrodynamically efficient proboscis position. Specifically, the fully folded model's simulations suggested that this proboscis position generated stabilizing forces at the tail fin while also reducing drag towards the anterior of the body. This proboscis position also produced smaller zones of low and high-pressure around the proboscis compared to the other proboscis positions, suggesting that the anterior of the body is likely more stable when the proboscis is fully folded and tucked underneath the body. It is important to note, however, that the most

hydrodynamically efficient proboscis position may not be the position the proboscis was truly held in while the Tully Monster was alive. Regardless, hydrodynamic efficiency likely remains a good proxy to assess proboscis position and swimming in the absence of other lines of evidence.

It is also possible that the proboscis position during swimming was variable if the proboscis was used as a speedbrake. Moving the proboscis into different positions relative to the body would have disrupted the flow of water around the body and producing drag. This would slow the entire body, stopping forward motion. In the absence of other control features for braking, it is likely the proboscis could have served a braking function.

This study was also unable to narrow-down the ecological niche of the Tully Monster. Various ideas regarding the Tully Monster's feeding strategy, such as slingjaw-wrasse-like ambush predation where the proboscis rapidly extends to capture unsuspecting prey, ambush predation near the ocean bottom where the Tully can remain mostly hidden, and browsing predation where the Tully Monster picks through sediment on the seafloor to find prey, all remain feasible based on this study's results. However, the Tully Monster was likely not a fast swimmer, and was therefore likely incapable of successfully chasing-down prey based on the results of this study. This widely agrees with the Tully Monster's morphology, which is not suited to sustained fast swimming (Webb, 1984; Lauder, 1989; Videler, 1993; Arreola and Westneat, 1996; Drucker and Lauder, 2001; Flammang and Lauder, 2009; Tytell et al., 2010; McCoy et al., 2016; Han et al., 2020).

While this study was not able to definitively answer questions about the Tully Monster's swimming and its ecology, it provides a solid basis for more focused studies that can help answer these questions. A recurring theme throughout this study was that more robust 3D simulations could model the synergistic effects of various hydrodynamic structures like the proboscis, the

eyebar, and the tailfin to produce a clearer picture of the Tully Monster's likely swimming mechanics and, therefore, its ecology. Specifically, 3D modeling focused on vortex generation following the methods of Dec in their 2019 study can provide insight into the eyebar's role as a stabilizing structure and the proboscis's role in swimming (Dec, 2019). 3D models placed in simulated pelagic and benthic environments following the methods of Férron et al. (2020) could provide further insight into whether the Tully Monster hydrodynamics favored a pelagic or benthic environment while also investigating feeding motions related to each environment. Finally, more robust 3D simulations can attempt to re-create and test various Tully Monster swimming motions, following the methods of Li et al.(2021) to gain a clearer picture of the Tully Monster's complex hydrodynamics during actual swimming.

While this study provided more future directions than clear answers, these preliminary hydrodynamic insights are pivotal for future, more targeted studies designed to test specific swimming-based and ecological hypotheses. This study also revealed that the Tully Monster's eyebar is hydrodynamically important, which provides some answers regarding one of the Tully Monster's strange features. Further computational fluid dynamics studies of the Tully Monster will slowly make this bizarre, charismatic monster less enigmatic.

Chapter 7: References

Aleyev, Y.G., 1977. Creation of propulsive force (locomotion). In *Nekton* (pp. 87-183). Springer, Dordrecht. https://doi.org/10.1007/978-94-010-1324-6_5

Amen, R., Nagel, R., Hedt, M., Kirschbaum, F. and Tiedemann, R., 2020. Morphological differentiation in African weakly electric fish (genus Campylomormyrus) relates to substrate preferences. *Evolutionary Ecology*, *34*(3), pp.427-437. https://doi.org/10.1007/s10682-020-10043-3

Ansys® Student R2 2021, Release 18.1, Help System, Coupled Field Analysis Guide, ANSYS, Inc.

Arreola, V.I. and Westneat, M.W., 1996. Mechanics of propulsion by multiple fins: kinematics of aquatic locomotion in the burrfish (Chilomycterus schoepfi). *Proceedings of the Royal Society of London. Series B: Biological Sciences*, *263*(1377), pp.1689-1696. https://doi.org/10.1098/rspb.1996.0247

Bailey, R.G. and Banister, K.E., 1986. The Zaïre River system. In *The ecology of river systems* (pp. 201-224). Springer, Dordrecht. https://doi.org/10.1007/978-94-017-3290-1_6

Baird, G.C., 1979. Lithology and fossil distribution, Francis Creek Shale in northeastern Illinois. In *Mazon Creek Fossils* (pp. 41-67). Academic Press. https://doi.org/10.1016/B978-0-12-519650-5.50010-2

Baird, G.C., Sroka, S.D., Shabica, C.W. and Beard, T.L., 1985. Mazon Creek-type fossil assemblages in the US midcontinent Pennsylvanian: their recurrent character and palaeoenvironmental significance. *Philosophical Transactions of the Royal Society of London. B, Biological Sciences*, *311*(1148), pp.87-99.

https://doi.org/10.1098/rstb.1985.0141

Baird, G.C., Sroka, S.D., Shabica, C.W. and Kuecher, G.J., 1986. Taphonomy of Middle Pennsylvanian Mazon Creek area fossil localities, northeast Illinois: Significance of exceptional fossil preservation in syngenetic concretions. *Palaios*, pp.271-285. https://doi.org/10.2307/3514690

Ballard, S.E. and Rakocinski, C.F., 2012. Flexible feeding strategies of juvenile gray triggerfish (Balistes capriscus) and planehead filefish (Stephanolepis hispidus) within Sargassum habitat. *Gulf and Caribbean Research*, *24*(1), pp.31-40. https://doi.org/10.18785/gcr.2401.05

Bardack, D. and Zangerl, R., 1968. First fossil lamprey: a record from the Pennsylvanian of Illinois. *Science*, *162*(3859), pp.1265-1267. https://doi.org/10.1126/science.162.3859.1265

Botella, H. and Fariña, R.A., 2008. Flow pattern around the rigid cephalic shield of the Devonian agnathan Errivaspis waynensis (Pteraspidiformes: Heterostraci). *Palaeontology*, *51*(5), pp.1141-1150. https://doi.org/10.1111/j.1475-4983.2008.00801.x

Burgess, S.C., Wang, J., Etoundi, A.C., Vaidyanathan, R. and Oliver, J.D., 2011. A functional analysis of the jaw mechanism in the sling-jaw wrasse. *International Journal of Design & Nature and Ecodynamics*, *6*(4), pp.258-271. https://www.witpress.com/elibrary/DNE-volumes/6/4/539

Chenhan, L. and Yongjun, Z., 1988. Notes on the Chinese paddlefish, Psephurus gladius (Martens). *Copeia*, *1988*(2), pp.482-484. https://doi.org/10.2307/1445891

Clements, T., Dolocan, A., Martin, P., Purnell, M.A., Vinther, J. and Gabbott, S.E., 2016. The eyes of Tullimonstrum reveal a vertebrate affinity. *Nature*, *532*(7600), pp.500-503.

https://doi.org/10.1038/nature17647

Clements, T., Purnell, M. and Gabbott, S., 2019. The Mazon Creek Lagerstätte: a diverse late Paleozoic ecosystem entombed within siderite concretions. *Journal of the Geological Society*, *176*(1), pp.1-11. https://doi.org/10.1144/jgs2018-088

Cotroneo, S., Schiffbauer, J.D., McCoy, V.E., Wortmann, U.G., Darroch, S.A.F., Peng, Y. and Laflamme, M., 2016. A new model of the formation of Pennsylvanian iron carbonate concretions hosting exceptional soft-bodied fossils in Mazon Creek, Illinois. *Geobiology*, *14*(6), pp.543-555. https://doi.org/10.1111/gbi.12197

Crampton, W.G., 2019. Electroreception, electrogenesis and electric signal evolution. *Journal of fish biology*, *95*(1), pp.92-134. https://doi.org/10.1111/jfb.13922

Cunningham, J.A., Rahman, I.A., Lautenschlager, S., Rayfield, E.J. and Donoghue, P.C., 2014. A virtual world of paleontology. *Trends in ecology & evolution*, *29*(6), pp.347-357. https://doi.org/10.1016/j.tree.2014.04.004

Dec, M., 2019. Hydrodynamic performance of psammosteids: New insights from computational fluid dynamics simulations. *Acta Palaeontologica Polonica*, *64*(4). https://doi.org/10.4202/app.00623.2019

Decru, E., Vreven, E., Danadu, C., Walanga, A., Mambo, T. and Snoeks, J., 2017. Ichthyofauna of the Itimbiri, Aruwimi, and Lindi/Tshopo rivers (Congo basin): Diversity and distribution patterns. *Acta Ichthyologica et Piscatoria*, *47*(3), pp.225-247. https://doi.org/10.3750/AIEP/02085

Dennielou, B., Droz, L., Babonneau, N., Jacq, C., Bonnel, C., Picot, M., Le Saout, M., Saout, Y., Bez, M., Savoye, B. and Olu, K., 2017. Morphology, structure, composition and build-up processes of the active channel-mouth lobe complex of the Congo deep-sea fan with

inputs from remotely operated underwater vehicle (ROV) multibeam and video surveys. *Deep Sea Research Part II: Topical Studies in Oceanography*, *142*, pp.25-49. https://doi.org/10.1016/j.dsr2.2017.03.010

Drucker, E. and o, G., 2001. Wake dynamics and fluid forces of turning maneuvers in sunfish. *Journal of Experimental Biology*, *204*(3), pp.431-442. https://doi.org/10.1242/jeb.204.3.431

Evans, C.W., Cziko, P., Cheng, C.H.C. and Devries, A.L., 2005. Spawning behaviour and early development in the naked dragonfish Gymnodraco acuticeps. *Antarctic Science*, *17*(3), pp.319-327. https://doi.org/10.1017/S0954102005002749

Feldman, H.R., Archer, A.W., Kvale, E.P., Cunningham, C.R., Maples, C.G. and West, R.R., 1993. A tidal model of Carboniferous Konservat-Lagerstätten formation. *Palaios*, pp.485-498. https://doi.org/10.2307/3515022

Ferrón, H.G., Martínez-Pérez, C., Rahman, I.A., de Lucas, V.S., Botella, H. and Donoghue, P.C., 2020. Computational fluid dynamics suggests ecological diversification among stem-gnathostomes. *Current Biology*, *30*(23), pp.4808-4813. https://doi.org/10.1016/j.cub.2020.09.031

Ferrón, H.G., Martínez-Pérez, C., Rahman, I.A., Selles de Lucas, V., Botella, H. and Donoghue, P.C., 2021. Functional assessment of morphological homoplasy in stem-gnathostomes. *Proceedings of the Royal Society B*, *288*(1943), p.20202719. https://doi.org/10.1098/rspb.2020.2719

Feulner, P.G.D., Kirschbaum, F., Mamonekene, V., Ketmaier, V. and Tiedemann, R., 2007. Adaptive radiation in African weakly electric fish (Teleostei: Mormyridae: Campylomormyrus): a combined molecular and morphological approach. *Journal of*

evolutionary biology, *20*(1), pp.403-414. https://doi.org/10.1111/j.1420-9101.2006.01181.x

Feulner, P.G., Kirschbaum, F. and Tiedemann, R., 2008. Adaptive radiation in the Congo River: an ecological speciation scenario for African weakly electric fish (Teleostei; Mormyridae; Campylomormyrus). *Journal of Physiology-Paris*, *102*(4-6), pp.340-346. https://doi.org/10.1016/j.jphysparis.2008.10.002

Flammang, B.E. and Lauder, G.V., 2009. Caudal fin shape modulation and control during acceleration, braking and backing maneuvers in bluegill sunfish, Lepomis macrochirus. *Journal of Experimental Biology*, *212*(2), pp.277-286. https://doi.org/10.1242/jeb.021360

Foster, M.W., 1998. Richardson's Guide to the Fossil Fauna of Mazon Creek. *Rocks and Minerals*, *73*(5), p.360.

Gaylord, M.K., Blades, E.L. and Parsons, G.R., 2020. A hydrodynamics assessment of the hammerhead shark cephalofoil. *Scientific Reports*, *10*(1), pp.1-12. https://doi.org/10.1038/s41598-020-71472-2

Gemmell, B.J., Sheng, J. and Buskey, E.J., 2013. Morphology of seahorse head hydrodynamically aids in capture of evasive prey. *Nature Communications*, *4*(1), pp.1-8. https://doi.org/10.1038/ncomms3840

George, A.B., 2020. *Functional Morphology and Evolution of the Balistiform Swimming Mode* (Doctoral dissertation, The University of Chicago). https://www.proquest.com/docview/2428392650?pq-origsite=gscholar&fromopenview=true

Gess, R.W., Coates, M.I. and Rubidge, B.S., 2006. A lamprey from the Devonian period of

South Africa. *Nature*, *443*(7114), pp.981-984. https://doi.org/10.1038/nature05150

Han, P., Lauder, G.V. and Dong, H., 2020. Hydrodynamics of median-fin interactions in fish-like locomotion: Effects of fin shape and movement. *Physics of Fluids*, *32*(1), p.011902. https://doi.org/10.1063/1.5129274

Hultmark, M., Leftwich, M. and Smits, A.J., 2007. Flowfield measurements in the wake of a robotic lamprey. *Experiments in fluids*, *43*(5), pp.683-690. https://doi.org/10.1007/s00348-007-0412-1

Janssen, K., Mähler, B., Rust, J., Bierbaum, G. and McCoy, V.E., 2022. The complex role of microbial metabolic activity in fossilization. *Biological Reviews*, *97*(2), pp.449-465. https://doi.org/10.1111/brv.12806

Jiang H., Costello J. H., and Collins S.P., 2021. Fluid dynamics and efficiency of colonial swimming via multijet propulsion at intermediate Reynolds numbers: Physical Review Fluids, v. 6. https://doi.org/10.1103/PhysRevFluids.6.013103

Johnson, R.G. and Richardson Jr, E.S., 1966. A remarkable Pennsylvanian fauna from the Mazon Creek area, Illinois. *The Journal of Geology*, *74*(5, Part 1), pp.626-631. https://www.journals.uchicago.edu/doi/abs/10.1086/627194

Johnson R.G. and Richardson E.S., 1969. Pennsylvanian invertebrates of the Mazon Creek Area; Illinois: the morphology and affinities of Tullimonstrum: Geology, v. 12 (8), p. 119-149. https://archive.org/details/pennsylvanianinv128john/page/148/mode/2up

Kajiura, S.M., Forni, J.B. and Summers, A.P., 2003. Maneuvering in juvenile carcharhinid and sphyrnid sharks: the role of the hammerhead shark cephalofoil. *Zoology*, *106*(1), pp.19-28. https://doi.org/10.1078/0944-2006-00086

Kern, S. and Koumoutsakos, P., 2006. Simulations of optimized anguilliform swimming. *Journal*

of Experimental Biology, *209*(24), pp.4841-4857. https://doi.org/10.1242/jeb.02526

Kotrschal, K., 1989. Trophic ecomorphology in eastern Pacific blennioid fishes: character transformation of oral jaws and associated change of their biological roles. *Environmental Biology of Fishes*, *24*(3), pp.199-218. https://doi.org/10.1007/BF00001224

Kuecher, G.J., Woodland, B.G. and Broadhurst, F.M., 1990. Evidence of deposition from individual tides and of tidal cycles from the Francis Creek Shale (host rock to the Mazon Creek Biota), Westphalian D (Pennsylvanian), northeastern Illinois. *Sedimentary Geology*, *68*(3), pp.211-221. https://doi.org/10.1016/0037-0738(90)90113-8

Kuratani, S. and Hirasawa, T., 2016. Getting the measure of a monster. *Nature*, *532*(7600), pp.447-448. https://doi.org/10.1038/nature17885

Lamanna, F., Kirschbaum, F., Ernst, A.R., Feulner, P.G., Mamonekene, V., Paul, C. and Tiedemann, R., 2016. Species delimitation and phylogenetic relationships in a genus of African weakly-electric fishes (Osteoglossiformes, Mormyridae, Campylomormyrus). *Molecular phylogenetics and evolution*, *101*, pp.8-18. https://doi.org/10.1016/j.ympev.2016.04.035

Lauder, G.V., 1989. Caudal fin locomotion in ray-finned fishes: historical and functional analyses. *American Zoologist*, *29*(1), pp.85-102. https://doi.org/10.1093/icb/29.1.85

Lauder, G.V. and Drucker, E.G., 2004. Morphology and experimental hydrodynamics of fish fin control surfaces. *IEEE journal of oceanic engineering*, *29*(3), pp.556-571. https://doi.org/10.1109/JOE.2004.833219

Lauder, G.V., Anderson, E.J., Tangorra, J. and Madden, P.G., 2007. Fish biorobotics: kinematics and hydrodynamics of self-propulsion. *Journal of experimental biology*, *210*(16),

pp.2767-2780. https://doi.org/10.1242/jeb.000265

Lee, H.J., Wang, S.W., Lu, M.F. and Chiang, J.S., 2011. The Life and Death of Euler, Bernoulli, and Navier—Stokes Equations and Associated CFD for So-Called Incompressible Fluid Flow. *International Journal of Mechanical Engineering Education*, *39*(2), pp.171-183. https://doi.org/10.7227%2FIJMEE.39.2.7

Li, G., Liu, H., Müller, U.K., Voesenek, C.J. and Van Leeuwen, J.L., 2021. Fishes regulate tail-beat kinematics to minimize speed-specific cost of transport. *Proceedings of the Royal Society B*, *288*(1964), p.20211601. https://doi.org/10.1098/rspb.2021.1601

Maicu, F., De Pascalis, F., Ferrarin, C. and Umgiesser, G., 2018. Hydrodynamics of the Po River-Delta-Sea System. *Journal of Geophysical Research: Oceans*, *123*(9), pp.6349-6372. https://doi.org/10.1029/2017JC013601

Markert, J.A., Schelly, R.C. and Stiassny, M.L., 2010. Genetic isolation and morphological divergence mediated by high-energy rapids in two cichlid genera from the lower Congo rapids. *BMC Evolutionary Biology*, *10*(1), pp.1-9. https://doi.org/10.1186/1471-2148-10-149

Marrero, C. and Winemiller, K.O., 1993. Tube-snouted gymnotiform and mormyriform fishes: convergence of a specialized foraging mode in teleosts. *Environmental Biology of Fishes*, *38*(4), pp.299-309. https://doi.org/10.1007/BF00007523

McComb, D.M., Tricas, T.C. and Kajiura, S.M., 2009. Enhanced visual fields in hammerhead sharks. *Journal of Experimental Biology*, *212*(24), pp.4010-4018. https://doi.org/10.1242/jeb.032615

McCoy, V.E., Saupe, E.E., Lamsdell, J.C., Tarhan, L.G., McMahon, S., Lidgard, S., Mayer, P., Whalen, C.D., Soriano, C., Finney, L., Vogt, S., Clark, E. G., Anderson, R. P.,

Petermann, H., Locatelli, E. R., and Briggs, D. E. G., 2016. The 'Tully monster' is a Vertebrate: Nature, v. 532 (7600), pp.496-499. https://doi.org/10.1038/nature16992

McCoy, V.E., Wiemann, J., Lamsdell, J.C., Whalen, C.D., Lidgard, S., Mayer, P., Petermann, H. and Briggs, D.E., 2020. Chemical signatures of soft tissues distinguish between vertebrates and invertebrates from the Carboniferous Mazon Creek Lagerstätte of Illinois. *Geobiology*, *18*(5), pp.560-565. https://doi.org/10.1111/gbi.12397

McDowall, R.M., 2003. Variation in vertebral number in galaxiid fishes, how fishes swim and a possible reason for pleomerism. *Reviews in Fish Biology and Fisheries, 13*(3), pp.247-263. https://doi.org/10.1023/B:RFBF.0000033121.97066.c1

McDowall, R.M., 2008. Jordan's and other ecogeographical rules, and the vertebral number in fishes. *Journal of Biogeography*, *35*(3), pp.501-508. https://doi.org/10.1111/j.1365-2699.2007.01823.x

Mikulic, D.G. and Kluessendorf, J., 1991. Illinois' state fossil: Tullimonstrum gregarium. *Geogram no. 10.* https://www.ideals.illinois.edu/bitstream/handle/2142/100302/geogram_10.pdf?sequence=2

Nursall, J.R., 1958. The caudal fin as a hydrofoil. *Evolution*, *12*(1), pp.116-120. https://doi.org/10.2307/2405913

Olla, B. L., Samet, C. E., and Studholme, A. L., 1972. Activity and feeding behavior of the summer flounder (Paralichthys dentatus) under controlled laboratory conditions. *Fishery Bulletin*, *70*(4). https://spo.nmfs.noaa.gov/sites/default/files/pdf-content/1972/704/olla.pdf

Patil, H. and Jeyakarthikeyan, P.V., 2018, August. Mesh convergence study and estimation of

discretization error of hub in clutch disc with integration of ANSYS. In *IOP Conference Series: Materials Science and Engineering* (Vol. 402, No. 1, p. 012065). IOP Publishing. https://iopscience.iop.org/article/10.1088/1757-899X/402/1/012065/meta

Peppers, R.A., 1996. *Palynological correlation of major Pennsylvanian (Middle and Upper Carboniferous) chronostratigraphic boundaries in the Illinois and other coal basins* (Vol. 188). Geological Society of America.

Phillips, T.L., Peppers, R.A. and Dimichele, W.A., 1985. Stratigraphic and interregional changes in Pennsylvanian coal-swamp vegetation: environmental inferences. *International Journal of Coal Geology*, *5*(1-2), pp.43-109. https://doi.org/10.1016/0166-5162(85)90010-2

Racicot, R., 2016. Fossil secrets revealed: X-ray CT scanning and applications in paleontology. *The Paleontological Society Papers*, *22*, pp.21-38. https://doi.org/10.1017/scs.2017.6

Richardson Jr, E.S., 1966. Wormlike fossil from the Pennsylvanian of Illinois. *Science*, *151*(3706), pp.75-76. https://doi.org/10.1126/science.151.3706.75.b

Roberts, T.R. and Stewart, D.J., 1976. An ecological and systematic survey of fishes in the rapids of the lower Zaire or Congo River. *Bulletin of the Museum of comparative Zoology*, *147*(6), pp.239-317. https://mormyrids.myspecies.info/sites/mormyrids.myspecies.info/files/roberts__stewart_1976.pdf

Sallan, L., Giles, S., Sansom, R.S., Clarke, J.T., Johanson, Z., Sansom, I.J. and Janvier, P., 2017. The 'Tully Monster'is not a vertebrate: characters, convergence and taphonomy in Palaeozoic problematic animals. *Palaeontology*, *60*(2), pp.149-157.

https://doi.org/10.1111/pala.12282

Savoye, B., Cochonat, P., Apprioual, R., Bain, O., Baltzer, A., Bellec, V., Beuzart, P., Bourillet, J.F., Cagna, R., Cremer, M. and Crusson, A., 2000. Structure and recent evolution of the Zaire deep-sea fan: preliminary results of the ZaiAngo 1 & 2 cruises (Angola-Congo margin). *Comptes Rendus de l'Academie des Sciences Series IIA Earth and Planetary Science*, *3*(331), pp.211-220. https://doi.org/10.1016/S1251-8050(00)01385-9

Savoye, B., Babonneau, N., Dennielou, B. and Bez, M., 2009. Geological overview of the Angola–Congo margin, the Congo deep-sea fan and its submarine valleys. *Deep Sea Research Part II: Topical Studies in Oceanography*, *56*(23), pp.2169-2182. https://doi.org/10.1016/j.dsr2.2009.04.001

Scott, W.B. and Tibbo, S.N., 1968. Food and feeding habits of swordfish, Xiphias gladius, in the western North Atlantic. *Journal of the Fisheries Board of Canada*, *25*(5), pp.903-919. https://doi.org/10.1139/f68-084

Shabica, C.W., 1979. Pennsylvanian sedimentation in Northern Illinois: examination of delta models. In *Mazon creek fossils* (pp. 13-40). Academic Press. https://doi.org/10.1016/B978-0-12-519650-5.50009-6

Shimeld, S.M. and Donoghue, P.C., 2012. Evolutionary crossroads in developmental biology: cyclostomes (lamprey and hagfish). *Development*, *139*(12), pp.2091-2099. https://doi.org/10.1242/dev.074716

Shimose, T., Shono, H., Yokawa, K., Saito, H. and Tachihara, K., 2006. Food and feeding habits of blue marlin, Makaira nigricans, around Yonaguni Island, southwestern Japan. *Bulletin*

of Marine Science, *79*(3), pp.761-775. https://www.ingentaconnect.com/content/umrsmas/bullmar/2006/00000079/00000003/art00027

Stevens, J.A., Sukhum, K.V. and Carlson, B.A., 2013. Independent evolution of visual and electrosensory specializations in different lineages of mormyrid electric fishes. *Brain, Behavior and Evolution*, *82*(3), pp.185-198. https://doi.org/10.1159/000355369

Sullivan, J.P., Lavoué, S. and Hopkins, C.D., 2002. Discovery and phylogenetic analysis of a riverine species flock of African electric fishes (Mormyridae: Teleostei). *Evolution*, *56*(3), pp.597-616. https://doi.org/10.1111/j.0014-3820.2002.tb01370.x

Summers, R.W., 1980. The diet and feeding behaviour of the flounder Platichthys flesus (L.) in the Ythan estuary, Aberdeenshire, Scotland. *Estuarine and Coastal Marine Science*, *11*(2), pp.217-232. https://doi.org/10.1016/S0302-3524(80)80042-9

Thomason, J. ed., 1997. *Functional morphology in vertebrate paleontology*. Cambridge University Press.

Troelsen, P.V., Wilkinson, D.M., Seddighi, M., Allanson, D.R. and Falkingham, P.L., 2019. Functional morphology and hydrodynamics of plesiosaur necks: does size matter?. *Journal of Vertebrate Paleontology*, *39*(2), p.e1594850. https://doi.org/10.1080/02724634.2019.1594850

Turingan, R.G., 1994. Ecomorphological relationships among Caribbean tetraodontiform fishes. *Journal of Zoology*, *233*(3), pp.493-521. https://doi.org/10.1111/j.1469-7998.1994.tb05279.x

Tytell, E.D., Borazjani, I., Sotiropoulos, F., Baker, T.V., Anderson, E.J. and Lauder, G.V., 2010.

Disentangling the functional roles of morphology and motion in the swimming of fish. *Integrative and comparative biology*, *50*(6), pp.1140-1154. https://doi.org/10.1093/icb/icq057

Videler, J.J., 1993. *Fish swimming* (Vol. 10). Springer Science & Business Media.

Vose, F.E. and Nelson, W.G., 1994. Gray triggerfish (Balistes capriscus Gmelin) feeding from artificial and natural substrate in shallow Atlantic waters of Florida. *Bulletin of Marine Science*, *55*(2-3), pp.1316-1323. https://www.ingentaconnect.com/content/umrsmas/bullmar/1994/00000055/F0020002/art00084#expand/collapse

Wainwright, P.C., 1994. Functional morphology as a tool in ecological research. *Ecological morphology:integrative organismal biology*, pp.42-59.

Webb, P.W., 1977. Effects of median-fin amputation on fast-start performance of rainbow trout (Salmo gairdneri). *Journal of Experimental Biology*, *68*(1), pp.123-135. https://doi.org/10.1242/jeb.68.1.123

Webb, P.W., 1984. Form and function in fish swimming. *Scientific American*, *251*(1), pp.72-83. https://www.jstor.org/stable/24969414

Weihs, D. and Moser, H.G., 1981. Stalked eyes as an adaptation towards more efficient foraging in marine fish larvae. *Bulletin of Marine Science*, *31*(1), pp.31-36. https://swfsc-publications.fisheries.noaa.gov/publications/CR/1981/8170.PDF

Westneat, M.W. and Wainwright, P.C., 1989. Feeding mechanism of Epibulus insidiator (Labridae; Teleostei): evolution of a novel functional system. *Journal of Morphology*, *202*(2), pp.129-150. https://doi.org/10.1002/jmor.1052020202

Wueringer, B.E., Squire, L. and Collin, S.P., 2009. The biology of extinct and extant sawfish

(Batoidea: Sclerorhynchidae and Pristidae). *Reviews in Fish Biology and Fisheries, 19*(4), pp.445-464. https://doi.org/10.1007/s11160-009-9112-7